Interplay of π–π Stacking and Hydrogen Bonding in Conjugated Supramolecular Systems studied by Solid-State NMR

Dissertation zur Erlangung des Grades
„Doktor der Naturwissenschaften"
im Promotionsfach Chemie

am Fachbereich Chemie, Pharmazie und Geowissenschaften
der Johannes Gutenberg-Universität in Mainz

von

Anne Bohle
geboren in Berlin

Mainz 2010

Die vorliegende Arbeit wurde in der Zeit von August 2007 bis Juli 2010 am Max-Planck-Institut für Polymerforschung in Mainz angefertigt. Die Dissertation erfolgte an der Johannes Gutenberg-Universität Mainz (D77).

Tag der mündlichen Prüfung: 28.07.2010

Contents

1. Introduction 10

2. Theoretical Background 13
   - 2.1. NMR Interactions . . . 13
     - 2.1.1. Zeeman Interaction . . . 14
     - 2.1.2. Radio Frequency Pulse . . . 16
     - 2.1.3. Chemical Shift . . . 17
     - 2.1.4. Dipole–Dipole Interaction . . . 19
     - 2.1.5. Quadrupolar Coupling . . . 21
     - 2.1.6. *J*-Coupling . . . 22
   - 2.2. Magic Angle Spinning (MAS) . . . 22
   - 2.3. Decoupling Methods . . . 23
     - 2.3.1. Heteronuclear Decoupling . . . 24
     - 2.3.2. Homonuclear Decoupling . . . 25
   - 2.4. Recoupling Methods . . . 25

3. NMR Methods and Pulse Sequences 28
   - 3.1. Basic NMR Experiments . . . 28
     - 3.1.1. Single Pulse Experiment . . . 28
     - 3.1.2. Cross Polarization (CP) . . . 29
   - 3.2. Advanced 2D NMR Methods . . . 31
     - 3.2.1. Coherence Order . . . 32
     - 3.2.2. ^{1}H–^{1}H DQ–SQ MAS NMR Using Back-to-Back Recoupling . . . 33
     - 3.2.3. REPT-HSQC . . . 35
     - 3.2.4. FSLG-Decoupled CP HETCOR . . . 37
     - 3.2.5. REPT-HDOR . . . 38

4. Shape-Persistent Macrocycles 41
   - 4.1. Shape-Persistent Macrocycles Based on Phenylene-Ethynylene Units . . . 41
   - 4.2. Aggregation and Phase Behavior of SPM-1 . . . 44

4.3. Aggregation and Phase Behavior of SPM-2 54
4.4. Conclusion 57

5. Conductive Polymers Based on Polythiophenes for Organic Photovoltaics 59
5.1. Basic Principle of a Photovoltaic Cell 60
5.2. Introduction of the Investigated Systems 62
5.2.1. Wide Angle X-ray Scattering (WAXS) Investigations 64
5.2.2. Previous Solid-State NMR Investigations 65
5.3. Aggregation and Packing of P3ATs 66
5.4. Aggregation and Packing of P3OctiT 77
5.5. Aggregation of Bulk-Heterojunctions Based on P3HT and PCBM 80
5.6. Aggregation of PCPDTBT 88
5.7. Aggregation of a Bulk-Heterojunction Based on PCPDTBT and PCBM . . 89
5.8. Conclusions 93

6. Aggregation of Oligo(p-benzamides) - Poly(ethylene glycol) Copolymers 94
6.1. Rod–Coil Copolymers Based on OPBA-PEG 95
6.2. Aggregation of OPBA–PEG Copolymers in Solution 97
6.3. Aggregation of Unsubstituted OPBAs in the Solid State 98
6.3.1. OPBA-2 and OPBA-3 100
6.3.2. OPBAs with (n $\geq$ 2) 104
6.4. Aggregation of OPBA-PEG Copolymers in the Solid State 108
6.5. Phase Behavior of OPBA-PEG Copolymers 112
6.6. Conclusion 115

7. Conclusion 117

Appendix 120

A. Sample Preparation 120
A.1. Macrocycles 120
A.2. Thiophene based polymers 120
A.3. Rod–coil copolymers 120

B. Methods 121
B.1. Solid-State NMR 121
B.2. WAXS 122

B.3. POM 122
B.4. DSC 122
B.5. Theoretical calculations 123

References 124

Danksagung 132

Abbreviations

AFM ..... atomic force microscopy
BaBa ..... back to back
COSY ..... correlation spectroscopy
CP ..... cross polarization
CS ..... chemical shift
CSA ..... chemical shift anisotropy
D ..... dipole–dipole interaction
DMF ..... dimethylformamide
DQ ..... double quantum
DQC ..... double quantum coherence
DQF ..... double quantum filter
DSC ..... differential scanning calorimetry
ex ..... external
FID ..... free induction decay
FSLG ..... frequency-switched Lee-Goldburg
FT ..... Fourier transformation
GPC ..... gel permeation chromatography
HDOR ..... heteronuclear dipolar order recoupling
HETCOR ..... heteronuclear correlation
HETERO ..... heteronuclear
HOMO ..... highest occupied molecular orbital
HOMO ..... homonuclear
HSQC ..... heteronuclear single quantum correlation
ind ..... induced
int ..... internal
ITO ..... indium doped tin oxide
J ..... *J*-coupling
LED ..... light emitting diode
LUMO ..... lowest unoccupied molecular orbital
MA ..... magic angle

MAS ..... magic angle spinning
NICS ..... nuclear independent chemical shift
nuc ..... nucleus
OPBA ..... oligo(p-benzamide)
P3AT ..... poly(3-alkylthiophene)
P3HepT ..... poly(3-heptylthiophene)
P3HT ..... poly(3-hexylthiophene)
P3OT ..... poly(3-octylthiophene)
P3PT ..... poly(3-pentylthiophene)
PCBM ..... [6,6]-phenyl-C_{61}-butyric acid methyl ester
PCPDTBT ..... poly[2,6-(4,4-bis-(2-ethylhexyl)-4H-cyclopenta[2,1-b;3,4-b‘] dithiophene)-alt-4,7(2,1,3-benzothiadiazole)]
PEDOT ..... poly(ethylene-dioxythiophene)
PEG ..... poly(ethylene glycol)
POM ..... polarization optical microscope
PSS ..... polystyrene sulfonic acid
Q ..... quadrupole interaction
REDOR ..... rotational-echo double-resonance
REPT ..... recoupled polarization transfer
RF ..... radio frequency
S ..... spin
SAXS ..... small angle X-ray scattering
SFM ..... scanning force microscopy
SPM ..... shape persistent macrocycle
SQ ..... single quantum
SQC ..... single quantum coherence
TEM ..... transmission electron microscopy
TPPM ..... two pulse phase modulation
VT ..... variable temperature
WAXS ..... wide angle X-ray scattering
XRD ..... X-ray diffraction
Z ..... Zeeman
ZQC ..... zero quantum coherence

1. Introduction

One main focus of research in this decade is the investigation of renewable energy sources like wind, water and sun power. Especially the utilization of sun power is, at the moment, less than 1% despite the high potential, which is connected with this source. Theoretically the sun is able to provide about 10000 times more energy than the world population needs.[1] However, the utilization of the sun is at the moment orders of magnitudes too expensive and hence, the usage is limited and only feasible with subsidies from the government. The hope is that with a new generation of devices, which should be much cheaper compared to the devices available at the moment, the usage of sun energy could be extended. To decrease the device costs, one possible approach could be to replace the silicon based material used at the moment with inexpensive and easily processable organic compounds. Potential materials for this kind of application include highly conjugated π-systems, but demanding requirements have to be met to gain sufficient device efficiencies and life times. Hence, a well-defined and assessable aggregation behavior is essential and not yet fully understood. One focus of this work is therefore to understand the self-assembly and aggregation behavior of suitable materials for organic photovoltaic applications and the corresponding driving forces for aggregation based on non-covalent interactions like π–π-stacking and hydrogen bonding. Suitable organic materials include highly conjugated π-systems, which are responsible for the essential conductivity, for the rigidity and, in most cases, also for the insolubility. In order to improve these properties of the conjugated building blocks, alkyl side chains are often attached. In some cases these are also able to introduce liquid-crystalline phases which are dealt within another topic of the present work.

Advanced solid-state NMR techniques are important for studying the above-mentioned non-covalent interactions and the liquid-crystallinity. An introduction to these methods is given in **Chapter 2** and **Chapter 3**. Specifically, ^{13}C $\{^{1}$H$\}$ cross polarization (CP) magic angle spinning (MAS) NMR and 2D techniques like frequency-switched Lee-Goldburg (FSLG) decoupled CP heteronuclear correlation (HETCOR) and ^{1}H–^{1}H double quantum–single quantum (DQ–SQ) correlations are used to gain insights about the local structure. The local molecular mobility can be assessed via the recoupled po-

larization transfer-heteronuclear dipolar order recoupling (REPT-HDOR) method.
Three supramolecular organic systems are studied in more detail in this work: conjugated macrocycles, polymer systems based on polythiophene and a rod–coil copolymer based on a rigid rod of oligo(p-benzamides) (OPBA) and a flexible poly(ethylene glycol) (PEG) chain. All systems include rigid building blocks with conjugated π-systems and flexible side chains of different length. They differ in the geometric shape of the rigid block and the proportion of this block compared to the flexible side chains. Thus, the structural properties of the corresponding system can be studied with respect to the presence of non-covalent interactions.
In **Chapter 4**, a model system based on a macrocycles of phenylene, ethynylene, and benzodithiophene units attached with alkyl side chains is the main focus. Within this system, the size of the rigid block and the flexible alkyl side chains are of the same order of magnitude. Two macrocycles are studied in more detail. The corresponding structural differences of both macrocycles are investigated via differential scanning calorimetry (DSC), wide angle X-ray scattering (WAXS), and solid-state NMR. It is determined how different types of alkyl side chains influence non-covalent interactions like π–π-stacking and the local order and molecular mobility. Another issue strongly connected to the alkyl side chains, is the liquid-crystallinity of these systems. To study the influence of the alkyl side chains with respect to this property of the macrocycle temperature-depended solid-state NMR measurements are performed.
The systems studied in **Chapter 5** are rather close to industrial applications. Specifically, two polymers with a fully conjugated and hence rigid polymer backbone are in the focus. The properties of such polymers can be influenced via alkyl chains attached to each monomer unit. Compared to the size of the rigid backbone the alkyl side chains are rather short. The ability of the polymer to self-assemble, in the neat state and after addition of a fullerene derivative as an acceptor, with respect to preparation conditions like thermal treatment is studied. Additionally, the influence of the alkyl chain length on the self-assembled structure is studied for a selected polymer system.
In **Chapter 6**, besides π–π-stacking and phase separation of different building blocks, hydrogen bonding as a third type of non-covalent interactions come into play. The studied systems are based on rigid OPBA rods, which are attached to PEG polymer chains. First, it is investigated how the structure and aggregation can be manipulated via suppression of a certain hydrogen bond in neat OPBAs. Afterwards, differences of the structure and aggregation upon polymer attachment are evaluated and discussed, in light of the influence of the resulting liquid-crystalline phase transition.

Finally, all results are summarized and discussed, in the context of future prospects.

2. Theoretical Background

2.1. NMR Interactions

Every NMR experiment is based on the nuclear spin and its interactions with electrical and magnetic fields. These fields may originate from external sources or within the sample itself. If one distinguishes between external and internal spin interactions, the spin Hamiltonian $\hat{H}_S$ is given by

$$\hat{H}_S = \hat{H}_{ex} + \hat{H}_{int} \ . \tag{2.1}$$

There are two main external interactions: the interaction of the sample with the static magnetic field of the spectrometer (B_0), which is also known as the Zeeman interaction, and the interaction with the applied radio-frequency (rf) pulse (B_1). Internal spin interactions are the chemical shift, the dipole–dipole interaction, the J-coupling, and the quadrupolar coupling.[2] All interactions can be written in form of their Hamiltonians and the spin Hamiltonian is then given by the sum of all interactions.

$$\hat{H}_S = \hat{H}_Z + \hat{H}_{RF} + \hat{H}_{CS} + \hat{H}_D + \hat{H}_J + \hat{H}_Q \tag{2.2}$$

The corresponding magnitudes of these interactions are shown in the following table. They are arranged according to their magnitude, starting with the strongest interaction which is in most cases the Zeeman interaction.[3] For nuclei with a low gyromagnetic ratio (γ) like cobalt and manganese the quadrupolar interaction can assume larger values than the Zeeman interaction.[4]

Hamiltonian	Name	Magnitude
$\hat{H}_Z$	Zeeman interaction	100 MHz
$\hat{H}_Q$	Quadrupolar coupling	1-10 MHz
$\hat{H}_D$	Dipolar interaction	50 kHz
$\hat{H}_{CS}$	Chemical shift	20 kHz
$\hat{H}_J$	J-coupling	100 Hz

Table 2.1.: Types of NMR interactions and their magnitudes.

In solids, all interactions have a spatial dependency. Hence, it is convenient to define an axis system, called the laboratory frame. In this frame, the static magnetic field of the spectrometer B_0 is aligned along the *z*-axis and the rf-field B_1 is directed along the *x*-axis (see Figure 2.1).[2] This rf-field is applied via a coil and the corresponding induced current. The same coil can be used to achieve excitation along the *y*-axis, if the phase of the pulse is modified. All spatial information given in the next sections is referred to the laboratory frame unless stated otherwise.

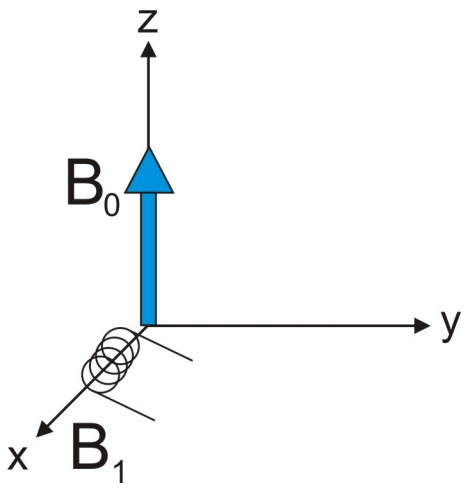

Figure 2.1.: Laboratory frame: the static B_0-field of the spectrometer is aligned along the *z*-axis, the rf-field B_1 is excited along the *x*-axis.

2.1.1. Zeeman Interaction

The Zeeman interaction is the basis for every NMR signal and describes the interaction of the applied magnetic field of the spectrometer (B_0) and the nuclear spin. The

Hamiltonian which represents the energy of this interaction is:

$$\hat{H}_{onespin} = -\gamma B_0 \hat{I}_z \ , \tag{2.3}$$

with the gyromagnetic ratio γ and the operator $\hat{I}_z$ representing the z-component of the nuclear spin angular momentum. As can be inferred from this equation, the Zeeman interaction depends on the magnetic field strength B_0. For a proton, the Zeeman interaction is about 300 MHz in a magnetic field of 7 T and 850 MHz at 20 T. The corresponding energy eigenvalue is given by:

$$E_m = -m\hbar\gamma B_0 \tag{2.4}$$

For a S = 1/2-nucleus, the energy can be written as:

$$E_{\alpha,\beta} = \pm\frac{1}{2}\hbar\gamma B_0 \ . \tag{2.5}$$

Hence in the presence of a static magnetic field there are two distinct non-degenerated energy levels, labeled as E_α and E_β. The energy of the transition between these states can be calculated by subtracting the corresponding energies,

$$\Delta E_{\alpha\to\beta} = E_\beta - E_\alpha = \hbar\gamma B_0 \ , \tag{2.6}$$

where the frequency,

$$\nu_{\alpha\to\beta} = \frac{\gamma B_0}{2\pi} = \nu_0 \ , \tag{2.7}$$

is equal to the Larmor frequency of the nucleus.[5] In a static magnetic field a transition from the α to the β state can be induced by irradiation at the Larmor frequency of the corresponding nucleus (which is in the radio-frequency range, see Table 2.1) and the NMR signal can be recorded (shown in Figure 2.2).

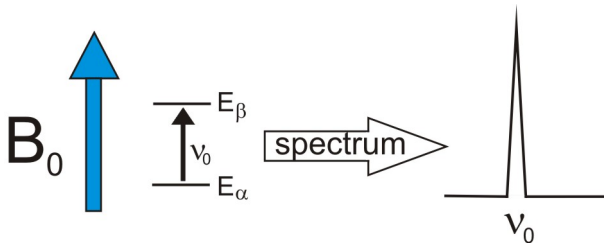

Figure 2.2.: The transition frequency from the α to the β state is equal to the Larmor frequency and the source of the NMR signal.

2.1.2. Radio Frequency Pulse

In a static magnetic field, the spin system interacts with a rf-pulse in a well-defined manner. The Hamiltonian for this interaction is given by the following equation.

$$\hat{H}_{RF} = \omega_1 \hat{I}_x \tag{2.8}$$

$$\omega_1 = -\gamma B_1 \tag{2.9}$$

The B_1 field is the magnetic field, which is associated with the rf-pulse.[6] By means of theoretical approaches based on the density operator formalism the interaction of the rf-pulse with the spin system can be calculated.[5]

$$\hat{\rho}(t_p) = \exp(-i\omega_1 t_p \hat{I}_x)\hat{I}_z \exp(i\omega_1 t_p \hat{I}_x) = \cos(\omega_1 t_p)\hat{I}_z - \sin(\omega_1 t_p)\hat{I}_y \tag{2.10}$$

The effect of a rf-pulse on the equilibrium magnetisation $\hat{I}_z$ can be illustrated by the flip angle $\beta = \omega_1 t_p$. For a 90° *x*-pulse acting on the equilibrium magnetization this is shown in equation (2.11).[7]

$$\hat{I}_z \xrightarrow{90^\circ \hat{I}_x} \cos(90^\circ)\hat{I}_z - \sin(90^\circ)\hat{I}_y = -\hat{I}_y \tag{2.11}$$

Hence the equilibrium magnetization along the *z*-axis is flipped by a 90° x-pulse towards the –*y*-axis, as shown in Figure 2.3.

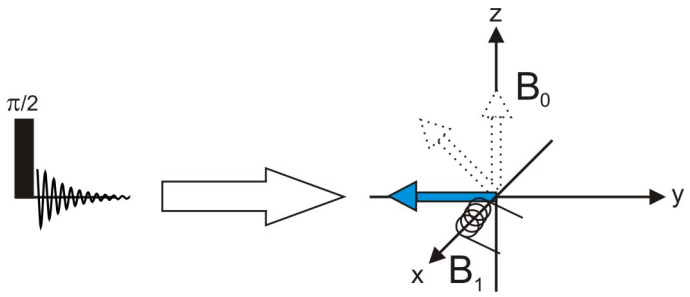

Figure 2.3.: Influence of a $\pi/2$ rf x-pulse on the equilibrium magnetization.

With the product operator approach the effect of any pulse sequence towards the spin system can be worked out. In addition to the effect of pulses, it allows to consider couplings among different spins.

2.1.3. Chemical Shift

Beside the nucleus, electrons interact with the applied magnetic field as well and induce a secondary field. This secondary field contributes to the field, which is present at the site of the nucleus and slightly changes the resonance frequency.[6] This so called chemical shift is very important for a NMR experiment since it enables to distinguish between nuclei with different chemical environments. The effective magnetic field can be expressed by the following equation:

$$B_{nuc} = B_0 + B_{ind} = B_0 + \sigma B_0 = (1 - \sigma)B_0 \tag{2.12}$$

with the shielding tensor σ of a nucleus in a molecule, which can be represented by a (3×3) matrix. This matrix relates the direction and the magnitude of the magnetic field vector at the nucleus (B_{nuc}) to an external magnetic field (B_0). The shielding tensor σ can be decomposed into independent symmetrical and antisymmetrical parts. The σ^{anti} tensor is often neglected since it does not give rise to observable shifts although it affects the relaxation of the spin. The symmetrical tensor can be split into an isotropic tensor σ^{iso} and a traceless symmetric tensor σ^{sym}.[8]

$$\sigma = \sigma^{iso} + \sigma^{sym} + \sigma^{anti} \tag{2.13}$$

If the axis system is chosen such that σ is a diagonal matrix, it is called a principal axis system. In this principle axis system the tensors σ^{iso} and σ^{sym} are defined as:[3]

$$\sigma^{iso} = \sigma_{av} \begin{pmatrix} 1 & 0 & 0 \\ 0 & 1 & 0 \\ 0 & 0 & 1 \end{pmatrix} , \tag{2.14}$$

$$\sigma^{sym} = \delta \begin{pmatrix} -\frac{1}{2}(1+\eta) & 0 & 0 \\ 0 & -\frac{1}{2}(1+\eta) & 0 \\ 0 & 0 & 1 \end{pmatrix} . \tag{2.15}$$

The parameters σ_{av}, δ, η (asymmetry parameter) and $\Delta\sigma$ (anisotropy parameter) are given by

$$\sigma_{av} = (\sigma_{11} + \sigma_{22} + \sigma_{33})/3 , \tag{2.16}$$

$$\delta = \sigma_{33} - \sigma_{av} = \frac{2}{3}\Delta\sigma , \tag{2.17}$$

$$\Delta\sigma = \sigma_{33} - (\sigma_{11} + \sigma_{22})/2 , \tag{2.18}$$

$$\begin{aligned} \eta &= (\sigma_{22} - \sigma_{11})/(\sigma_{33} - \sigma_{av}) = (\sigma_{22} - \sigma_{11})\delta \\ &= (\sigma_{22} - \sigma_{11})/(\frac{2}{3}\Delta\sigma) . \end{aligned} \tag{2.19}$$

An important property of a matrix is the trace, which is the sum of the diagonal elements. As shown in equations (2.14) and (2.15), the trace of σ^{iso} is non-zero in contrast to the trace of σ^{sym}. The trace of a tensor remains unchanged when the tensor is rotated. This is important for an isotropic liquid with fast rotational motion of the molecules. All traceless chemical shift tensors do not give rise to frequency shifts when the system exhibits fast rotation. Thus, in a liquid only the effect of σ^{iso} is observable, which behaves like a scalar and the corresponding spectrum consists of single lines.[8]

In the solid state, the situation is different due to the absence of fast molecular motion. Beside σ^{iso} also the effect of σ^{sym} is observable. σ^{sym} does not behave like a scalar and the chemical shift depends on the orientation of the tensor in the magnetic field. In a powder with many small crystallites, a superposition of many orientations and hence different frequencies occur and a typical powder patter is observed as shown in Figure

2.4.[2] This dependency of the chemical shift on the orientation is called chemical shift anisotropy (CSA).

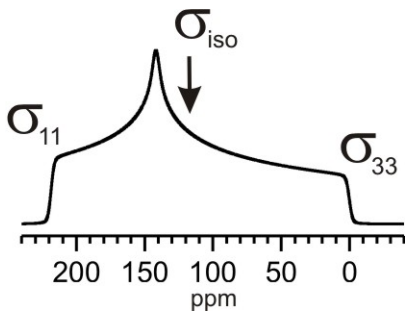

Figure 2.4.: ^{13}C powder pattern for a system with an orthorhombic symmetry.

One can also write the Hamiltonian for the chemical shift interaction in the form shown in equation (2.20). The angles θ and ϕ define the polar coordinates of the vector (cf. Figure 2.5). In analogy to the tensor discussion above equation (2.21) shows that there is no orientation dependency of σ^{iso} in contrast to σ^{sym}.

$$\hat{H}_{CS} = \gamma \hat{I}_z \sigma B_0 \tag{2.20}$$

$$\hat{H}_{CS} = \gamma B_0 [1 - (\sigma^{iso} + \Delta\sigma(3\cos^2\theta - 1 + \eta\sin^2\theta\cos(2\phi)))]\hat{I}_z \tag{2.21}$$

2.1.4. Dipole–Dipole Interaction

Due to their magnetic moment nuclear spins, in close spatial proximity interact with each other. A direct through-space interaction is called dipole–dipole interaction or dipolar coupling. There are two types of coupling: the coupling between equal nuclei is referred to as homonuclear dipolar coupling and the coupling between spins of different nuclei is called heteronuclear dipolar coupling. The Hamiltonian for the dipole–dipole interaction can be written in the Cartesian tensorial form as

$$\hat{H}_D = -2\hat{\mathbf{I}}\mathbf{D}\hat{\mathbf{S}} \, . \tag{2.22}$$

$\hat{I}$ and $\hat{S}$ are spin angular momenta and D is the dipolar coupling tensor. This dipolar

coupling tensor can be written in the principal axis system as[6]

$$D = \begin{pmatrix} -\frac{d}{2} & 0 & 0 \\ 0 & -\frac{d}{2} & 0 \\ 0 & 0 & d \end{pmatrix} , \tag{2.23}$$

$$d = \frac{\mu_0 \hbar}{4\pi r^3} \gamma_I \gamma_S \, . \tag{2.24}$$

Since the trace of the tensor D is zero any dipolar coupling is averaged out in case of fast molecular motion (this effect has already been discussed in section 2.1.3). Therefore, the dipolar coupling can be neglected in liquids, due to the absence of an isotropic component. In contrast the line shape of a solid-state NMR spectrum is strongly influenced by the dipolar coupling. To illustrate this effect equation (2.22) is transformed into the rotating frame. The corresponding result is shown for the homonuclear dipolar coupling in equation (2.25) and for the heteronuclear dipolar coupling in equation (2.26).[6]

$$\hat{H}_{D,homo} = -\frac{\mu_0 \hbar \gamma^2}{4\pi r^3} \cdot \frac{1}{2}(3cos^2\theta - 1)(3\hat{I}_z\hat{S}_z - \hat{\mathbf{I}}\hat{\mathbf{S}}) \tag{2.25}$$

$$\hat{H}_{D,hetero} = -\frac{\mu_0 \hbar \gamma_I \gamma_S}{4\pi r^3} \cdot \frac{1}{2}(3cos^2\theta - 1)2\hat{I}_z\hat{S}_z \tag{2.26}$$

These equations can be separated in a spin part and a space part. The space part shows the orientational dependency of the Hamiltonians. For a dipolar coupled two spin system the corresponding Pake pattern can be derived, which is shown in Figure 2.5.

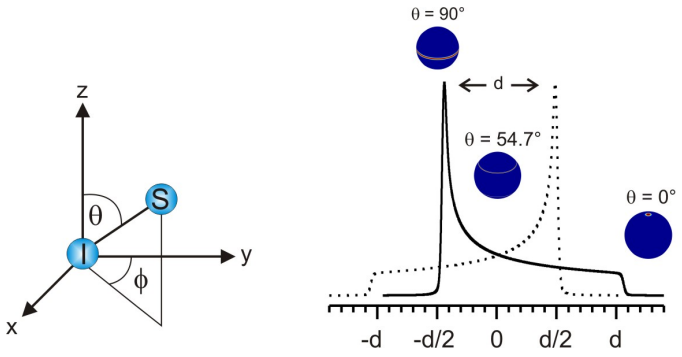

Figure 2.5.: Typical Pake Pattern of two dipolar coupled spins I and S.[9]

The large fraction of spin–spin vectors oriented perpendicular to B_0 induces the highest spectral intensity at $\pm$d/2, while the small fraction of spin–spin vectors parallel to B_0 give rise to spectral minima at $\pm$ d. At an angle of 54.7° towards B_0, the dipolar coupling vanishes. Beside the orientation, the dipolar coupling also depends on the gyromagnetic ratio and the distance between the nuclei. Due to their large gyromagnetic ratio, the homonuclear dipolar coupling between protons is rather strong. As the distance between the nuclei increases, the dipolar coupling decreases dramatically due to the $1/r^3$ dependency. Typical magnitudes of the dipolar coupling constants are given in Table 2.2.

Nuclear Pair	**Internuclear Distance**	**Dipolar Coupling Constant**
^{1}H/^{1}H	2 Å	15 kHz
^{1}H/^{13}C	1 Å	30 kHz
^{1}H/^{13}C	2 Å	3.8 kHz

Table 2.2.: Magnitudes of homo- and heteronuclear dipolar couplings with respect to the internuclear distance.

2.1.5. Quadrupolar Coupling

For nuclei with S $>$ 1/2 the positive electric charges are distributed non-spherically within the nucleus. Hence, they possess a quadrupole moment (Q), which is an intrinsic property of the nucleus like the gyromagnetic ratio. The interaction of the quadrupole moment with the electric field gradient at the nucleus is called quadrupolar coupling and can be rather strong. The corresponding Hamiltonian can be written as

$$\hat{H}_Q = \frac{eQ}{2I(2I-1)\hbar}\hat{\mathbf{I}}\mathbf{V}\hat{\mathbf{I}}\,, \tag{2.27}$$

where **V** is the electric field gradient tensor.[6] Perturbation theory distinguishes between quadrupolar couplings of different order. First-order quadrupolar couplings split spectra of half-integer quadrupolar spin systems in a single crystal into 2*I*–1 satellite lines, with the center line remaining at the Larmor frequency ν_0. Similar to the dipolar coupling it is possible to average out first-order quadrupolar couplings by fast molecular motions.[10] For strong quadrupolar couplings, also second-order terms have to be considered. Both first- and second-order quadrupolar coupling terms broaden

the NMR signals significantly and lead to uninterpretable NMR spectra. The second-order quadrupolar coupling term additionally shifts the center line for half integer nuclei. This coupling cannot be averaged out by molecular motion.[9]

In this work, only the ^{2}H nucleus has been studied as a representative of quadrupolar nuclei. Since it possesses a low quadrupolar moment, only first-order quadrupolar couplings have to be considered.

2.1.6. J-Coupling

The *J*-coupling is an indirect coupling of two nuclei through the electrons of the bond between these nuclei. Hence, nuclei predominantly interact intramolecular via *J*-couplings, though in rare cases also intermolecular *J*-couplings through H-bonds are observed. The Hamiltonian for the *J*-coupling is given by

$$\hat{H}_J = 2\pi \hat{\mathbf{I}}_\mathbf{j} \mathbf{J} \hat{\mathbf{I}}_\mathbf{k} \ . \tag{2.28}$$

Normally, the *J*-coupling is rather weak (cf. Table 2.1) and not observable in solid-state NMR spectra due to broader lines compared to liquid-state NMR spectra.

2.2. Magic Angle Spinning (MAS)

Summarizing the last sections it can be concluded that a S = 1/2 spin system in the liquid state is described by a typical Hamiltonian

$$\hat{H}_S = \hat{H}_Z + \hat{H}_{RF} + \hat{H}_{CS_{iso}} + \hat{H}_J \ . \tag{2.29}$$

Due to the absence of all orientation dependent interactions, the lines in a typical liquid-state NMR spectrum are rather narrow and structural information is accessible from the isotropic chemical shifts and the *J*-coupling. In a solid, due to the absence of fast molecular motions, the spin system is described by the Hamiltonians

$$\hat{H}_S = \hat{H}_Z + \hat{H}_{RF} + \hat{H}_{CS} + \hat{H}_D + (\hat{H}_J) \ . \tag{2.30}$$

In this case, the effect of the CSA and the dipolar coupling broaden the resonances and complicate the extraction of information in the spectrum (Figure 2.6 a).

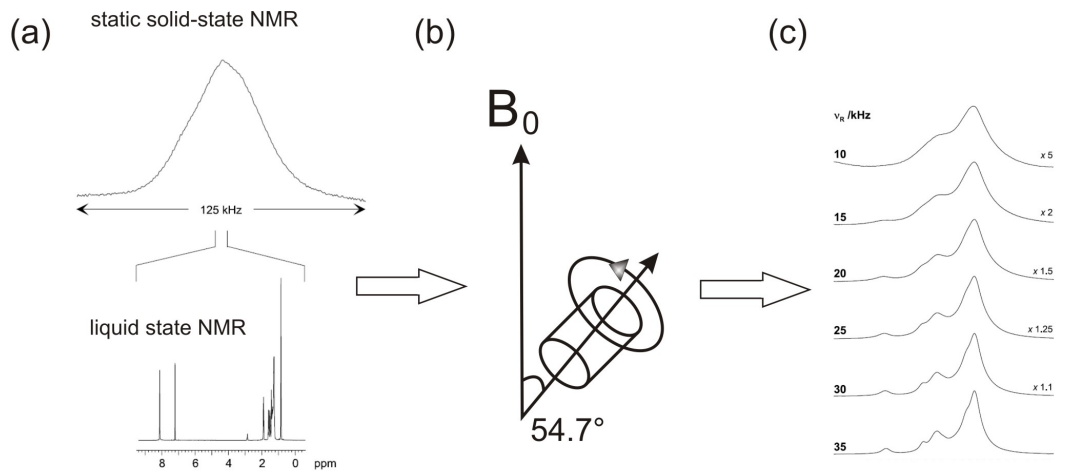

Figure 2.6.: **(a)** Comparison of a ^{1}H static solid-state NMR spectrum and a corresponding liquid-state NMR spectrum. **(b)** illustration of the MAS technique and **(c)** effect of MAS on the ^{1}H solid-state NMR spectrum.[11]

One approach to decrease the line width is to mimic the effect of fast molecular motion like in the liquid state. For this reason, magic angle spinning (MAS) is performed. Under MAS conditions, the sample is rotated at an angle of 54.7° with respect to the external magnetic field (Figure 2.6 b). At this so-called magic angle, the dipolar $3\cos^2\theta$-1 term (see equation (2.25) and (2.26)) and the CSA vanishes, if the sample is rotated sufficiently fast. State-of-the-art devices allow rotational velocities up to 70 kHz. Routinely, the MAS rate is about 30 kHz. Thus, the spatial part of the Hamiltonian, which has an orientational dependency, is averaged by MAS. For an efficient averaging, the spinning rate needs to exceed the largest anisotropic interaction by a factor of three.[6] With a rotation frequency of about 30 kHz, the broadening effect of inhomogenous interactions like CSA and heteronuclear dipolar couplings are significantly reduced. In contrast, homogenous interaction like homonuclear dipolar couplings require higher averaging frequencies.[12]

2.3. Decoupling Methods

Unfortunately MAS alone can not completely average out the interactions which broadens the lines. Therefore additional decoupling methods are necessary.

2.3.1. Heteronuclear Decoupling

Heteronuclear decoupling has to be considered in case of coupling between a hetero nucleus like ^{13}C and protons. Normally, this coupling is an inhomogenous interaction, which is averaged out by MAS rather efficiently. However, in a real sample, homonuclear couplings overlap with heterogeneous interactions, which make MAS alone less sufficient. Therefore, additional decoupling methods need to be used to obtain a high spectral resolution.

Heteronuclear dipolar couplings are most easily decoupled during the recording of the free induction decay (FID). This is performed by continuous rf irradiation on the non-observed channel. This rf irradiation causes the ^{1}H spins to undergo repeated transitions from the α to the β state at a rate determined by the amplitude of the rf irradiation. The disadvantage of that method is, that it causes heating of the sample, especially in the presence of water and it pushes the electronic device of the probehead to their limit.[6] Therefore, alternative decoupling pulse sequences are used to achieve desired resolution within an acceptable rf power range, such as the Two Pulse Phase Modulation (TPPM) method and derivatives thereof.[13] The idea behind TPPM decoupling is to apply rf pulses of τ_p length and alternate them between two phases by an angle of ϕ (Figure 2.7). This decoupling method is even more efficient than the continuous wave decoupling.[14]

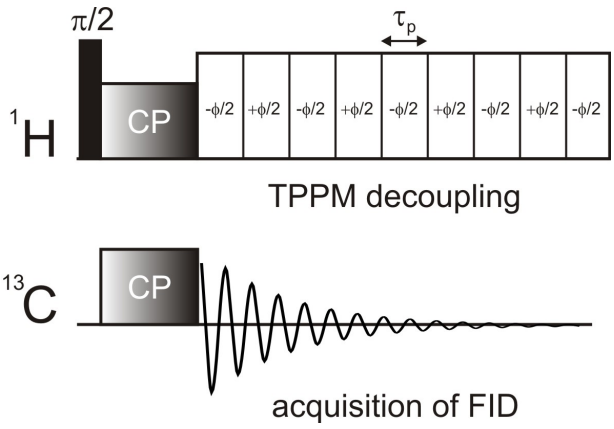

Figure 2.7.: Pulse sequence of a ^{13}C $\{^{1}$H$\}$ CP/MAS experiment with TPPM decoupling on the ^{1}H channel carried out throughout the acquisition of the FID on the ^{13}C channel.[14]

2.3.2. Homonuclear Decoupling

The homonuclear dipole–dipole coupling plays an important role for protons. It can be neglected for carbons due to the low natural abundance of the ^{13}C nucleus. For the protons, a lot of effort has been devoted to invent effective decoupling methods since MAS alone is not sufficient as a result of the large homonuclear coupling between the protons. In this work, especially a method called frequency-switched Lee-Goldburg (FSLG) decoupling has been used to decouple the^{1}H–^{1}H homonuclear couplings in the indirect dimension of a 2D spectrum. This decoupling method is based on a off resonant rf irradiation, which is continuously applied on the proton channel during the t_1-time. The magnitude of this irradiation is adjusted such, that the effective field in the rotating frame is at the magic angle with respect to the static magnetic field. Furthermore, this rf irradiation is switched between the two LG conditions ($\pm\omega_1/\sqrt{2}$) accompanied by a simultaneous π-shift in the phase at the end of each segment. This leads to a rotation of the spin around an effective field, which is tilted away from the static magnetic field by the magic angle. Thus, homonuclear dipolar couplings between the spins are averaged out.[15,16]

2.4. Recoupling Methods

Beside the effect that dipolar couplings broaden the resonances in the corresponding spectrum, these interactions are also a great source of information. Due to the fact that the dipolar coupling interacts through space, useful information about internuclear distances and structural packing can be observed. To access highly resolved spectra, which contain this type of information, methods are needed to selectively recouple this anisotropic interaction under MAS conditions.

The basis of many recoupling methods is the rotational-echo double-resonance (REDOR) technique, which was invented to measure the distance of different hetero nuclei under MAS.[17,18] On the observed nucleus, a normal spin echo experiment with a $\pi/2$-pulse at time zero and a π-pulse after one rotor period is applied. On the non-observed channel, π-pulses are applied after 1/2 and 3/2 rotor periods (Figure 2.8). Due to these π-pulses on the I-spin, the orientation of the local field at the S-spin is changed.[17,18]

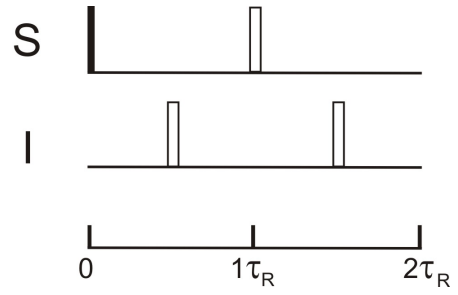

Figure 2.8.: REDOR pulse sequence

The recoupling effect can also be understood by having a closer look at the Hamiltonians. The Hamiltonian of the heteronuclear dipolar coupling can be separated in a spin part and a space part. The space part of the Hamiltonian

$$-\frac{\mu_0 \hbar \gamma^2}{4\pi r^3} \cdot \frac{1}{2}(3cos^2\theta - 1) \tag{2.31}$$

is strongly affected by MAS and partially averaged out. This averaging effect is also observable in the rotor modulation curve shown in Figure 2.9 a.

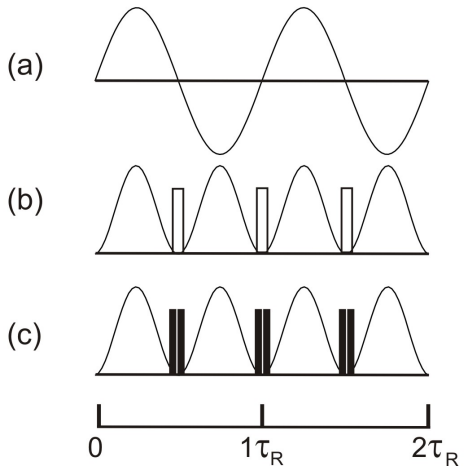

Figure 2.9.: Recoupling schemes under MAS conditions (a) Modulation of an anisotropic interaction, (b) heteronuclear recoupling, and (c) homonuclear recoupling[19]

By integration over a full rotor period, the modulated interaction vanishes as positive and negative parts of the oscillation cancel each other. A way to avoid this cancellation

is to invert the spin part ($2\hat{I}_z\hat{S}_z$) of the Hamiltonian by applying a pulse sequence, which simultaneously alternates the sign of the spin part. For heteronuclear dipolar couplings and CSA, normal π-pulses are sufficient to invert the sign. Figure 2.9 b illustrates how an averaging of the interaction within one rotor period can be avoided by these π pulses.[12] Interactions with a bilinear spin dependence like the homonuclear dipolar coupling can be recoupled in an analogous fashion. However, the π-pulses have to be replaced by a pair of $\pi/2$-pulses with orthogonal phases (Figure 2.9 c).[20] This recoupling scheme is referred to as back-to-back (BaBa) pulse sequence.[12,21]

3. NMR Methods and Pulse Sequences

3.1. Basic NMR Experiments

3.1.1. Single Pulse Experiment

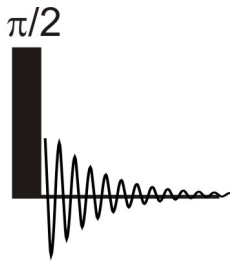

Figure 3.1.: Pulse sequence of a one pulse sequence.

The single pulse experiment is based on a 90° ($\pi/2$) pulse followed by the measurement of the free induction decay (FID, cf. Figure 3.1). The influence of such a $\pi/2$-pulse on the spin system has already been discussed from a theoretical point of view in section 2.1.2. It could be shown that the equilibrium magnetization is flipped via a $\pi/2$ pulse from the z-axis to the transversal plane. The precession of the magnetization within the transverse plane induces a tiny current in the receiver coil which can be measured (the FID). The decay of the FID over time is due to relaxation processes, which make the system return back to its equilibrium state.[5]

The above mentioned pulse sequence is mainly used to measure 1D ^{1}H MAS NMR spectra. Due to the high natural abundance (99.99%) and the large magnitude of the gyromagnetic ratio of protons, no further enhancement strategies are necessary to record a suitable ^{1}H spectrum. In ^{1}H solid-state NMR spectra, non-covalent interactions such as hydrogen bonding and π–π-interactions can be observed. Signals originating from hydrogen-bonded protons are well separated in the spectrum, with typical chemical shifts between 8 and 20 ppm.[22–24] This ^{1}H chemical shift includes semi-quantitative information about the strength of the hydrogen bonds.[22,25–27] In

addition, the ^{1}H chemical shift is a sensitive probe with respect to ring currents associated with aromatic moieties.[11,28] These ring currents are observed as a low-field shift of the chemical shift compared to the corresponding liquid-state signal and constitute a direct hint for π–π-interactions. The line widths of the ^{1}H MAS NMR spectrum give further information about the system. Effects like low molecular mobility and a low degree of local order broaden the lines, while the opposite effect is observable for mobile or highly ordered systems.

3.1.2. Cross Polarization (CP)

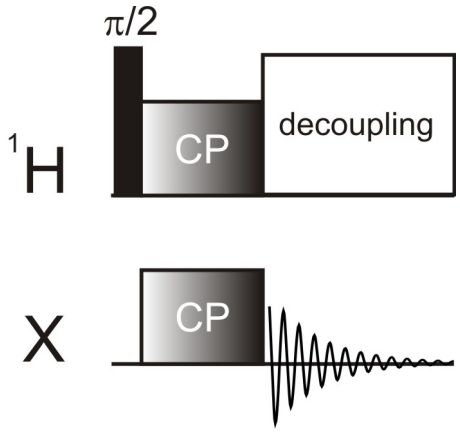

Figure 3.2.: Pulse sequence of a CP-MAS experiment. Heteronuclear spins are denoted X.

Single pulse experiments are only feasible for nuclei with a high natural abundance and a suitable gyromagnetic ratio. However, nuclei like ^{13}C and ^{15}N are of great interest which neither have a high natural abundance (^{13}C 1.1% and ^{15}N 0.4%) nor a proper gyromagnetic ratio. To overcome these problems, Pines et al. invented the concept of cross-polarization (CP) where the magnetization is transferred from abundant spins (normally protons), to the hetero nuclei.[29,30] The first step of the sequence, shown in Figure 3.2, is the rotation of the proton magnetization onto the –*y*-axis by application of a 90° pulse along the *x*-axis. Subsequent spin-locking is achieved by an on-resonant rf-pulse along the –*y*-axis. Thus a high degree of proton polarization is obtained along the spin-lock field, which is labeled B_{1H}. While the ^{1}H spins are locked along the –*y*-axis, an on-resonant pulse B_{1X} is applied on the low abundant X-spins, by which the X-spins are locked along the –*y*-axis as well. By choosing the magnitude of

the spin-locking fields B_{1H} and B_{1X} according to the Hartmann-Hahn condition (shown in equation (3.1)) the magnetization is transferred from the ^{1}H spin reservoir to the X spin reservoir.[31,32]

$$\gamma_{^1H} B_{1H} = \gamma_X B_{1X} \tag{3.1}$$

In the last step, the FID is detected on the X channel while rf pulses are applied on the proton channel for decoupling. Thus the signal intensity of the X-nucleus can be enhanced up to a factor of $\gamma_{^1H}/\gamma_X$, e.g. ^{13}C signals are enhanced up to a factor of four. Additionally the relaxation time determining the measuring time is the proton relaxation, which is typically much shorter than the relaxation of the hetero nucleus, which lack homonuclear couplings.[6] Beside these advantages, the disadvantage is that no quantitative information is available.

In this work, mainly the ^{13}C $\{^1$H$\}$ CP/MAS technique was used. The main advantage ^{13}C spectrum over a ^{1}H spectrum is the increased resolution due to the broader chemical shift range. This is by far more important in solid-state NMR than in solution-state NMR. Typical assignments of carbon atoms in different chemical environments are shown in Figure 3.3.

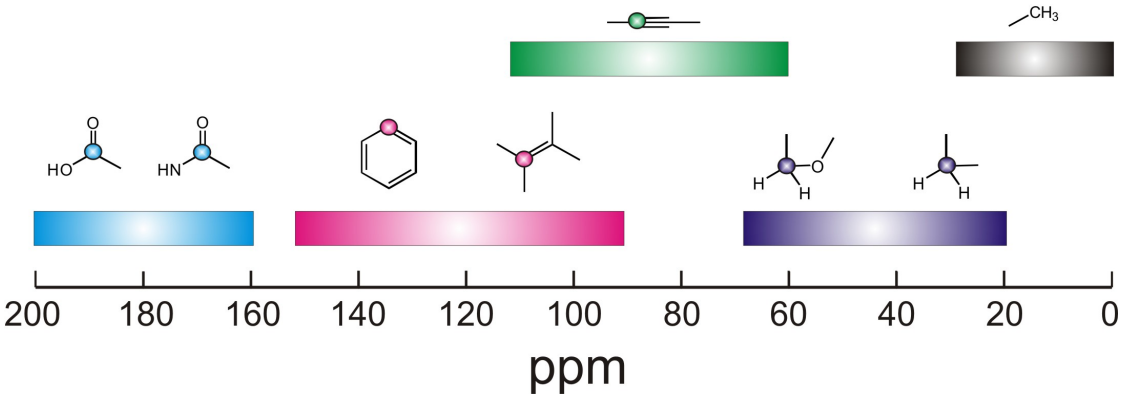

Figure 3.3.: ^{13}C chemical shift assignment for important structural components present in molecules studied in this work.[33]

From solid-state NMR spectra, information far beyond the chemical shift can be obtained. Specifically, line widths of the NMR signal contain useful information about the local molecular order. Broad lines indicate a rather amorphous structure, while narrow lines indicate a more crystalline structure. This is due to the fact that amorphous structures contain molecules with a variety of conformational orientations. Since each

orientation gives rise to a slightly different chemical shift, a broad line results for an amorphous sample.[34,35]

Another nucleus studied by the CP/MAS technique, is ^{15}N which is even less abundant than ^{13}C. Only systems with high nitrogen contents in close proximity to protons can be measured, but still long measuring times are necessary to obtain spectra with acceptable signal-to-noise-ratios. However, the chemical shift range of ^{15}N is broader than the chemical shift range of ^{13}C. Thus, the ^{15}N is even more sensitive to structural changes.[36]

3.2. Advanced 2D NMR Methods

The basic idea behind a 2D NMR measurement is not to plot the frequency against the intensity like in a 1D spectrum but to correlate different frequencies. A general scheme for 2D NMR is shown in Figure 3.4.

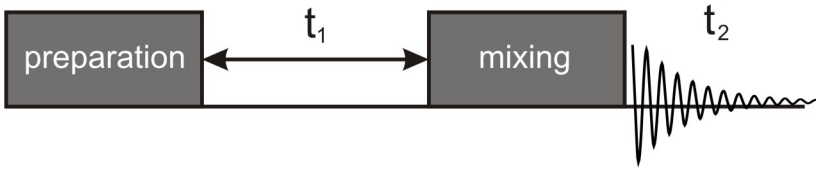

Figure 3.4.: Typical design of a 2D NMR pulse sequence

The first step of every 2D measurement is the preparation, which in the easiest case could be just a 90° pulse to generate transversal magnetization. During the evolution time (t_1), no pulses are applied and the generated coherence can evolve. Note that t_1 is not fixed but incremented in systematic steps and varied in a series of separate experiments (cf. Figure 3.5).

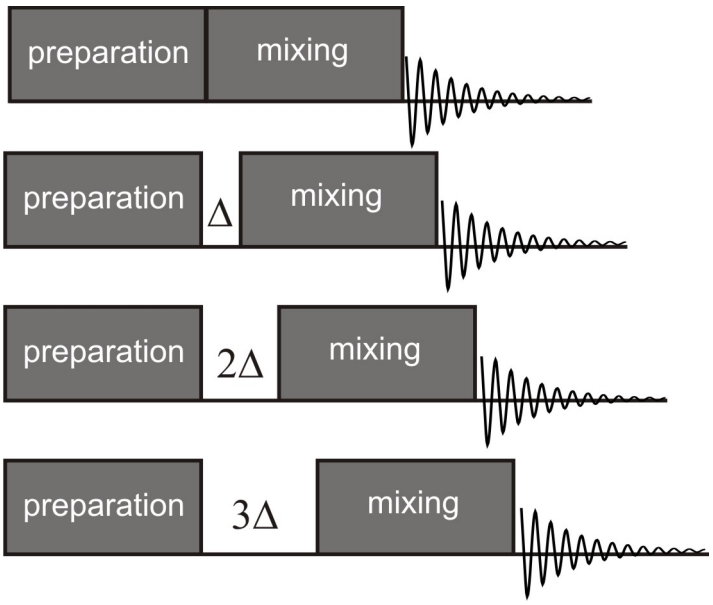

Figure 3.5.: Scheme of FID detection in the indirect dimension.

This process makes 2D experiments compared to a normal 1D experiment rather time consuming, but constitutes the basis for the FID detection in the indirect dimension of the corresponding 2D spectrum. With each t_1 increment, one point of the indirect FID is recorded. During the mixing time, the magnetization is manipulated into an observable signal, which is measured during the t_2-time and leads to the direct dimension of the 2D spectrum.[5] Data processing and hence Fourier transformation have to be done with respect to both times t_1 and t_2. The corresponding 2D spectrum is obtained after processing both FIDs.

3.2.1. Coherence Order

Another important aspect, especially for 2D NMR techniques, is the coherence order of an operator. In general, the coherence order is defined by what happens to a particular operator upon application of a z-rotation by an angle ϕ. Operators with zero quantum coherence (ZQC), like the $\hat{I}_z$ operator, are unaffected by such a rotation. The coherence orders +1 (single-quantum coherence, SQC) and +2 (double-quantum coherence, DQC) correspond to rotations by angles -ϕ and -2ϕ, respectively. Examples for operators with SQC are the $\hat{I}_x$ or $\hat{I}_y$ operators. The $\hat{I}_{1x}\hat{I}_{2y}$ operator is an example for a DQC operator. Higher order coherences require a coupled spin system. Further, the

coherence order can only be changed by pulses. This is exemplified via a double quantum (DQ) filtered correlation spectroscopy (COSY) experiment and the corresponding coherence transfer pathway scheme shown in Figure 3.6.

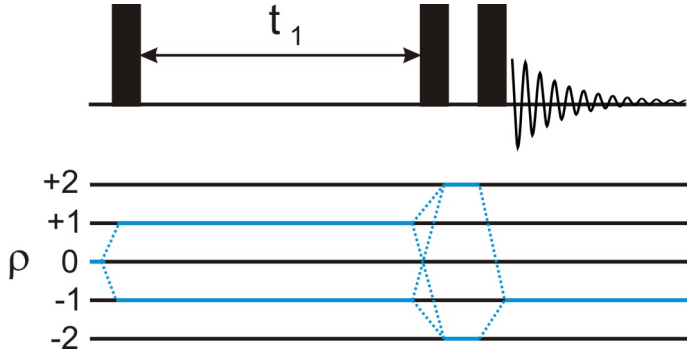

Figure 3.6.: Coherence transfer pathway of a DQ filtered COSY.

Starting point is the longitudinal magnetization along the z-axis, which has a coherence order of zero. After the first 90° pulse, the magnetization is flipped to the transversal plane and the coherence order changes to ± 1. During the delay time without any pulses, the coherence order is unchanged but the spin system can evolve due to the presence of couplings, to antiphase coherence ($\hat{I}_{1x}\hat{I}_{2z}$). If now a $\pi/2$ pulse is applied to antiphase coherence, double-quantum coherence is generated, which has to be transformed back to an observable coherence order of -1 by a third $\pi/2$ pulse.[5] Double-quantum coherence is a useful tool for many applications since it contains information about a coupled spin system and information about spatial proximities in the sample via underlying dipolar couplings. In an equilibrium spin state, DQ transitions are forbidden. However a spin system in a magnetic field is not in an equilibrium state and those transitions are partially allowed.[12] DQC can selectively be utilized in a 2D spectrum, since DQC can be selected among all coherence orders by a procedure termed phase cycling.[5,7]

3.2.2. ^{1}H–^{1}H DQ–SQ MAS NMR Using Back-to-Back Recoupling

A rather easy and relatively fast measureable 2D experiment is a ^{1}H–^{1}H correlation.

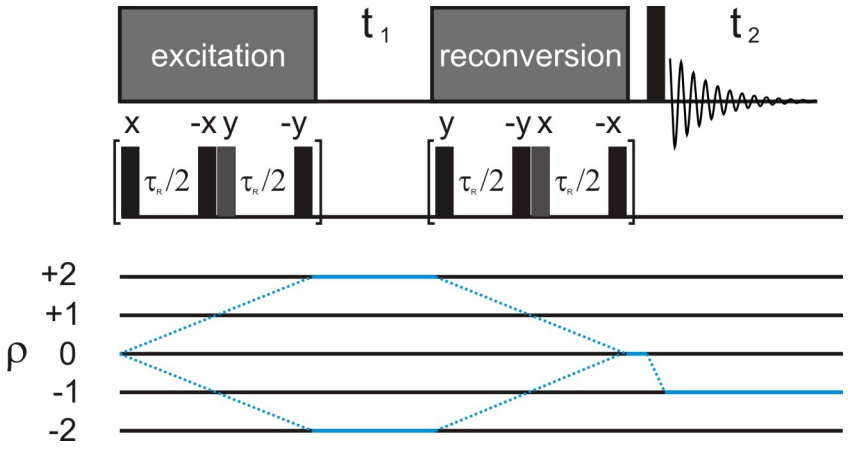

Figure 3.7.: Pulse sequence and coherence transfer pathway diagram for a ^{1}H–^{1}H DQ–SQ MAS NMR experiment using the BABA recoupling sequence for excitation and reconversion of DQCs.[16]

One way to increase the selectivity of such an experiment is to include a double-quantum filter (DQF). DQ filtering is based on DQC, which in case of a solid relies on the existence of dipolar coupled spins. However, in the solid state under MAS conditions, the dipolar coupling between the protons, which is necessary for generating DQC, is mostly averaged out. Hence, special recoupling techniques are necessary, which were already introduced in section 2.4. A recoupling of the homonuclear dipolar coupling can be achieved via a pair of orthogonal $\pi/2$-pulses. The whole process of dipolar recoupling and DQC generation is done during the excitation step of the back-to-back (BABA) pulse sequence (Figure 3.7).[12,16,37] During the incremented t_1-time, the DQC evolves before reconversion to the initial spin state, which is normally longitudinal magnetization. This reconversion is the crucial part of the pulse sequence. It is based on a time inversion of the initial sequence, which was used to excite the DQC. Finally, a single 90° rf pulse creates observable transverse magnetization, which is detected during the t_2-time.[16] Fourier transformation yields a 2D spectrum. The direct dimension contains the single-quantum dimension and the indirect dimension the double-quantum dimension (Figure 3.8). Diagonal peaks in the spectrum result from so-called like spins with identical chemical shifts. Cross peaks reflect couplings among unlike spins with different chemical shifts.

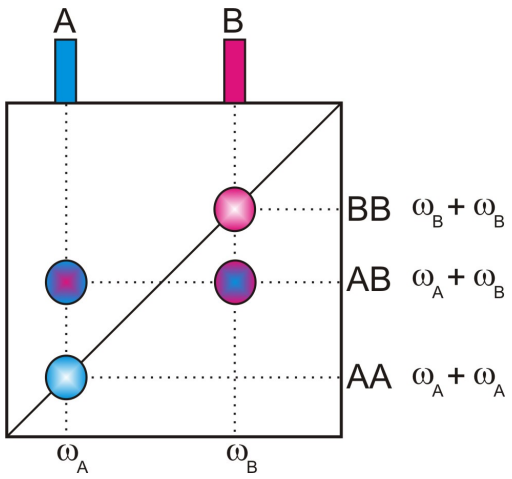

Figure 3.8.: Scheme of a 2D ^{1}H–^{1}H DQ–SQ MAS NMR spectrum.[11]

This technique is based on the dipolar coupling, interacting through space. Thus it is not limited to intramolecular contacts and allows detailed insights in the local structure and packing. It is also possible to retrieve information about internal mobilities. If these mobilities are on the timescale of the DQ filter, the signal of the mobile species vanishes in spectrum.[12]

3.2.3. REPT-HSQC

A second relatively inexpensive 2D NMR experiment in terms of measurement time is a ^{13}C/^{1}H recoupled polarization-transfer heteronuclear single-quantum correlation (REPT-HSQC). Its main advantage, over the ^{1}H–^{1}H DQ–SQ MAS NMR experiment described above is that a ^{13}C spectrum is detected in the direct dimension. The ^{13}C spectrum has a much larger chemical shift range and therefore provides a better resolution, which can also improve the resolution of the proton spectrum in the indirect dimension. The corresponding pulse sequence is shown in Figure 3.9.

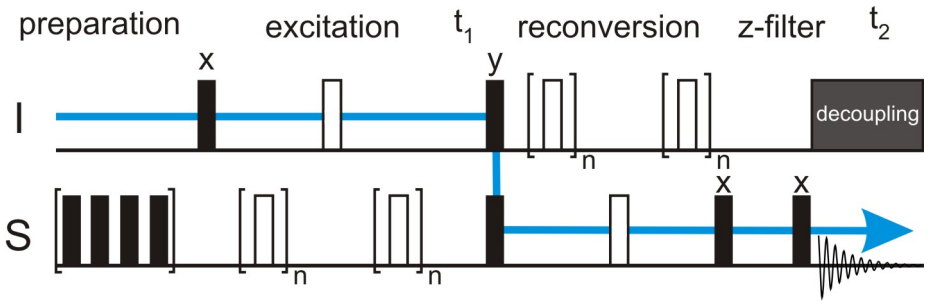

Figure 3.9.: Scheme of a 2D ^{13}C/^{1}H REPT-HSQC experiment.[38]

Within the preparation, a series of 90° saturation pulses are applied on the S channel. The experiment starts with an initial 90° *x*-pulse on the I channel, which flips the longitudinal magnetization in the transversal plane. The resulting –*y* magnetization evolves under the action of a REDOR pulse train (see section 2.4) to reintroduce the heteronuclear dipolar coupling.

$$-\hat{I}_y \longrightarrow -\hat{I}_y \cos(N_{rcpl}\Phi_0) - 2\hat{I}_x\hat{S}_z \sin(N_{rcpl}\Phi_0) \tag{3.2}$$

The number of rotor periods for recoupling is controlled by a loop counter N, which is defined as N = 2n. During the t_1-time the gained antiphase coherence (-$2\hat{I}_x\hat{S}_z$) can evolve. At the end of the t_1 period, it is transferred from the I-spin (^{1}H) to the S-spin (^{13}C) by application of two 90° *y*-pulses parallel on the I and the S channel.

$$\begin{aligned} -2\hat{I}_x\hat{S}_z \sin(N_{rcpl}\Phi_0) \xrightarrow{\Omega_1 t_1} & -2\hat{I}_x\hat{S}_z \sin(N_{rcpl}\Phi_0)\cos(\Omega_1 t_1) \\ & - 2\hat{I}_y\hat{S}_z \sin(N_{rcpl}\Phi_0)\sin(\Omega_1 t_1) \end{aligned} \tag{3.3}$$

$$\begin{aligned} -2\hat{I}_x\hat{S}_z \sin(N_{rcpl}\Phi_0)\cos(\Omega_1 t_1) \xrightarrow{90°\,\hat{I}_y/\hat{S}_y} & -2\hat{I}_x\hat{S}_z \sin(N_{rcpl}\Phi_0)\cos(\Omega_1 t_1) \\ & + 2\hat{I}_z\hat{S}_x \sin(N_{rcpl}\Phi_0)\cos(\Omega_1 t_1) \end{aligned} \tag{3.4}$$

Afterwards, another REDOR pulse train is applied. Thus, the recoupled dipolar coupling evolves the antiphase coherence back to observable $\hat{S}_x$ magnetization. In the *z*-filter period, the magnetization is stored along the *z*-axis and all unwanted magnetization dephases. After applying another 90° pulse, the $\hat{S}_z$ magnetization is flipped back to the transversal plane where the signal is detected.[39] The advantage of the REPT-HSQC sequence is that the polarization transfer is a coherent transfer and thus more distance selective than pulse sequences solely based on CP. Hence, it is possible

to qualitatively distinguish between different distances and different CH_n groups by variation of the recoupling time. This is illustrated in Figure 3.10 where the intensities of different CH_n groups are shown with respect to different recoupling times.

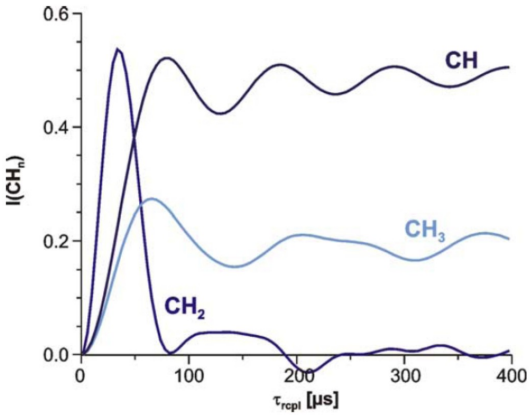

Figure 3.10.: Building up of ^{13}C signal intensities of different CH_n groups as a function of the REPT dipolar recoupling time.[12]

It should be noted that, e.g. CH_2 groups are only observable when applying a rather short recoupling time. In general the signal intensity of CH_3 groups is decreased compared to CH groups. This yields, rather useful information about the studied system.[12]

3.2.4. FSLG-Decoupled CP HETCOR

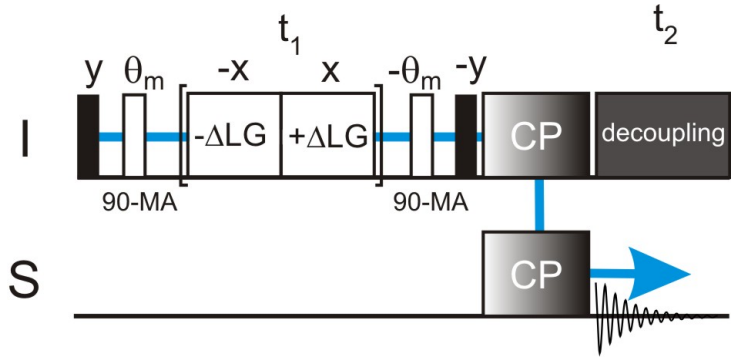

Figure 3.11.: Scheme of a 2D $^{13}C/^{1}H$ FSLG-decoupled CP HETCOR.

Another $^{13}C/^{1}H$ correlation pulse sequence, besides the REPT-HSQC described above, is the frequency switched Lee–Goldburg (FSLG) decoupled CP heteronuclear correla-

tion (FSLG-decoupled CP HETCOR) sequence shown in Figure 3.11. At the beginning of the pulse sequence, the magnetization of the protons is flipped to the transversal plane by a 90° *y*-pulse, followed by a pulse, which flips the magnetization vector into a plane inclined by the magic angle with respect to B_0. This measurement is based on the decoupling of homonuclear dipolar couplings of protons achieved by the FSLG technique which was described in section 2.3.2. This decoupling technique is performed during the t_1-time and results in a highly resolved proton spectrum in the indirect dimension of the corresponding 2D spectrum. After the evolution period, the proton magnetization is flipped back by a –*y*-pulse, which turns any component perpendicular to the LG pulse back into the *xy* plane and which will bring the spin-locked component back to the *z*-axis. Finally proton magnetization is transferred to carbon magnetization by CP, which is detected during the t_2-time.[40]

This measurement leads to an increased proton resolution in the indirect dimension of the 2D spectrum. Due to the fact that the transfer is less selective, it is possible to detect weak interactions with a reasonable signal-to-noise-ratio using a smaller amount of scans compared to the REPT-HSQC technique. However, the spectral width in the indirect proton dimension has to be rescaled in the resulting 2D spectrum. This rescaling should be calibrated on a known sample for the specific spectrometer but is conveniently done by a factor of $1/\sqrt{3}$. Further, the chemical shift value has to be changed manually and is normally referenced to the 1D ^{1}H spectrum.[16,39]

3.2.5. REPT-HDOR

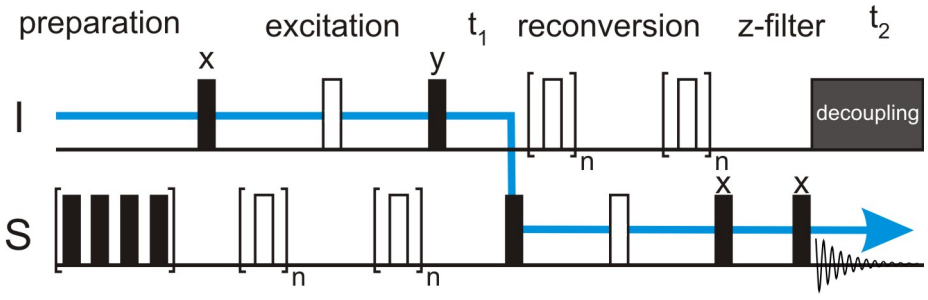

Figure 3.12.: Scheme of a 2D ^{13}C/^{1}H REPT-HDOR experiment.[39]

The recoupled polarization transfer-heteronuclear dipolar order recoupling (REPT-HDOR) pulse sequence shown in Figure 6.18 is rather similar to the REPT-HSQC

pulse sequence, which was introduced in section 3.2.3. The excitation block leads to a transversal magnetization of the protons, which is gained after a 90° x-pulse. This can evolve under the influence of the recoupled heteronuclear dipolar coupling to the antiphase coherence $2\hat{I}_x\hat{S}_z$. Deviating from the REPT-HSQC sequence a 90° *y*-pulse is applied on the I channel leading to longitudinal magnetization in the form of $2\hat{I}_z\hat{S}_z$. This longitudinal magnetization does not evolve during the t_1-time. Hence, no chemical shift information is available in the indirect dimension of the corresponding 2D spectrum. Another difference compared to the REPT-HSQC sequence is that the t_1-time is not incremented in multiples of the rotor period but in steps smaller than one rotor period ($\Delta t_1 < \tau_R$). Thus, the indirect dimension is not incremented rotor-synchronized and a sideband pattern is obtained. These sideband patterns only include information about the heteronuclear dipolar coupling. After the t_1-time another 90° pulse is applied to the S channel to obtain antiphase coherence in analogy to the REPT-HSQC experiment.[39,41,42]

The data available form a REPT-HDOR measurement is different compared to the 2D methods introduced above, since no chemical shift information is available in the indirect dimension. The hetero nuclear dipolar sideband pattern of each resolved carbon nucleus, allows to extract the magnitude of the dipolar coupling constant between the carbon atom and the corresponding proton. Therefore, one slice of the data set is Fourier transformed with respect to the t_2-time (Figure 3.13). This FID is replicated N times to gain a longer FID and avoid truncation effects. The corresponding data set is then Fourier transformed with respect to the t_1-time. The resulting sideband pattern can be fitted with special routines to retrieve the magnitude of the dipolar coupling constant.[12,16,42]

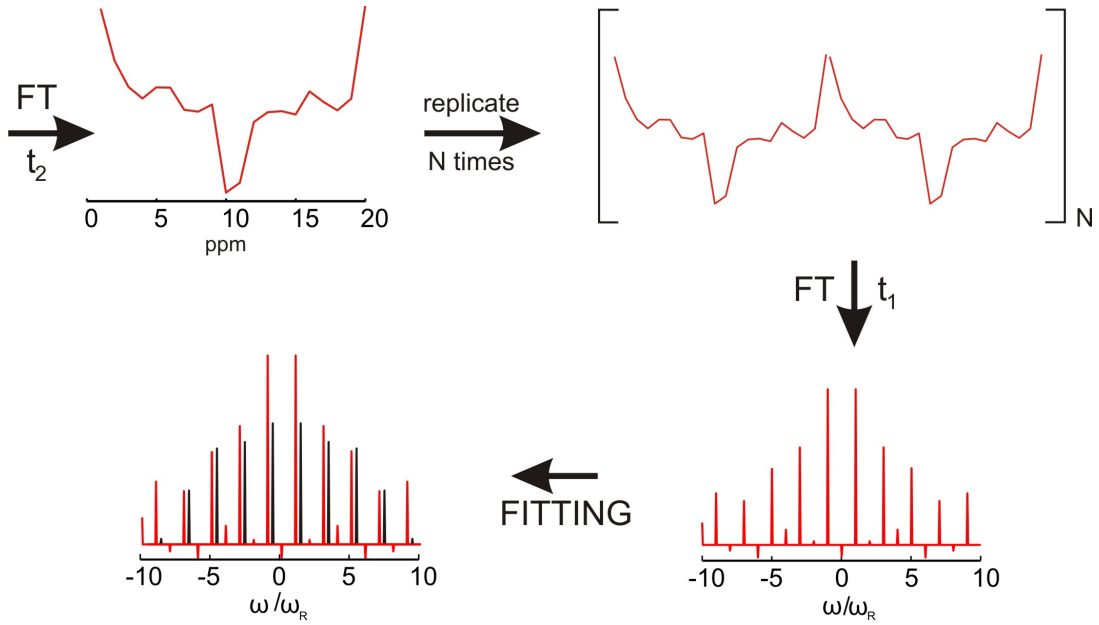

Figure 3.13.: Data processing of a slice of a REPT-HDOR measurement. After replication and Fourier transformation the obtained sideband pattern is fitted to retrieve the dipolar coupling constant.

REPT-HDOR measurements are especially suitable for CH groups due to significantly reduced multispin interactions. From the extracted dipolar coupling constant, quantitative information about the internal mobility of the system is available, since the dipolar coupling constant decreases with increasing mobility. The dynamic order parameter S for a specific carbon site in a specific molecule can be gained from the ratio of the dipolar coupling constant for the rigid case (21 kHz) and the measured value.[42]

$$S = \frac{D_{measured}}{D_{rigid}} \tag{3.5}$$

According to this definition, the order parameter is in the range of 0–1 where 1 is completely rigid and 0 is completely mobile. In addition it is possible to convey the kind of mobility present in the system.[43,44]

4. Shape-Persistent Macrocycles

Large conjugated π-systems, with attached alkyl chains, have received rising interest due to possible applications in the field of organic electronics.[45] Hence, it is necessary to generate structures with a high degree of intra- and intermolecular order, since structural imperfections strongly influence the observed properties. To deepen the understanding of how the order of a supramolecular system could be systematically controlled, a macrocycle model system based on phenylene-ethynylene units functionalized via alkyl chains is studied in this chapter. The advantage of this kind of material is that it organizes spontaneously in ordered assemblies of an extended size.[46,47] Due to its monodispersity all studied structural features can be directly related to the properties of the molecule and not to defects in the aggregated structure.[45] This study focuses on the self assembly of such a system based on non-covalent interactions like π–π-stacking and the driving force for the phase separation due to different chemical properties of the building blocks. In particular the influence of alkyl chains is studied in detail since they affect, besides the solubility and the melting behavior, the liquid crystallinity of the system.[48,49] According to the literature liquid-crystallinity plays a decisive role for the order of the structure.[50–52] With these considerations, two macrocycles with similar rigid backbones and different substituted alkyl side chains are studied in more detail with solid-state NMR, wide-angle X-ray scattering (WAXS), and differential scanning calorimetry (DSC).

4.1. Shape-Persistent Macrocycles Based on Phenylene-Ethynylene Units

The investigated shape-persistent macrocycles (SPM), which are based on a rigid backbone of phenylene, ethynylene, and benzodithiophene units attached with alkyl chains, are shown in Figure 4.1.

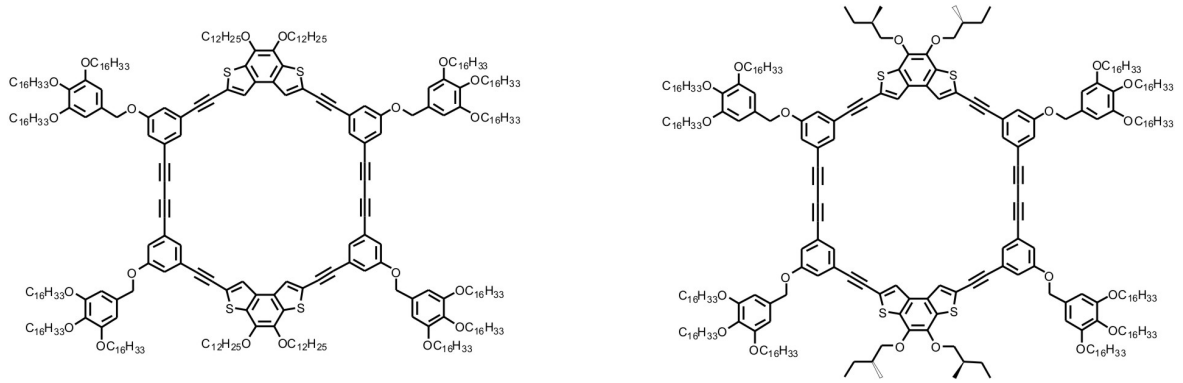

SPM-1 SPM-2

Figure 4.1.: Chemical structures of the macrocycles SPM-1 and SPM-2.

All alkyl chains bonded to the phenylene rings consist of C-16 chains for both macrocycles. The structures of both macrocycles differ in the kind of alkyl chain, which is attached to the benzodithiophene unit. SPM-1 contains unbranched C-12 alkyl chains while SPM-2 has shorter C-4 alkyl chains with a methyl branch and therefore also a stereogenic center. These minor changes in the structure impose strong effects on the properties of the macrocycles as shown by DSC in Figure 4.2. For SPM-1, three endothermic peaks at 22, 109, and 151°C are observed in the DSC heating curve. In contrast the heating curve of SPM-2 shows two endothermic peaks at 33 and 160°C only. All processes are reversible and give rise to exothermic peaks in the corresponding cooling curves.[53]

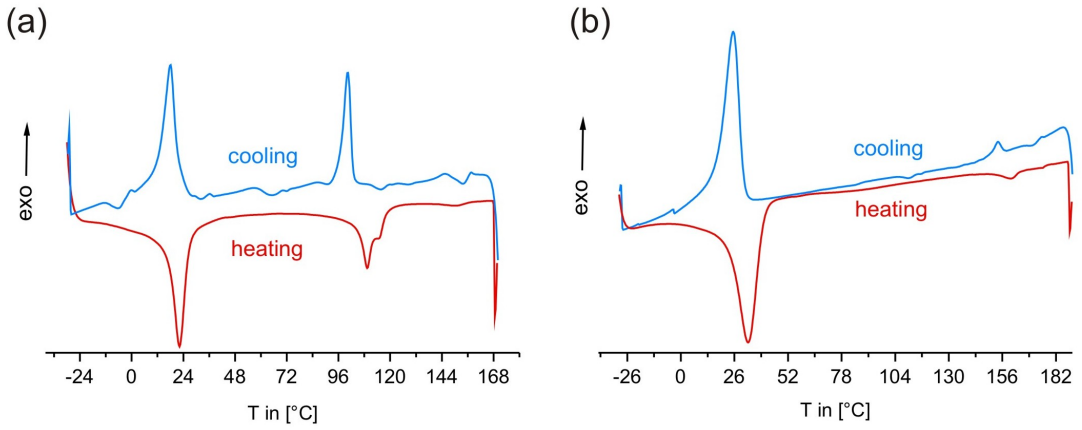

Figure 4.2.: DSC curve of (a) SPM-1 and (b) SPM-2.[53]

A first assignment of the peaks in the DSC curves can be done via polarization optical microscopy (POM). The endothermic peaks at 22°C (SPM-1) and 33°C (SPM-2) can

be assigned to the transition from a crystalline to a liquid-crystalline phase, probably due to the melting of the alkyl chains. In addition, it is possible to assign the peaks at 151°C (SPM-1) and 160°C (SPM-2) to the transition from a liquid-crystalline phase to an isotropic phase. The peak at 109°C observed for SPM-1, is a transition between two liquid-crystalline phases.

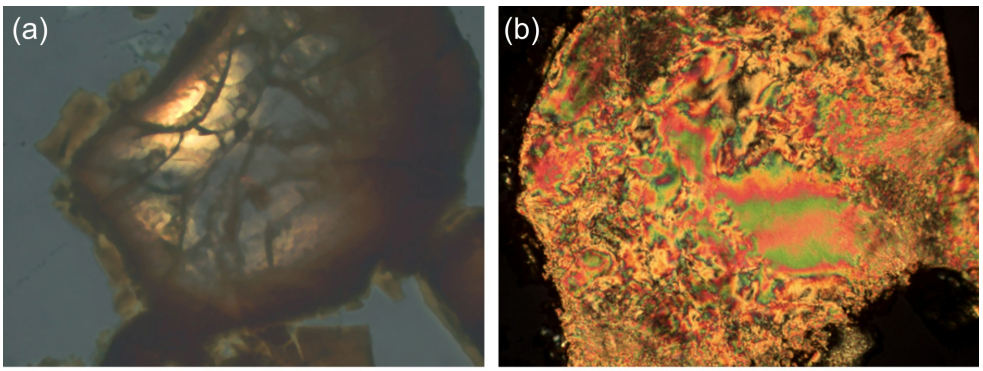

Figure 4.3.: POM images of SPM-1 at (a) 23°C (below the phase transition) and (b) at 92°C within the liquid-crystalline phase.[53]

However, with POM it is only possible to identify liquid-crystalline phases as such, but a detailed characterization cannot be achieved. Thus, WAXS was utilized for a more detailed analysis. It was found that SPM-2 forms a liquid-crystalline phase in a broad temperature range with a hexagonal ordering of the columns. In contrast, SPM-1 exhibits two liquid-crystalline phases. Upon cooling of the isotropic phase, a rectangular-columnar phase was found which changes upon further cooling below 109°C to a hexagonal phase similar to the liquid-crystalline phase assigned for SPM-2. A disordered, soft crystalline phase is obtained below 22°C.[53] It is surprising that SPM-1 and SPM-2 are able to form liquid-crystalline phases at all, since these systems have an empty void in the center of the molecule. It was expected that due to the frustration between molecular anisotropy and the empty space insight the ring, the system is prevented from forming stable thermotropic mesophases.[54] Hence, the understanding of the aggregation and stacking behavior of SPM-1 and SPM-2 is of great interest. In the next section, solid-state NMR is applied to deepen the understanding of the molecular ordering involved.

4.2. Aggregation and Phase Behavior of SPM-1

First, solid-state NMR was applied to gain a deeper insight into the first phase transition of SPM-1, which was observed via DSC at 22°C. ^{13}C $\{^1H\}$ CP/MAS NMR was performed slightly below and above the phase transition. The corresponding spectra are shown in Figure 4.4. A rough assignment of the resonance can be done in the following way: 10–40 ppm alkyl chains, 70–80 ppm OCH_2 groups, 80–100 ppm alkyne carbon atoms, 110–140 ppm aromatic carbon atoms, and ∼150 ppm quaternary aromatic carbon atoms bonded to oxygen (cf. Figure 3.3). This assignment is further refined within this section via 2D NMR techniques, but already without an exact assignment of the resonances useful information can be retrieved.

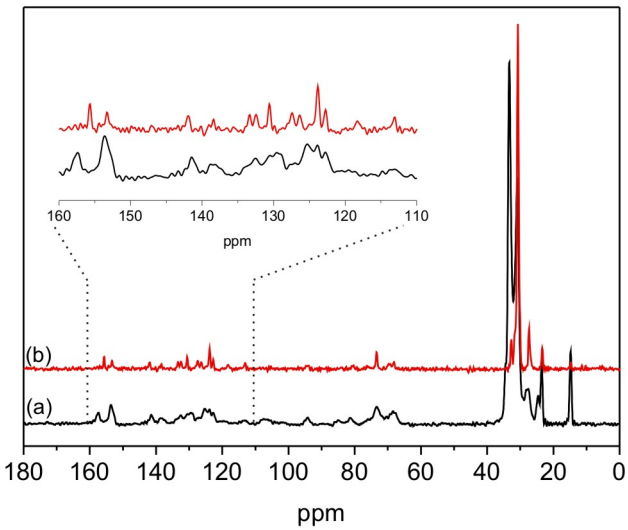

Figure 4.4.: ^{13}C $\{^1H\}$ CP/MAS NMR spectra of SPM-1 (a) at 295 K (black) and (b) at 340 K (red).

Below the phase transition, two intense resonances occur in the alkyl region at 33.3 and 30.8 ppm. Above the phase transition, only one resonance remains at 30.7 ppm. This indicates that the first phase transition can indeed be assigned to a melting of the alkyl chains as the alkyl chemical shifts at 33.3 and 30.8 ppm are averaged to 30.7 ppm upon the increase in temperature. The higher local mobility of the alkyl chains also influences the aromatic region. All resonances in the ^{13}C $\{^1H\}$ CP/MAS NMR spectrum are better resolved above the phase transition, which is indicative of

an increased local order. It can be noted that the spectrum at 340 K displays thirteen well resolved resonances for aromatic carbon atoms (inset Figure 4.4). However, the chemical shift values above the liquid-crystalline transition are hardly influenced by the phase transition apart from one resonance at 157.3 ppm, which is shifted up field to 155.6 ppm. Since these resonances are also observed in solution, the values gained from solution- and solid-state NMR are compared in Table 4.1.

δ **(in ppm) liquid**	δ **(in ppm) solid**	Δ
158.5	155.4	**3.1**
153.6	153.0	0.6
142.9	141.8	1.1
138.2	137.9	0.3
134.8	133.3	1.5
131.5	132.2	-0.7
130.7	130.4	0.3
127.9	127.5	0.4
124.5	126.2	-1.7
123.1	123.8	-0.7
122.8	122.6	0.2
118.7	118.2	0.5
106.15	112.6	**-6.5**

Table 4.1.: Chemical shift values for the aromatic carbon atoms of solution- and solid-state NMR.

Table 4.1 underlines the remarkable resolution observed in the ^{13}C $\{^1H\}$ CP/MAS NMR spectrum of SPM-1. Only in rare cases, it is possible to observe the same number of resonances in the solid state as in solution. This strongly indicates that the solid-state packing of SPM-1 is highly ordered. Further the ordering should be completely symmetric so that all aromatic groups are undistinguishable within the macrocycle. In addition, the chemical shift values are in good agreement. Only two values show a larger deviation due to the influence of packing on the chemical shift value in the solid state, e.g., via π–π-stacking interactions.

To study the transition into the liquid-crystalline phase in further detail, ^1H MAS NMR was performed. The corresponding spectra are shown in Figure 4.5. Similar to ^{13}C $\{^1H\}$ CP/MAS NMR, the ^1H MAS spectra underline the structural differences before

and after the phase transition. At 295 K (below the phase transition) three resonances at 6.4 ppm (aromatic protons), 3.9 ppm (OCH_2 protons), and 1.5 ppm with a shoulder at 1.1 ppm (alkyl protons) are observable.

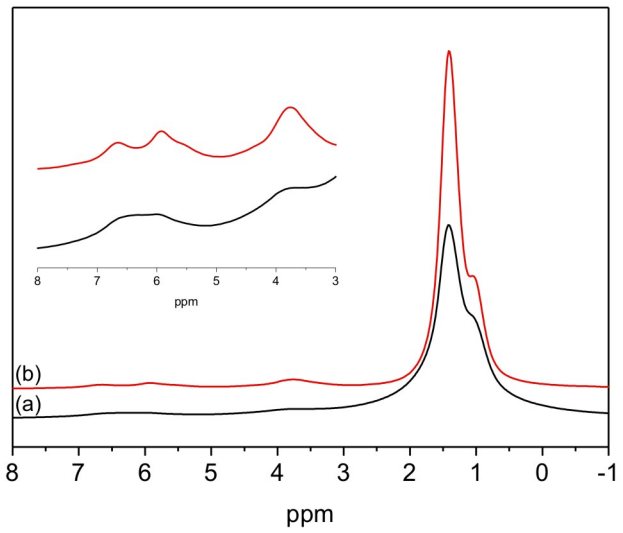

Figure 4.5.: ^{1}H MAS NMR of SPM-1 (a) at 295 K black and (b) at 330 K red.

Above the phase transition (330 K), the alkyl resonance is narrowed substantially from a line width of 440 Hz to 220 Hz. This supports the assumption that the alkyl chains are melting during the phase transition. Moreover, the resolution is improved like in the ^{13}C $\{^{1}$H$\}$ CP/MAS NMR spectrum. Specifically the resonance at 6.4 ppm is splitted into three resonances at 6.8 ppm, 6.0 ppm, and 5.5 ppm (cf. inset of Figure 4.5). These different chemical shift values indicate the presence of π–π-stacking interactions in the local packing. A strong shift of a resonance up field is indicative of strong π–π-stacking interactions, i.e. the aromatic proton of one layer is located above the aromatic ring of another layer.[11,28]

The second phase transition is more difficult to study. A ^{13}C $\{^{1}$H$\}$ CP/MAS NMR spectrum at 380 K did not contain any peaks beside the strong alkyl resonance at about 30 ppm. This indicates that the second phase transition causes an increased mobility of the inner aromatic rings, which disturbs the conditions for cross polarization from ^{1}H to ^{13}C. Thus, all further studies were limited to the liquid-crystalline phase occurring above 22°C and below 109°C. Deeper insights into this phase could be gained by advanced 2D NMR techniques. ^{13}C/^{1}H correlation techniques like the FSLG-decoupled

CP HETCOR sequence turned out to be advantageous because the proton resolution in the indirect dimension is improved. Since a CP step is included it is in principle possible to control the observable distance via the contact time. Hence, the FSLG-decoupled CP HETCOR has been measured twice, once with a rather short contact time of 0.5 ms (data not shown) and with a longer CP contact time of 3 ms. The spectrum with the shorter contact time allows to identify carbon atoms with directly bonded protons. This information turns out helpful for a later assignment. The spectrum with a longer contact time of 3 ms contains information about carbon atoms of the whole macrocycle. The corresponding 2D spectrum of SPM-1 is shown in Figure 4.6.

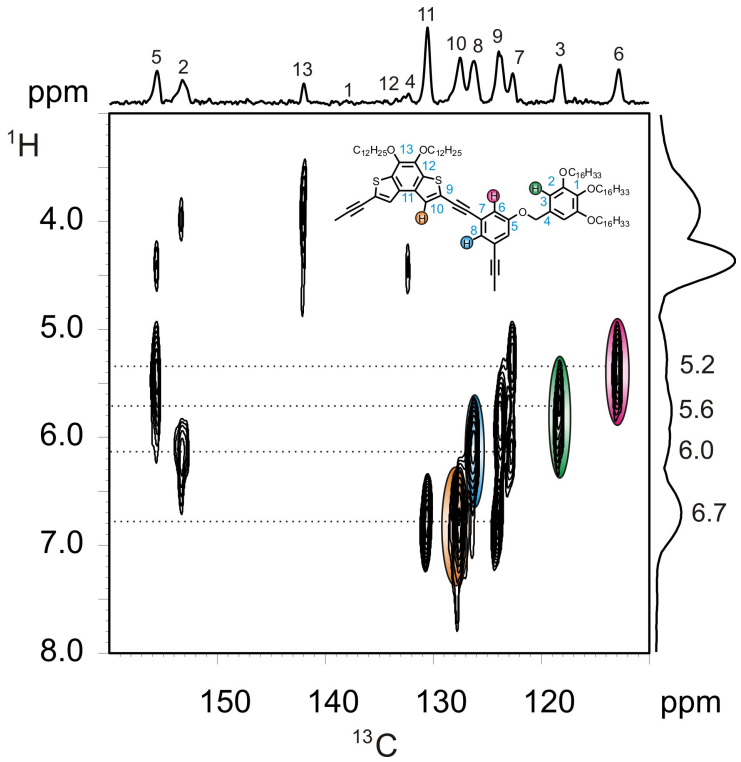

Figure 4.6.: ^{13}C/^{1}H FSLG-decoupled CP HETCOR of SPM-1 measured at 330 K, 15 kHz MAS and a contact time of 3 ms.

This 2D spectrum shows the ^{13}C projection in the direct dimension and the ^{1}H spectrum in the indirect dimension. Since the resolution in the indirect ^{1}H dimension is improved by FSLG decoupling, all different kinds of aromatic protons of SPM-1 are resolved and appear at 5.2 ppm, 5.6 ppm, 6.0 ppm and 6.7 ppm. The chemical shift value of 5.2 ppm indicates that this particular proton is influenced by strong π–π-stacking interactions. With the aid of the FSLG-decoupled CP HETCOR spectrum measured with a shorter contact time, each aromatic proton can be assigned to its

directly bonded carbon atom. This assignment (δ_{iso} (^{1}H), δ_{iso} (^{13}C): 6.7 ppm, 127.5 ppm; 6.0 ppm, 126.1 ppm; 5.6 ppm, 118.2 ppm; and 5.2 ppm, 112.8 ppm) is marked with a color code (cf. Figure 4.6). Notably the proton, which exhibits the strongest π–π-stacking, is correlated with the carbon atom, which has the largest chemical shift difference compared to the solution state. This indicates that identical aromatic rings within the macrocycles are not stacked on top of each other but with a slight angular pitch. The remaining assignments, are shown in Figure 4.6 and illustrated with the chemical structure of the macrocycle. The resonances of the carbon atoms 1, 4, and 12 are not observable in the 2D correlation. This is probably due to the fact that the distance to neighbored protons is not suitable for CP.

Further knowledge about the packing is gained via another 2D ^{13}C/^{1}H correlation experiment, the REPT-HSQC. The corresponding spectrum of SPM-1 is shown in Figure 4.7.

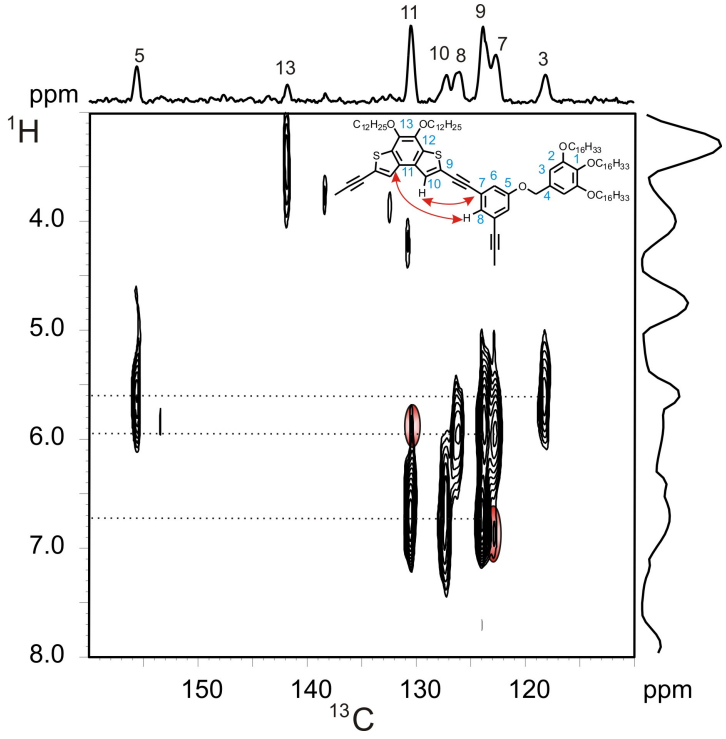

Figure 4.7.: ^{13}C/^{1}H REPT-HSQC of SPM-1 measured at 330 K, 25 kHz MAS and four rotor periods recoupling. Intermolecular correlations are marked in red.

In this experiment, the polarization transfer, from the protons to the carbons is different compared to CP HETCOR technique. Here the polarization transfer is achieved via recoupling of dipolar couplings, which have the advantage that the transfer is

even more distance selective and can be directly controlled with the recoupling time. However, this method is rather time consuming and long measuring times are often required for spectra with a suitable signal-to-noise-ratio.

The correlation peaks of the FSLG-decoupled CP HETCOR (Figure 4.6) and the REPT-HSQC correlation spectra are rather similar. In the REPT-HSQC spectrum, two additional correlations marked in red see Figure 4.7 can be noticed. Since these peaks can be assigned to intermolecular proximities they contain additional information on the stacking. The aromatic protons of the benzodithiophene unit (6.7 ppm) are weakly correlated towards the aromatic carbon atom 7 of the inner aromatic ring. Additionally, the proton connected to the inner aromatic ring at 6.0 ppm is correlated to the aromatic carbon atom of the benzodithiophene unit (11). Both correlations are visualized in the chemical structure shown in Figure 4.7 by the red arrows. Although illustrated as intramolecular interaction it should serve as guide to the eye to understand the intermolecular arrangement. These correlation peaks indicate a stacking where the macrocycle of one layer is rotated by an angle of about 60° with respect to the next layer (cf. Figure 4.8 (a)).

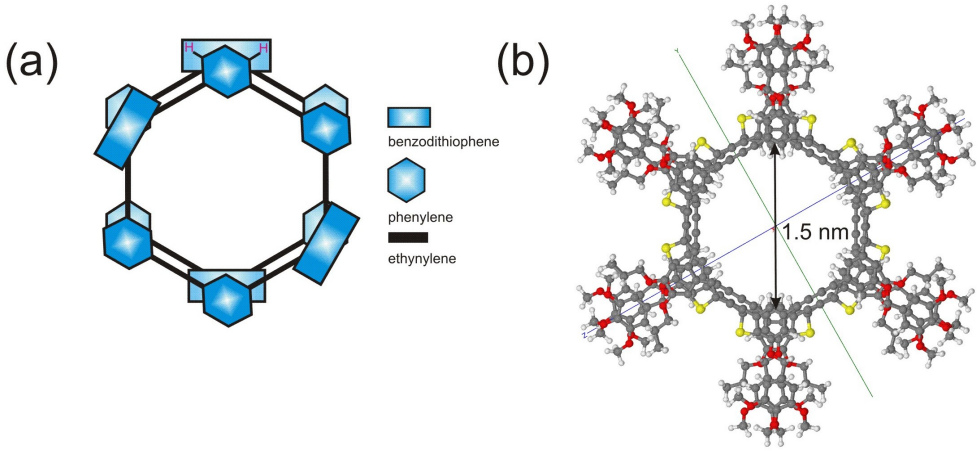

Figure 4.8.: Stacking behavior of SPM-1: (a) theoretical calculation with a pitch angle of 60° and (b) schematic overview.

Hence, the inner phenylene ring of one layer is above the benzodithiophene unit of the next layer. This configuration places the outer protons of the inner phenylene ring (marked in red see Figure 4.8 (a)) on top of the aromatic moiety of the benzodithiophene unit and strong π–π-stacking interactions and a proton chemical shift value of 5.2 ppm can occur. Within the columnar stack the next macrocycle is again rotated by

a pitch angle of 60° and hence a helical columnar packing is formed. It is expected that all macrocycle units within a column are stacked without further drifts on top of each other (cf. Figure 4.8 (b)) . Considering this kind of stacking all aromatic units are equivalent which is one important requirement of the packing.

A confirmation of the suggested pitch angle of 60° can be gained via theoretical DFT calculations. The packing of the whole system has been studied using single molecule units with C_{2h} symmetry optimized at the B3LYP/6-31+G** level. Within the model the molecules have been composed with the pitch angle of 60° and a interlayer distance of 3.5 Å. Neglecting infinite stacking effect of the aromatic units, it becomes sufficient to investigate a stack of 3 molecules. The first and third molecule represents the shielding effect, which the second molecule is exposed to. Thus, taking computed ^{1}H NMR chemical shift values for a isolated macrocycle and applying to it the nuclear independent chemical shift (NICS) maps of the first and third molecules (depicted in Figure 4.9) it is possible to estimate the shift values of the second molecule within the stack.

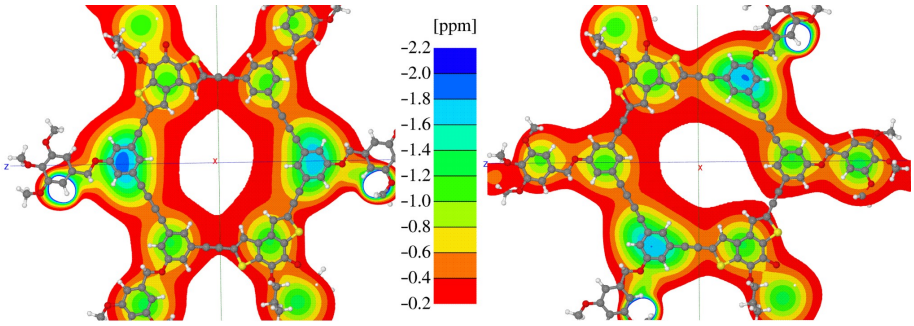

	δ_{iso} solution	influence of packing	δ_{iso} solid calculated	δ_{iso} solid observed
^{1}H benzo-dithiophene unit (orange)	7.7	-0.8	6.9	6.7
inner ^{1}H phenylene unit (blue)	7.2	-1.4	5.8	5.9
outer ^{1}H phenylene unit (red)	6.9	-1.6	5.3	5.2

Figure 4.9.: NICS map of SPM-1 with a pitch angle of 60° and a comparison of the corresponding calculated and measured proton chemical shift values. The first and third molecule represents the shielding effect, which the second molecule is exposed to.

Since the stack has a helical arrangement and thus all molecules in it are equivalent, the final chemical shift values are characteristic for the whole stack. Hence it is possible to understand the chemical shift values in the solid-state in comparison to the solution-state NMR. From the NICS map the corresponding values of the upper and the lower macrocycle are added to the solution-state chemical shift values. The obtained chemical shift value, which includes then packing related information can be compared to the measured ones. A detailed comparison has been done for the protons of the benzodithiophene unit (marked in orange Figure 4.6) and the inner phenylene ring (marked in blue and red Figure 4.6). The corresponding values are summarized in the Table see Figure 4.9. Indeed, the calculated and observed values are in remarkable agreement, which emphasizes the suggested pitch angle, of 60°.

As another 2D NMR technique to understand the packing of SPM-1, the ^{1}H–^{1}H DQ–SQ correlation sequence was used to reveal proton–proton proximities. The corresponding spectrum is shown in Figure 4.10.

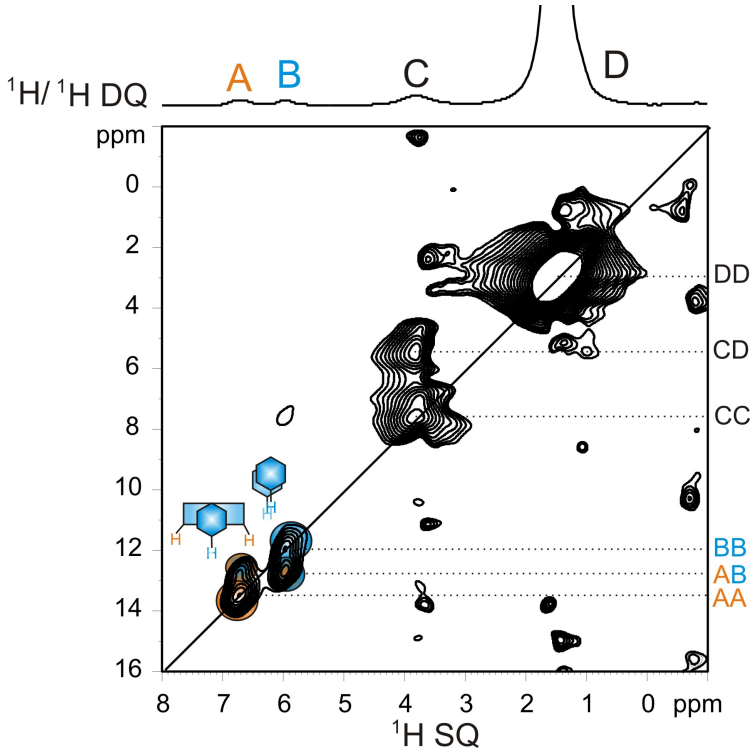

Figure 4.10.: ^{1}H–^{1}H DQ–SQ correlation of SPM-1 measured at 330 K, 25 kHz MAS and one rotor period recoupling.

In the proton projection of the 2D spectrum, four resonances are observable: two aromatic resonances at 6.7 ppm (assigned to the benzodithiophene protons, orange)

and 6.0 ppm (inner protons of the inner phenylene ring, blue), the OCH_2 protons at 3.7 ppm, and a broad alkyl resonance at about 1 ppm. Since the other two aromatic resonances at 5.6 and 5.2 ppm are not observed, one can conclude that the corresponding protons are isolated in the packing, i.e., no DQ coherence can be generated with the recoupling time of one rotor period. The 2D spectrum contains six correlation peaks. Three correlation peaks (marked in black) are due to intramolecular proximities. Three further peaks can be found in the aromatic region. The benzodithiophene protons (orange) give rise to one auto peak in the aromatic region, since both protons of one unit are in a close proximity. This auto correlation peak is marked with AA. AB and BB cannot be explained via intramolecular proximities. Hence, they are due to intermolecular proximities and contain information about the stacking. Both peaks AB and BB can be easily understood with the already proposed pitch angle of 60° between adjacent macrocycles. A rather helpful illustration of the intermolecular proton proximities is shown in the cut-out from the theoretically calculated packing shown in Figure 4.11.

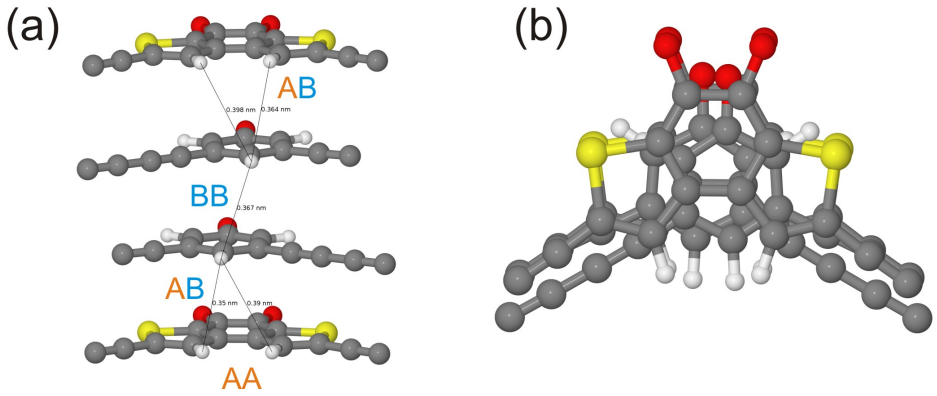

Figure 4.11.: Cut-out of the stacking of SPM-1 (a) from a side view and (b) from a top view.

One aromatic building block is chosen and the packing of the next four layers is illustrated. It can be noticed that in every fourth layer the packing is repeated. Especially the side view of this packing shown in Figure 4.11 (a) points out the observed proton proximities. AB as well as BB can be understood and are marked in the corresponding Figure. The stacking distances between the particular layers which are also available from the theoretical calculation fits with the proximities which are able to observe in the ^{1}H–^{1}H DQ–SQ correlation with respect to the used measuring conditions. Hence also ^{1}H–^{1}H DQ–SQ correlation confirms the proposed stacking with the pitch angle of

60°.

To gain further insight into the SPM-1 system, the local mobility was quantitatively studied. Via the REPT-HDOR method, the $^{13}C/^{1}H$ dipolar coupling constant could be determined. CH-groups and the other carbon atoms in the molecule could be selectively distinguished from each other, due to the fact that a CH-group gives rise to a characteristic line shape in the corresponding 2D spectrum. For SPM-1 four CH-groups could be identified. The dipolar coupling constants were extracted with the procedure described in section 3.2.5. The optimized side-band patterns and their simulations are shown in Figure 4.12.

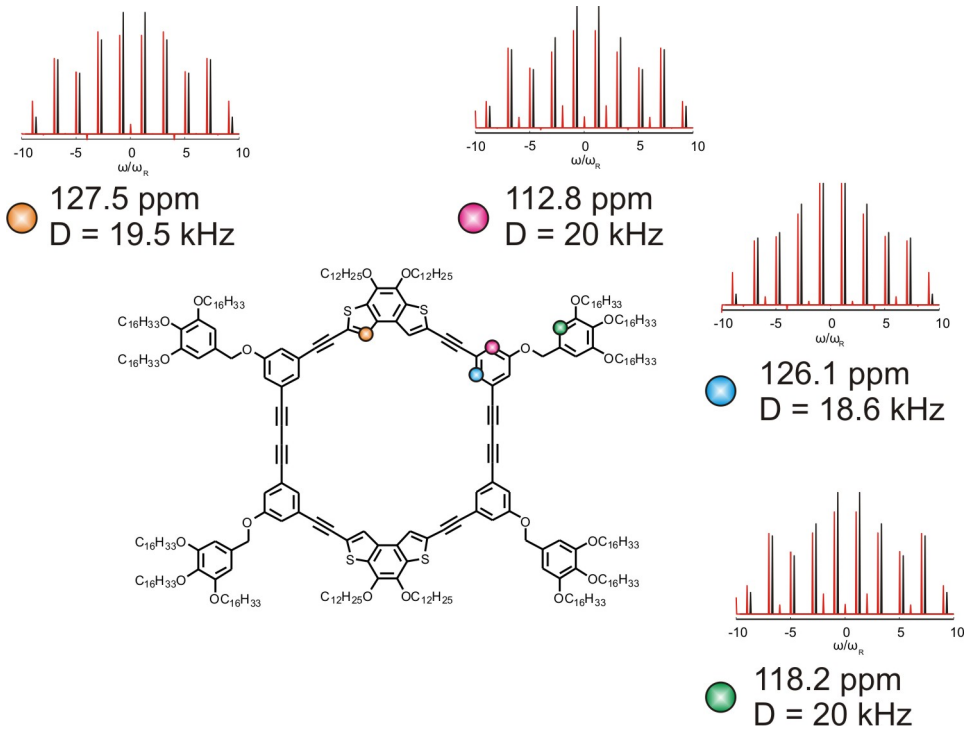

Figure 4.12.: $^{13}C/^{1}H$ REPT-HDOR dipolar side-band patterns of SPM-1. The measurement was performed at room temperature, 25 kHz MAS, and four rotor periods recoupling.

The different CH-groups, given by the color code were assigned, via the FSLG-decoupled CP HETCOR experiment discussed above. It should be noted that the aromatic ring system remains almost completely rigid above the first phase transition, although the mobility of the alky chain is increased. The rigidity of the aromatic system corroborates the previous assumption that the high spectral resolution in the ^{13}C $\{^{1}H\}$ CP/MAS NMR spectrum is due to a almost perfectly ordered crystalline structure of

SPM-1 identified now as a helical structure with 60° pitch angle and does not reflect a high local mobility. This result is in agreement with WAXS data where it was found that a highly ordered hexagonal phase is observable above 22°C. (see section 4.1).[53] In this section WAXS and solid-state NMR could identify the packing within a column. For the packing of the columns as such small angle X-ray scattering (SAXS) can be used and a distance between the columns of 53.1 Å was found.[53] The corresponding packing is shown schematically in Figure 4.13. Hence, a combination of all methods was used to understand the complex packing of SPM-1 and confirms the presence of liquid crystallinity despite the void in the center of the molecule.

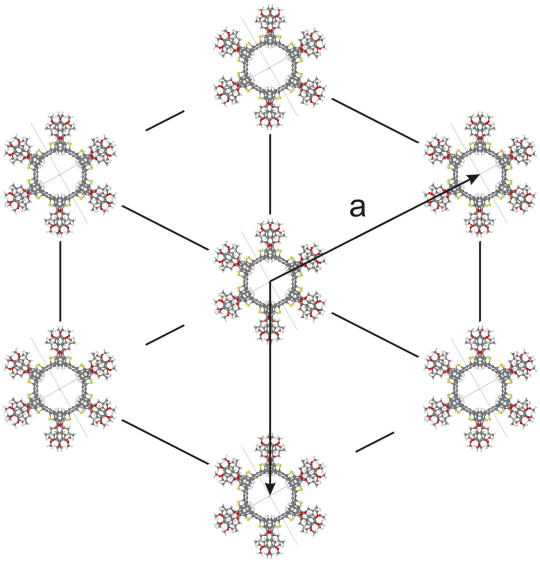

Figure 4.13.: Schematic overview of columnar arrangement within the hexagonal liquid crystalline phase with the distance a of 53.1 Å.[53]

4.3. Aggregation and Phase Behavior of SPM-2

In analogy to the investigation of SPM-1, SPM-2 is subjected to the same considerations and questions. Since both macrocycles exhibit the same kind of phase transition at about 20°C, it is expected to observe similarities in the solid-state NMR spectra of both components. To verify this expectation, a ^{13}C $\{^{1}H\}$ CP/MAS NMR measurement, which is rather sensitive to structural changes, was performed before and after the phase transition. The corresponding spectra are shown in Figure 4.14.

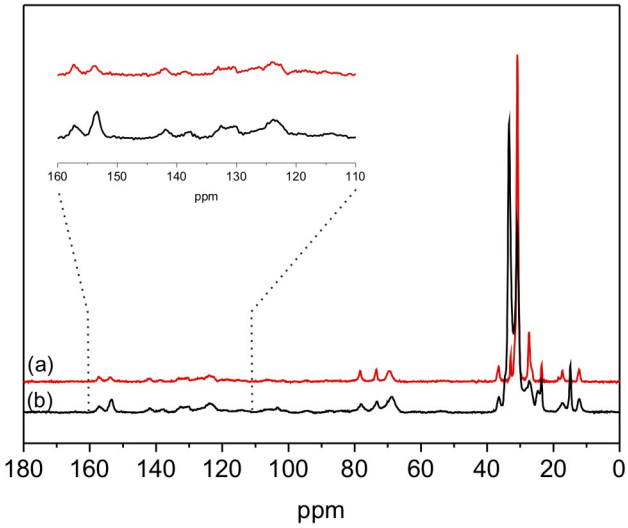

Figure 4.14.: ^{13}C $\{^{1}H\}$ CP/MAS NMR spectrum of SPM-2 (a) at 295 K (black) and (b) at 330 K (red).

The alkyl region at 20–40 ppm before and after the phase transition shows major similarities compared to SPM-1. At 295 K, two peaks at 33.7 ppm and 30.5 ppm are resolved. In the spectrum at 330 K, only one resonance remains, which indicates a melting of the alkyl chains and an averaging of the chemical shifts. However, the aromatic region of SPM-1 and SPM-2 differ substantially from each other after the phase transition. For SPM-1, it could be shown that the local order in this region is improved dramatically (cf. Figure 4.4). In contrast the ordering of SPM-2 does not improve at all. This is surprising, since in both cases similar processes are observed in the alkyl region. Counter intuitively, an impact on the local order of the whole macrocycle is observable only for SPM-1. This conclusion is also corroborated by the ^{1}H MAS spectrum, which illustrates that the order of SPM-2 is not comparable with SPM-1 (cf. Figure 4.15).

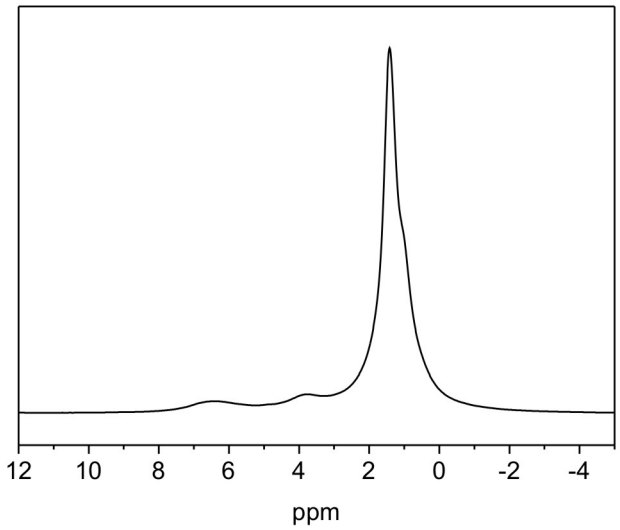

Figure 4.15.: ^{1}H MAS NMR spectrum of SPM-2 at 330 K.

Above the phase transition temperature at 330 K only three peaks are resolved and are located at 6.4 ppm, 3.8 ppm, and 1.4 ppm. The resonance at 6.4 ppm is rather broad and originates from overlapping signals of aromatic protons with and without π–π-stacking interactions. Due to lack of resolution, further information cannot be acquired from the spectrum. In addition a REPT-HDOR spectrum was recorded to obtain information about the local mobility. One resonance in the aromatic region of the spectrum allowed to extract the typical line shape of a CH group. The corresponding sideband pattern and the fit are shown in Figure 4.16.

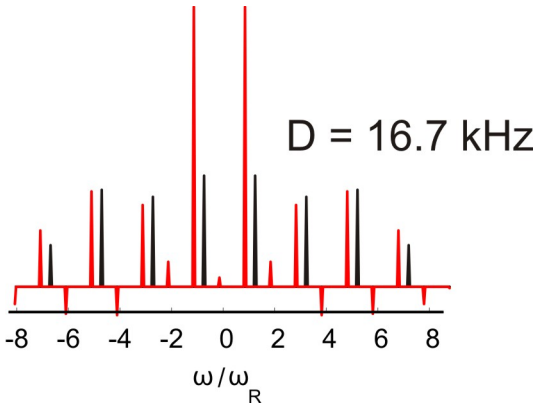

Figure 4.16.: ^{13}C/^{1}H REPT-HDOR dipolar sideband pattern of the ^{13}C resonance at 125.5 ppm of SPM-2.

Although an exact assignment of the resonance to a certain carbon atom of SPM-2 is not possible, it is probably related to an inner aromatic ring, due to the chemical shift value. The extracted dipolar coupling constant of 16.8 kHz indicates that the aromatic ring system of SPM-2 is more mobile than the ring system of SPM-1. This fundamental difference in structural organization is most probably related to a difference in space filling. For SPM-1 the long, unbranched alkyl chains attached to benzodithiophene provide for a better space filling than the shorter and branched alkyl chains of SPM-2. Thus, the local order of SPM-2 is decreased since more degrees of freedom to move within the columnar stack prevail. In contrast, SPM-1 is able to organize, after the first phase transition, in perfectly aligned columns. These are stabilized via long alkyl chains, which fill efficiently the space between different columns. Similar observations have been found for benzotricarboxyamide were the liquid-crystalline behavior for the system substituted with unbranched alkyl chains is different compared to the system with branched and shorter alkyl chains.[51] However, the major impact on the structural order is probably not the branching of the chains but the length which has to be suitable. In the literature also systems are described where the branched alkyl chains lead to better ordered structures.[55]

4.4. Conclusion

Via the comparison of SPM-1 and SPM-2 it could be shown that the kind of alkyl chains imposes a rather important effect on both structure and local order. This effect is not limited to the solubility and the melting behavior. Already tiny changes of the alkyl chains can have major effects on the structure. However, it is not trivial to predict, which kind of alkyl chains influences the system in which direction. The unbranched longer alkyl chains bonded to SPM-1 are able to stabilize the corresponding macrocycle in highly ordered hexagonal columns. The rings are stacked within the column on top of each other with a pitch angle of 60°. π–π-stacking interactions are present between the rings and the whole system is found to be rather rigid. In addition, SPM-1 is able to form a second liquid-crystalline phase, which is not present for SPM-2 and which was not studied in detail by solid-state NMR. SPM-2, despite the same liquid-crystalline phase transition, does not form an ordered columnar stack. The aromatic rings show an increased local mobility and a decreased order. In conclusion, for the design of an ordered supramolecular systems with an extended π-system, the right choice of the

attached alkyl side chains is crucial.

5. Conductive Polymers Based on Polythiophenes for Organic Photovoltaics

The predictable exhaust of fossil energy resources and the proceeding climate change increases the motivation for research in renewable energy sources like wind power, water power, and the sun, e.g., in form of photovoltaic cells.[56,57] Despite the fact that theoretically six hours of sunshine in the dessert are sufficient to satisfy the whole energy demand of the world for one year, only less than 0.1% of our energy is gained by photovoltaics. The main reason for this is that the photovoltaic cells which are available at the moment are mainly based on inorganic materials like silicon. These devices have served advantages like a high energy conversion efficiency about 15 to 20% and an expected life time up to thirty years. However, the fabrication of these devices is rather expensive. Without subsidies, photovoltaic cells are hardly profitable and their usage is limited. The high costs originate from the fact that already during the recovery of elementary silicon, needed for such devices, a huge amount of energy is required. Therefore, the inorganic solar cell has to run for about five years until energy conversion and consumption are balanced. These problems are tried to overcome with photovoltaic cells based on organic materials like highly conjugated polymers or oligomers. Such materials are easy and inexpensive to fabricate. Thus, the price for the final device is expected to decrease dramatically, which should open the wide use of organic-based photovoltaic cells.[58] However, these devices still have severe problems, which need to be overcome. Specifically, the efficiency of the current state-of-the-art devices is too low with values only up to 6%. Further the lifetime is limited to one year only. Another major problem relates to the reproducibility of a certain efficiency and a certain lifetime. These parameters are not predictable because the main processes responsible for the deterioration of these properties are not yet fully understood.[58] The morphology of the organic material is crucial for a high efficiency. It is affected by many parameters like the degree of regioregularity, the preparation conditions, annealing, the molecular weight, and the solvent. The morphology of two representative candidates for the use in a photovoltaic cell and the different factors, which influence their morphologies, are the focus of this chapter. The aim is to get

an increased understanding of the morphology, which can then be used to raise the efficiency of the devices in the future.

5.1. Basic Principle of a Photovoltaic Cell

The typical design of an organic photovoltaic cell is shown schematically in Figure 5.1.

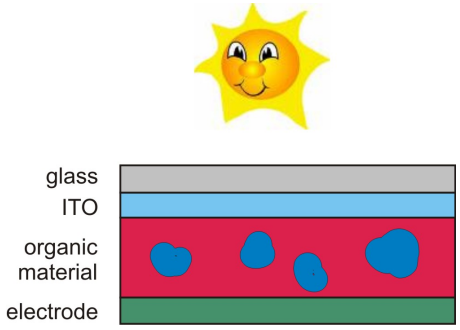

Figure 5.1.: Schematic assembly of a solar cell.

A thin glass plate is maintained on top of each photovoltaic cell to protect the device. Underneath the glass plate is a layer of indium doped tin oxide (ITO). This material has two rather crucial characteristics: a) it is conductive, hence it can be used as an electrode and b) it is transparent, which is important since the sunlight needs to reach the main part of the photovoltaic cell without substantial losses. To improve the surface quality of ITO, a thin layer of poly(ethylene-dioxythiophene) doped with polystyrene sulfonic acid (PEDOT-PSS) can be added between ITO and the organic material.[59] The next layer constitutes the heart of the solar cell, which is the organic material. This material is mostly based on a bulk-heterojunction of a donor (p-type) and an acceptor (n-type) component. The donor material constitutes of conjugated polymers and fullerenes are typically applied as acceptors. The most common representative is [6,6]-phenyl-C_{61}-butyric acid methyl ester (PCBM). Both materials are cast to a thin film of about 100–200 nm thickness via methods like spin-coating and printing techniques.[60] On the bottom of each solar cell a second electrode is mounted, which normally consists of a metal like aluminum.

The generation of a current in the photovoltaic cell is schematically shown in Figure 5.2.

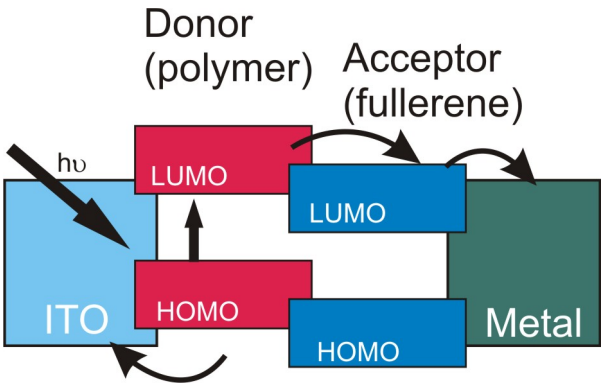

Figure 5.2.: Schematic overview of the working principle of a photovoltaic cell.

It can be explained in analogy to the valence and conduction band theory, which is used to describe inorganic semiconductors. In the organic material, the HOMO (highest occupied molecular orbital) and LUMO (lowest unoccupied molecular orbital) form bands due to the high conjugation of the system. They are treated in full analogy to valence and conduction bands of metals. By irradiation, an electron is excited from the HOMO of the donor material to its LUMO if the wavelength of the light matches the energy gap between HOMO and LUMO. This excited state is referred to as an exciton. It can be viewed as a spatially localized pair of an electron and a hole. The binding energy of the exciton is about 0.5 eV. Free charge carriers are necessary to generate a current. For this, the exciton needs to dissociate to a free electron and a hole. Hence, the formed exciton needs to migrate to the interface between donor and acceptor. This process dictates strict geometrical requirements on the device: donor-acceptor interfaces must be prevalent (occurring roughly every 10 nm) so that every created exciton may encounter an interface prior to a possible recombination of hole and electron. At this interface, the exciton is dissociated into a free electron and a hole, due to the difference between the energy levels of the donor and the acceptor. Once formed, the holes diffuse within the polymer domains. Likewise, the electrons are free to move within the fullerene domains and a current is generated. However, if the domains are isolated from the appropriate electrode or the carrier is too far from the electrode, the hole/electron pair will eventually recombine at a polymer/fullerene interface.[61–63]
The total efficiency of a device is the product of three electrical parameters: a) the short circuit voltage (I_{sc}), which is the number of photons absorbed and the efficiency of free charge carrier generation, b) the open circuit voltage (V_{oc}), which is related to the energy difference between the HOMO of the donor and the LUMO of the acceptor and contributes to a field induced drift of charge carriers, and c) the fill factor (FF),

which is a function of the efficiency of charge migration to the electrodes. These electrical parameters, divided by the incident light power density (P_{in}), describe the photovoltaic power conversion efficiency of a solar cell η_e (cf. equation 5.1).[59]

$$\eta_e = \frac{V_{oc} \cdot I_{sc} \cdot FF}{P_{in}} \tag{5.1}$$

For a single layer device, a total efficiency of 10 % can be theoretically obtained.[58,62] Most crucial for a high efficiency is the morphology of the bulk material and an appropriate domain size of the donor and acceptor material. But contrary requirements complicate the right device performance additionally. Large domains prevent for an efficient charge separation while small domains lead to a poorly connected network and increased charge carrier recombination.[58] Due to the complexity of the system and requirements these materials and devices have been subject of extensive studies, which have not, however lead to a breakthrough in the performance of these devices.[64–69]

5.2. Introduction of the Investigated Systems

The polymers with promising properties for photovoltaic devices studied in this chapter are shown in Figure 5.3.

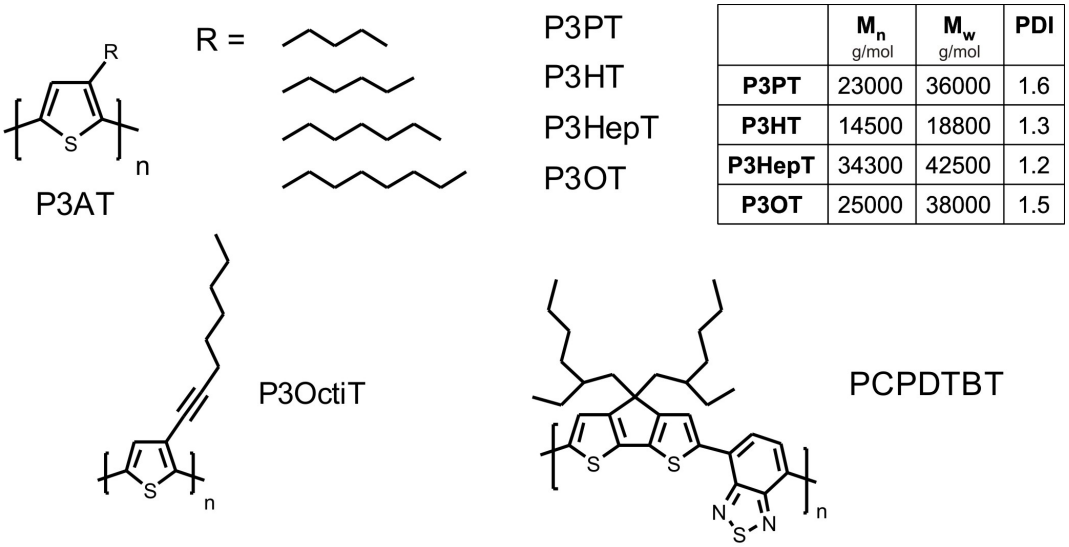

	M_n g/mol	M_w g/mol	PDI
P3PT	23000	36000	1.6
P3HT	14500	18800	1.3
P3HepT	34300	42500	1.2
P3OT	25000	38000	1.5

Figure 5.3.: Overview of the conjugated polymers in this study

The solid-state NMR studies in this chapter have first been carried out for a series

of poly(3-alkylthiophenes) (P3ATs, cf. Figure 5.3) to obtain information about their morphology. The investigated polymers contain a high degree of regioregularity with almost only head-to-tail linkages. In the literature, P3HT is widely studied, due to its promising properties, including a band gap of about 1.9 eV, a suitable absorption width, and a facile synthesis.[70–72] It is thus an important model component for different types of investigations. Further it has been shown that devices based on P3HT exhibit efficiencies of about 3–5%.[59] In addition, a P3AT derivative with a slight change of the structure, namely the insertion of a triple bond within the alkyl chain is investigated in more detail (P3OctiT). This system is of interest because it has an extended π-system and it is expected that hence the local order could be improved.

In addition, a lot of effort is devoted to find new materials with improved absorption edges to match the solar terrestric radiation, higher carrier mobilities, and a better energy alignment with the acceptor to reach high open circuit voltages.[60] The new generation of conjugated polymers for donor materials are alternating copolymers of an electron-rich and an electron-deficient building block in their backbone, like poly[2,6-(4,4-bis-(2-ethylhexyl)-4H-cyclopenta[2,1-b;3,4-b‘]dithiophene)-alt-4,7(2,1,3-benzothiadiazole)] (PCPDTBT), which is studied in the second part of this chapter. The synthesis of this polymer is more complex than that of P3ATs. However, its absorption band is improved and close to the near-IR region due to a low optical band gap of 1.4 eV.[73] This is particular promising since the majority of semiconducting polymers have band gaps higher than 2 eV which limits the theoretical efficiency to about 30%.[59] In contrast, a band gap of 1.4 eV allows to absorb 64% of the solar irradiation.[73]

The second component, which is essential for the device performance, is the acceptor (n-type component). Only a suitable ratio between donor and acceptor allows to gain free charge carriers like in inorganic photovoltaic cells. Promising acceptor materials are based on fullerene. Due to the fact that the solubility of pure fullerene is too low, fullerene derivatives like PCBM are used (Figure 5.4).[60]

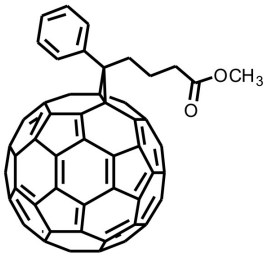

Figure 5.4.: Acceptor component in the bulk-heterojunction

The handling of all investigated polymers especially the mixtures with PCBM have been performed under exclusion of oxygen and humidity, because the large conjugated π-system and the fullerene derivative are rather sensitive.[74,75] Therefore, the sample preparation was performed in a glove box under an argon atmosphere. The solid-state NMR measurements of all samples have been performed firstly without any special treatment like annealing, for being able to investigate the influence of such conditions afterwards.
This chapter is organized as follow: first the most important studies from the literature and then the morphologies of the neat donor material are discussed. On this basis, bulk heterojunctions based on P3HT or PCPDTBT and PCBM are studied. Specifically, the morphology of the donor polymers, within the blend is in the focus. Another focus of the study is the phase separation of the bulk heterojunction upon thermal treatments.

5.2.1. Wide Angle X-ray Scattering (WAXS) Investigations

Many previous studies were focused on the impact of the morphology for the device performance in order to gain a better understanding of bulk heterojunctions like P3HT-PCBM. Especially transmission electron microscopy (TEM), atomic force microscopy (AFM), and WAXS were used to study the influence of preparation conditions on the morphology. Specifically the WAXS results are important for further solid-state NMR studies since WAXS and solid-state NMR probe on the same length scale of the sample. The solid-state NMR results obtained here are discussed with previous WAXS studies within this chapter, hence the latter are introduced in more detail. For neat P3ATs, a amorphous polymer fraction and two crystal modifications, termed as modification I and II were found.[76,77] Modification I is commonly observed and contains an orthorhombic or monoclinic unit cell. The π-system is oriented parallel to the *b*-direction and the interlayer distance is 3.8 Å. The alkyl chains are tilted away from the

thiophene backbone by an angle of 30° and are stacked along the *a*-direction. From the distance between two polymer chains within a layer, obtained from the 2θ value, it has been concluded that there is no interdigitation of the alkyl chains in modification I. Further it has been determined that the order along the *a*-axis improves with an increasing alkyl-chain length.[78]

Modification II is a structural component, which is observed less often. It shows similar structural properties as modification I but exhibits a shorter *a*-distance. This was interpreted as an interdigitation of the alkyl chains.[76,78] Also, the π–π-stacking distance is changed from 3.8 Å to 4.7 Å. This modification has been found in low molecular weight samples, which were prepared as thick films.[79] After annealing such a film, only modification I prevails.[80,81]

Fewer studies have been devoted to PCPDTBT so far. The published results were mainly focused on polymer blends with PCBM and not on the neat material. WAXS measurements of neat PCPBTBT reveal larger amorphous fractions in the polymer compared to P3ATs. The π–π-stacking distance of around 3.7 Å is similar to that of P3ATs. However, PCPDTBT is more complex due to the pendant groups, which include chiral centers and prevent the extraction of further information from the data.[82,83]

5.2.2. Previous Solid-State NMR Investigations

Although WAXS and solid-state NMR are complementary techniques only a small percentage of photovoltaic systems have been characterized via solid-state NMR until now. Further, previous solid-state NMR studies have only dealt with systems based on P3ATs. No publication could be found dealing with PCPDTBT.

Via ^{13}C $\{^1H\}$ CP/MAS NMR it was demonstrated that at different temperatures poly-(3-butlythiophene) (P3BT) and P3HT form different phases, including a plastic crystal phase, a glassy crystal phase, and a crystal phase. These have been combined in a phase diagram.[84,85] So far, only one publication tried to combine NMR and WAXS results. Here, the chemical shift values in the ^{13}C $\{^1H\}$ CP/MAS NMR spectrum were assigned to either one of the two crystal modifications. It could be confirmed that only one modification is maintained after annealing.[86] Solid-state NMR mobility studies via proton relaxation measurements could determine the amount of crystalline and amorphous phases within polythiophene. It was shown that about 62% of the morphology is crystalline, while the rest is amorphous.[87] The blend material of P3HT and PCBM

was studied as well.[88] Here, the PCBM molecules are in a close spatial proximity with the hexyl chains from the P3HT polymer after casting both components from solution. Annealing leads to a demixing of the blend and diminishes the proximities between P3HT and PCBM. Instead, the alkyl side chains of P3HT are interdigitated and PCBM has closer contacts with its own side chain. Both observations indicate that a phase separation has occurred, which leads to an increase of the local order in the P3HT and PCBM domains.[88]

The aim of this chapter is to deepen the knowledge about neat P3ATs and the P3HT–PCBM blend. This is achieved by comparing solid-state NMR results to observations from other methods, especially WAXS data. Further knowledge about the PCPDTBT polymer is gained. The retrieved data are then compared to the P3AT results. The obtained structural and dynamical data allows further insights, which will help to understand and to control the complex morphologies in such blend materials to increase the efficiency of prospective photovoltaic devices.

5.3. Aggregation and Packing of P3ATs

This section is focused on the aggregation of P3ATs (see Figure 5.3) in the bulk and the dependency on their alkyl-chain lengths. ^{1}H MAS NMR was applied to gain first insights in the system (cf. Figure 5.5). Two peaks are observable in all ^{1}H spectra: one broad peak at about 6 ppm, which can be assigned to the thiophene proton and a second peak at about 1 ppm, which can be assigned to the alkyl protons. The line shape of both peaks is rather asymmetric due to different resonances overlapping. This is remarkable since the thiophene proton is a single isolated proton and constitutes a first hint that the material is organized in two different modifications due to different packing.

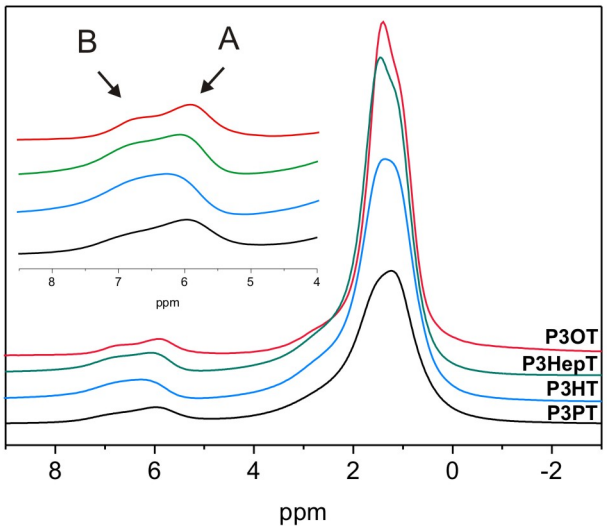

Figure 5.5.: ^{1}H-MAS NMR spectra of P3ATs with different alkyl-chain lengths.

Additional information is available from the chemical shift of the two different thiophene resonances. One resonance at 6.7 ppm is labeled modification B and the other resonance at 5.9 ppm is labeled modification A (cf. inset Figure 5.5). The proton chemical shift of modification B is comparable to that of the liquid-state signal, which appears at 6.8 ppm. In comparison, the chemical shift of modification A is shifted 0.8 ppm to a higher field, which is a hint for π–π-stacking interactions. In the case at hand the thiophene proton of one layer experiencing the aromatic ring current of the next layer. As can be seen in the inset of Figure 5.5, the two modifications are more distinct for polythiophenes with longer alkyl chains. This suggests that the local order of the thiophene backbone increases with increasing alkyl-chain length, which is in agreement with the previous WAXS investigations.[78]

This gives rise to the question if these two modifications are also observable in the ^{13}C $\{^{1}$H$\}$ CP/MAS NMR spectra. These are shown in Figure 5.6. The aromatic region in these spectra, which is of most importance for the current studies, includes five resonances: four sharp signals at 136.0, 132.7, 130.6, and 125.5 ppm, which can be assigned to the thiophene ring and one broad signal at about 140 ppm.

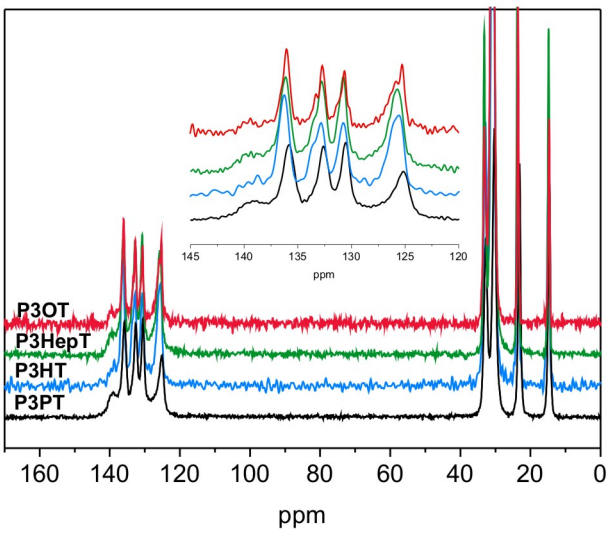

Figure 5.6.: ^{13}C $\{^1H\}$ CP/MAS NMR spectra of the P3ATs with different alkyl-chain lengths. The spectra are recorded at 25 kHz MAS and a CP contact time of 3.0 ms.

At first view, it is not possible to discern two modifications. However, the spectra of all thiophene derivatives are rather similar indicating that the same structural features are present for all P3ATs independent of the alkyl-chain length. In fact, all aromatic resonances and especially the signal at 125.5 ppm are broadened. Similar to the ^1H MAS spectra, the resolution of the ^{13}C $\{^1H\}$ CP/MAS NMR spectra is improved with an increasing alkyl-chain length. Hence, clear shoulders of the peaks at 125.5 ppm and 132.7 ppm are discernable for P3OT (cf. inset Figure 5.6).

To confirm if these shoulders denote one of the two modifications, further 2D NMR experiments were performed for all P3ATs. Due to its improved resolution, all results regarding further details of the structure are exemplified on P3OT. However, these results are also applicable to all other polythiophene derivatives since all 2D spectra look rather similar. The similarities of the ^{13}C and ^1H spectra indicate additionally a similar solid-state packing and therefore comparable structural features. The 2D $^{13}C/^1H$ FSLG-decoupled CP HETCOR correlation of P3OT is shown in Figure 5.7.

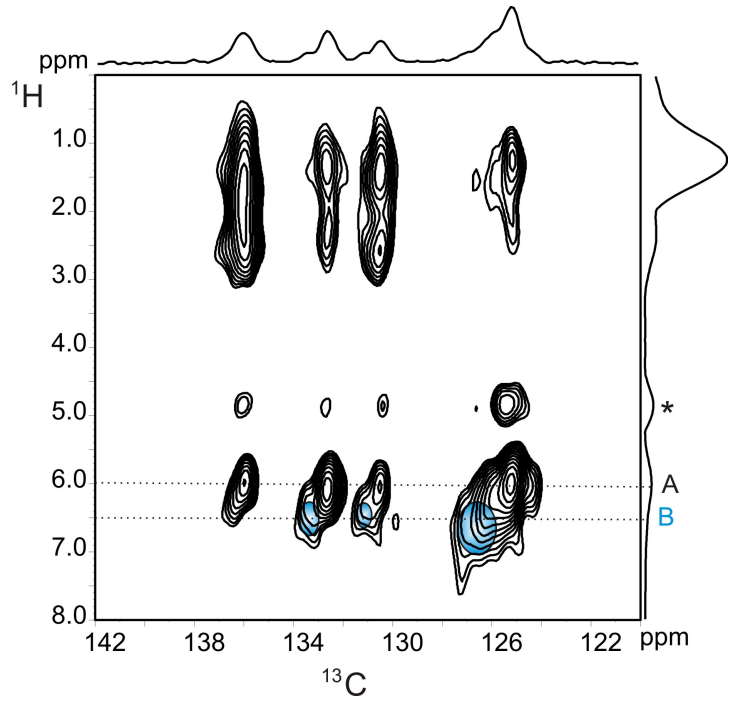

Figure 5.7.: 2D ^{13}C/^{1}H FSLG-decoupled CP HETCOR correlation spectrum of P3OT at 15 kHz MAS and a CP contact time of 3.0 ms. The asterisk indicates an artifact from the carrier frequency.

The aromatic region of the ^{13}C spectrum between 140 ppm and 120 ppm is shown in the direct dimension of the 2D plot, which can be assigned to the thiophene ring. The ^{1}H spectrum in the indirect dimension contains a resonance of the alkyl protons at about 1 ppm and the thiophene resonance at 6 ppm. In addition, a signal at 4.5 ppm is observable, which is an artifact of the measurement. Via the correlation peaks it is now possible to assign the carbon resonances to either modification A or B. The sharp signals at 136.0, 132.7, 130.6, and 125.5 ppm can be assigned to modification A due to the correlation to the proton resonance at 5.9 ppm. The carbon signals at 133.3, 131.1, and 126.8 ppm correlate to the proton resonance at 6.7 ppm and can hence be assigned to modification B. The resonance at 140 ppm is not observable in the 2D spectrum, but can probably be assigned to modification B. Notably, the carbon resonances assigned to modification B are broader than the resonances assigned to modification A. This indicates that modification B is rather amorphous compared to modification A, which has a higher local order.

From WAXS studies, it is known that annealing crucially affects the structure.[80,81] To shed light on this effect, ^{13}C $\{^{1}$H$\}$ CP/MAS NMR spectra were recorded at variable tem-

peratures (VT). The aromatic region of the corresponding spectra recorded between 300 K and 420 K is shown in Figure 5.8.

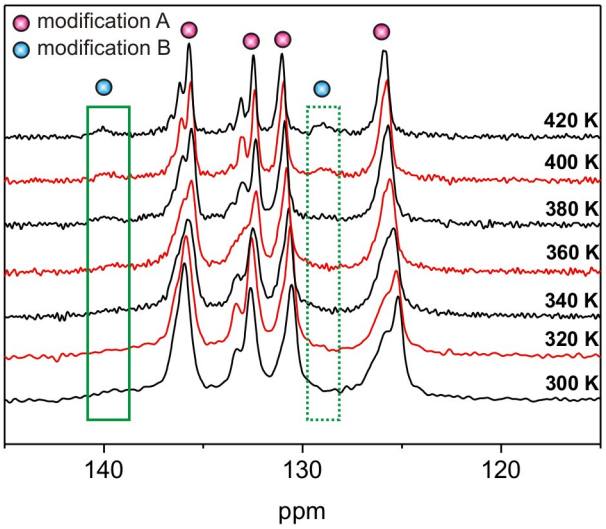

Figure 5.8.: VT ^{13}C $\{^1H\}$ CP/MAS NMR spectra of P3OT recorded in a temperature range of 300 K up to 420 K, 10 kHz MAS and a CP contact time of 3 ms.

With increasing temperature, the resonances of both modifications A and B undergo pronounced changes. Due to higher mobility at higher temperatures, the resolution of modification A is improved. Hence a splitting of the resonances especially of the peaks at 136.0 ppm and 132.7 ppm is observable. It is more difficult to detect changes for modification B in the 1D spectrum since the corresponding resonances are hardly recognizable. However, the resonance at 140 ppm can be used as a probe for modification B (see green box in Figure 5.8) to detect possible changes with respect to the temperature. With increasing temperature, the peak intensity decreases at first. At higher temperatures around 360 K, the peak can be noticed again and sharper than before. A second resonance of modification B, becomes observable at higher temperatures (128 ppm, cf. green dotted box in Figure 5.8). The slight difference of the chemical shift compared to already identified resonances for modification B in Figure 5.7, may be explained by a temperature dependency.

Still the resolution of the 1D spectrum is not sufficient. Hence a 2D $^{13}C/^1H$ CP HETCOR spectrum was measured, at 420 K (cf. Figure 5.9).

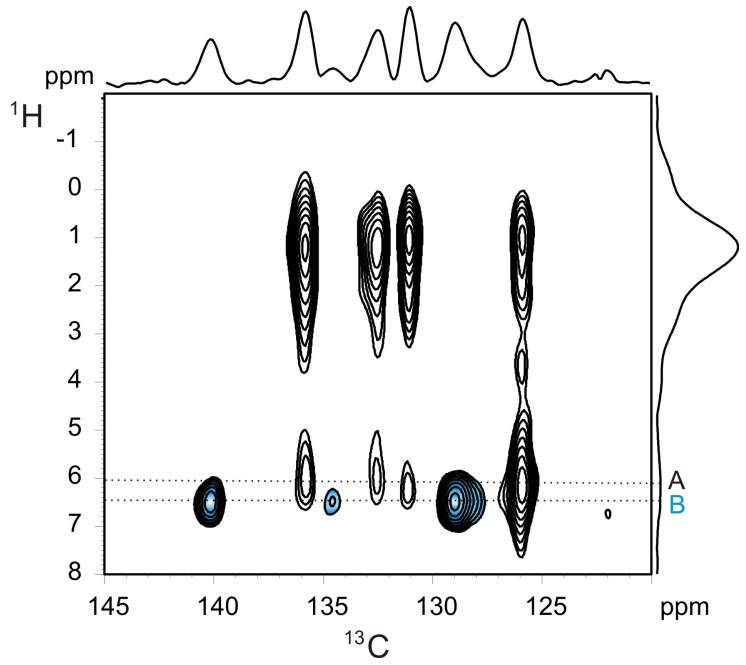

Figure 5.9.: 2D ^{13}C/^{1}H CP HETCOR spectrum of P3OT at 420 K, recorded at 10 kHz MAS and a CP contact time of 3.0 ms.

At 420 K the ^{13}C dimension of the 2D plot contains seven well-resolved peaks. The 2D ^{13}C/^{1}H correlation spectrum facilitates the assignment of the peaks to both modifications in comparison to the previous 1D measurement. The resonances assigned to modification A are rather unchanged compared to the 2D ^{13}C/^{1}H correlation spectrum at room temperature (cf. Figure 5.7). In contrast, all resonances assigned to modification B (marked in blue cf. Figure 5.9) are by far more distinct. The decrease in line broadening at higher temperatures indicates an improved local order or an increased mobility. The peak at 140 ppm, not observable in the 2D spectrum at room temperature, can be assigned to modification B. Further, the carbon chemical shifts of modification B are slightly shifted by around 1 ppm. It can be concluded that modification A is rather stable with respect to temperature changes, while modification B is more temperature-sensitive. To probe whether these changes are permanent, a 1D ^{13}C $\{^{1}$H$\}$ CP/MAS NMR spectrum at room temperature was measured after annealing (data not shown). The corresponding spectrum is almost identical to the 1D spectrum recorded before annealing. Only a marginal decrease of the resonance at 140 ppm was observable, which indicates that the relative ratio of modification B might be slightly reduced. Hence the improved resolution is most likely due to an increased mobility at higher temperatures and not due to permanent changes of the morphology. This

result can be rationalized regarding the lower local order of modification B. This reduced degree of order allows for more degrees of freedom for movements at higher temperatures. This is in agreement with the results found for macrocycles, described in Section 4.3.

To gain a deeper understanding of the aggregation and packing behavior of both modifications, a 2D ^{1}H–^{1}H DQ–SQ correlation spectrum of P3OT was recorded (cf. Figure 5.10).

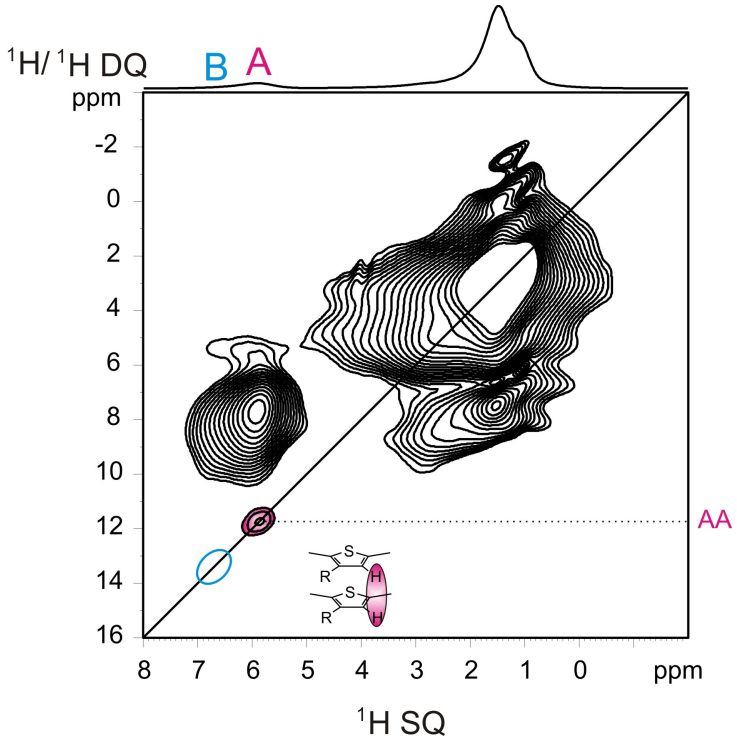

Figure 5.10.: 2D ^{1}H–^{1}H DQ–SQ correlation spectrum of P3OT measured at 25 kHz MAS and 1 τ_R recoupling.

The ^{1}H spectrum is plotted in the direct dimension of the 2D contour plot. It exhibits two resonances, which have been previously assigned to thiophene and alkyl protons. In distinction to the 1D ^{1}H MAS NMR spectrum, modification B is hardly observable in the spectrum in contrast to the resonance of modification A. The thiophene proton of modification A give rise to an auto peak (marked in red). This auto peak is not observed for modification B. The auto peak of modification A indicates a close proximity of thiophene proton pairs, which is only possible through an intermolecular coupling. Since the distance between two thiophene protons within a layer is too far to be detectable this auto peak indicates a coupling between thiophene protons of adjacent

layers (see inset Figure 5.10). With the employed measuring conditions interlayer distances of about 3.5 Å are detectable. From WAXS data an interlayer distance of 3.8 Å was found, which is in a good agreement with the present NMR data.[76,77] For modification B, such an auto peak is not observable in the ^{1}H–^{1}H DQ–SQ correlation spectrum, when a recoupling time of one rotor period is used. However, if the measuring conditions are changed towards longer recoupling times it is possible to observe also an auto peak for modification B. This indicates that modification B exhibits a larger interlayer distance then modification A.

With the knowledge gained for modification A it should now be possible to suggest a packing model. However, the question arises if all thiophene units within the packing are really stacked on top of each other with all sulfurs pointing in the same direction or if they are organized in an alternate way. In the literature both packings are discussed but the packing with an alternate arrangement of the sulfur groups seems to be preferred.[79,80,89,90] For clarifying this question theoretical DFT calculations have been performed, similar to the calculations, which have been done for the macrocycles see section 4.2. The corresponding NICS maps are shown in Figure 5.11.

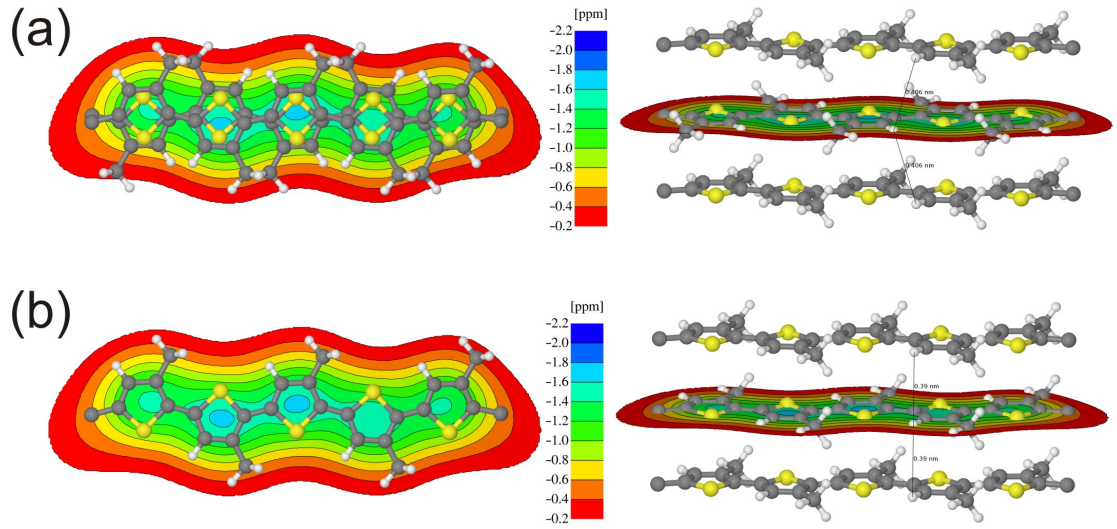

Figure 5.11.: NICS map of two possible stackings calculated for P3HT.

Two possible packing conformations could be found, where no inappropriate repulsions are present, all thiophene protons are equivalent within the packing and also the chemical shift value is adequate with the measured value of 5.9 ppm. In Figure 5.11 (a) the adjacent layer is rotated within the plane by an angle of 180° and stacked on top. In contrast Figure 5.11 (b) shows a stacking were all sulfur atoms are oriented

in the same direction. The difference between both proposed stacks is the thiophene proton distance which is for (a) 4.1 Å and for (b) 3.9 Å. Due to the fact that distances up to 3.5 Å are normally observable in a ^{1}H–^{1}H DQ–SQ correlation using a recoupling time of one rotor period the packing shown in (b) should slightly preferred. The stacking where the adjacent layers are stacked on top of each other and shifted by one thiophene unit could be excluded. Within this packing also an alternate stacking is achieved (cf. Figure 5.12), but all thiophene protons within this packing are too far away from each other for observing a correlation peak in the ^{1}H–^{1}H DQ–SQ correlation. However, this packing is widely suggested by WAXS as well as theoretical calculation.[90–95]

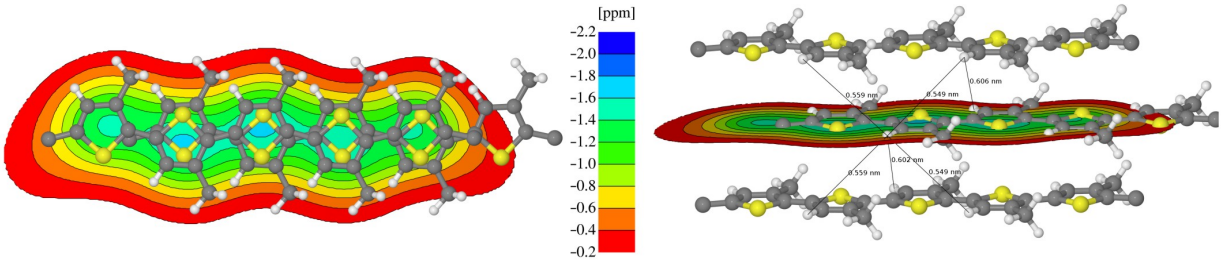

Figure 5.12.: NICS map of P3HT stacking were the adjacent layer is just put on top and shifted by one thiophene unit, which could be excluded.

Beside the morphology, the local mobility is another important parameter for the functionality of these materials. To observe the local mobility of the thiophene ring, REPT-HDOR measurements were performed. With the REPT-HDOR experiment dipolar coupling constants of CH bonds are detectable. For the thiophene group, the carbon signal at about 126 ppm was chosen. Since the dipolar coupling constant decreases, with increasing mobility the magnitude of coupling constant can be used to determine if the thiophene ring in the polymer backbone is rigid or mobile. A representative dipole–dipole side band pattern is shown for P3OT in Figure 5.13.

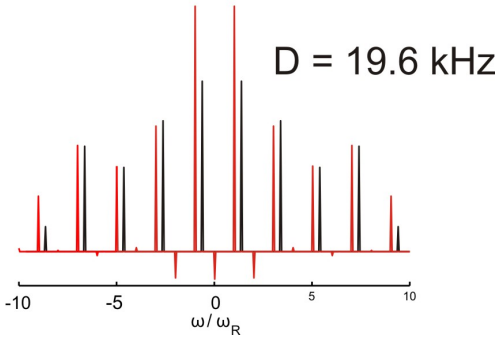

Figure 5.13.: REPT-HDOR sideband pattern of P3OT for a spectral slice at 126.3 ppm, recorded at 25 kHz MAS and 4 τ_R recoupling.

The measured data are displayed in red, the black pattern is obtained after the fitting procedure. The fitting procedure was performed on the third and fourth sideband since these are not affected by multispin interactions. Hence, a dipolar coupling constant of 19.6 kHz was extracted. The measurement and fittings were repeated for all P3ATs at 125.3 ppm for modification A and 126.3 ppm for modification B. The results are summarized in Table 5.1.

	P3PT	**P3HT**	**P3HepT**	**P3OT**
$\mathbf{D}_A$ (in kHz)	19.2	19.5	19.5	20.5
$\mathbf{D}_B$ (in kHz)	20.7	19.0	18.4	19.6

Table 5.1.: Overview of all measured dipolar coupling constants. The carbon signals at 125.3 ppm and 126.3 ppm were chosen for modification A and B, respectivly.

One should note that, the dipolar coupling constant for a completely rigid CH bond is 21 kHz and this can be used for interpreting the current results. All measured dipolar coupling constants are close to 21 kHz and reveal that the backbones of all investigated systems are rather rigid. For modification A it is observable that the mobility is decreasing with increasing alkyl-chain length. This confirms that the local packing can be improved with increasing alkyl chains and hence the degree of freedom is decreasing. This is in accordance with the results from the macrocycle were it has been found that an improved local order is related to a decrease of mobility (see section 4.1). For modification B it is not possible to observe a dependency between the alkyl-chain length and the local mobility probably due to the fact that all systems are rather amorphous.

In conclusion two different modifications were found for all P3ATs in the bulk, named modification A and B. With 2D techniques the proton resonances of each modification could be clearly assigned to the corresponding carbon resonances. The structure is rather independent from the alkyl-chain length but with increasing length the local order is improved. This is in contrast to the results found for the macrocycles in Chapter 4, where the impact of the alkyl chains towards the structure is substantially. However this difference could be explained by the fact that the ratio of the rigid block compared to the alkyl chains is for the macrocycles almost equal. In contrast, for P3ATs the size of the alkyl chains is rather short compared to the rigid polymer backbone. Also it has been found that the polymer backbone of all studied P3ATs is rather rigid and for modification A the rigidity is increasing with increasing alkyl-chain length due to the improved local order. Via ^{1}H MAS NMR it could be shown that the packing of both modifications is different. The layers of modification A are stacked on top of each other such that π–π-stacking interactions are observable. In contrast modification B does not give rise to π–π-stacking interactions. This is due to the π–π-stacking distance between adjacent layers, which is for modification B larger and was confirmed via 2D ^{1}H/^{1}H correlations. Another important difference between both modifications is that, modification A is more crystalline than modification B. It is not possible to convert the amorphous modification into a crystalline one by annealing. It is only possible to decrease the amorphous amount slightly, which is in agreement with the literature.[96] Combined with theoretical calculation two possible packing models for modification A are suggested. The model, where the packing between the layers is not in an alternate way of the thiophene rings but that the thiophene sulfur of one layer points in same direction as compared to the sulfur in the adjacent layer is slightly preferred. For the bulk as a whole this suggests that the crystalline modification is incorporated in an amorphous matrix. Comparing WAXS results and solid-state NMR data, the crystalline modification A described in this section can be related to modification I assigned by WAXS. This conclusion is underlined by fact that modification I is described as the more common modification, which is present after annealing. These characteristics have been also found via solid-state NMR. Additionally, the ^{13}C chemical shift values assigned for modification I in the literature are in agreement with the values assigned to modification A in this section.[86] A second crystalline modification described in the literature could not be observed in any of the investigated polymers.

5.4. Aggregation and Packing of P3OctiT

For understanding the influence of the side chains towards the packing further, another system with a slight variation within the alkyl side chain is studied. Due to the fact that the alkyl side chain of P3OctiT includes a triple bond which is directly attached to the thiophene backbone (compare Figure 5.3) the dihedral angle is decreased from 30° for P3ATs towards 1°.[97] The influence of the changed dihedral angle with respect to the structure is investigated via solid-state NMR, starting with ^{1}H MAS- and ^{13}C $\{^{1}H\}$ CP/MAS NMR shown in Figure 5.14.

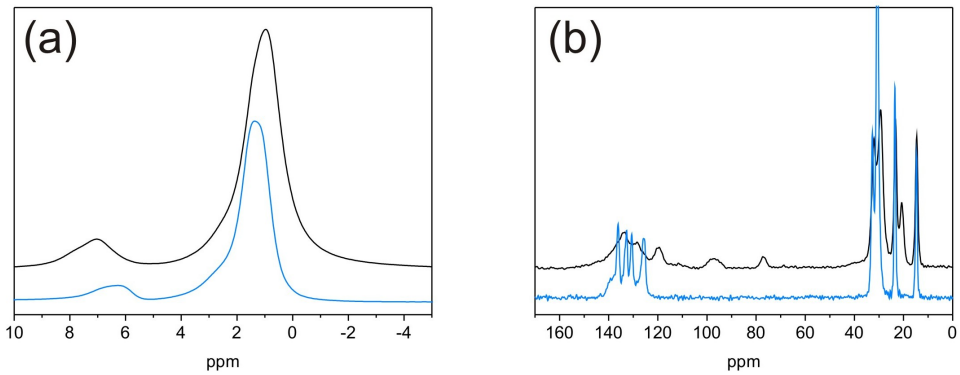

Figure 5.14.: (a) ^{1}H MAS NMR and (b) ^{13}C $\{^{1}H\}$ CP/MAS NMR spectrum of P3HT (blue) and P3OctiT (black).

In the proton spectrum two main peaks are observable at 7.0 ppm (thiophene proton) and 1.0 ppm (alkyl protons) and an additional shoulder at 7.8 ppm. The chemical shift value of 7.0 ppm for the thiophene proton indicates the absence of π–π-stacking interactions. This could be either due to an increased π–π-stacking distance or the stacking of the layers has changed such that the influence of the aromatic moiety is weaker. A comparison of the alkyl resonances of P3HT and P3OctiT show that the line width has increased, indicating a decrease of the local order for P3OctiT. This could be confirmed via ^{13}C $\{^{1}H\}$ CP/MAS NMR shown in Figure 5.14 (b). In the aromatic region of 120–140 ppm the resolution has dropped dramatically. Almost no thiophene related resonances are resolved anymore and also the resonances of the ethynylene unit at 97.5 ppm and 77.5 ppm are rather broad. In the literature it is described that the local order can be improved via annealing and hence, the sample has been heated up to 150°C for one hour.[98] The carbon spectrum after annealing (not shown here) is identical with the spectrum before annealing and no improvement of the local order

could be detected. However also in the literature a ^{13}C $\{^1H\}$ CP/MAS NMR spectrum with a better resolution for P3OctiT is published, but could not verified here.[97]

Additional insights into the local packing could be gained via a ^1H–^1H DQ–SQ correlation shown in Figure 5.15.

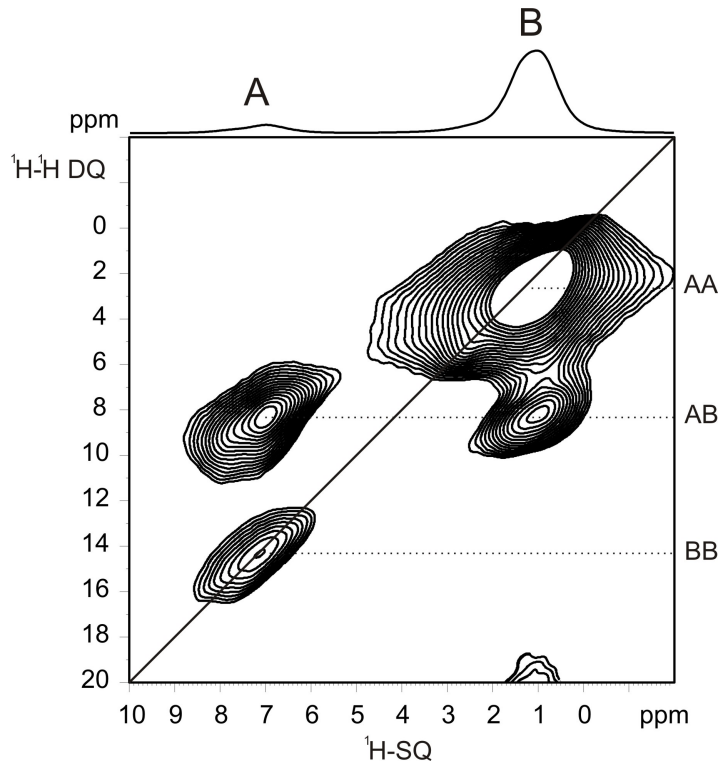

Figure 5.15.: ^1H–^1H DQ–SQ correlation of P3OctiT performed at 25 kHz MAS and one τ_R recoupling. Note the difference to Figure 5.10.

Especially the question whether the π–π-stacking distance has changed or if the local packing is not suitable for π–π-stacking interactions should be clarified. In the proton projection similar to the 1D proton spectrum two peaks are observable at 7.0 ppm and 1.0 ppm. Within the 2D correlation two auto peaks (AA and BB) and one cross peak (AB) occur. AA and AB can be assigned to intramolecular proximities however, the strong resonance AA is related to an intermolecular proximity of thiophene protons. Like for P3ATs, the distance between two thiophene protons within the layer is to far for observing such a strong auto peak. Hence this peak can be assigned to close thiophene proton proximities between different layers, which excludes that no π–π-stacking interactions are observable due to the fact that the π–π-stacking distance is to large. This indicates that the packing has changed, such that the thiophene rings

are not stacked on top of each other, like e.g. P3ATs (shown in Figure 5.11) but with a shift of the layers with respect to each other.

Another important aspect is, how the local mobility has changed for P3OctiT. Hence a REPT-HDOR measurement has been performed to extract the CH-dipolar coupling constant. For one resonance within the broad aromatic region the typical line shape could be extracted and the fitting procedure has been performed. The corresponding dipolar sideband pattern is shown in Figure 5.16.

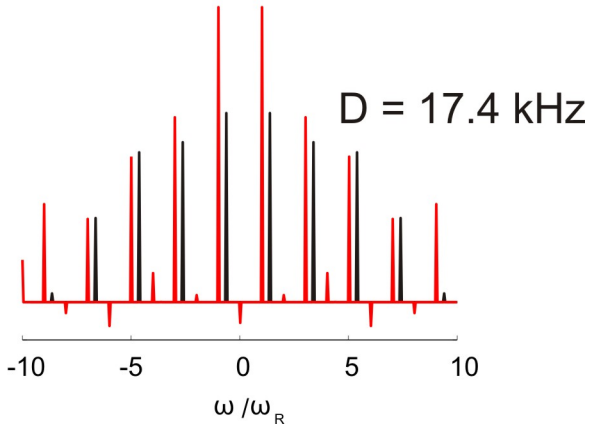

Figure 5.16.: REPT-HDOR sideband pattern of P3OctiT for the slide at 128.8 ppm, at 25 kHz MAS and 4 τ_R recoupling.

By means of fitting a dipolar coupling constant of 17.4 kHz could be extracted. This indicates that the system is still rather rigid, but compared to the P3AT systems the mobility has increased. This is in accordance with the previous results were the mobility is increasing with decreasing local order.

For concluding the present results for P3OctiT it can be noticed that although it has been expected that the local order of such a system should be increased due to the extended planarity, the local order has decreased dramatically. Also, the local packing has changed and no π–π-stacking interactions are observable anymore. This indicates that the different layers are not stacked on top of each other but slightly shifted so that the thiophene proton is located off the aromatic moiety of the next layers. In addition the local mobility within the system has increased. In comparison to the results of the macrocycle and the previous studies of P3ATs it seems that unbranched alkyl chains are most suitable for stabilizing a highly ordered local structure.

5.5. Aggregation of Bulk-Heterojunctions Based on P3HT and PCBM

For later applications in a photovoltaic cell, the morphology of the conjugated polymer alone is not of interest. Since the photovoltaic cell is only functional if the conjugated polymer is combined with an acceptor component like PCBM. Hence, the bulk heterojunction of P3HT and PCBM is studied in more detail in this section. To obtain a thick film and hence enough material for the solid-state NMR studies the corresponding film is prepared under an argon atmosphere by drop coating. For the drop coating procedure a solution containing 3% P3HT/PCBM in chlorobenzene is used. Subsequently, the film was scratched off the glass plate and measured like a powdered sample. Two different ratios of P3HT-PCBM (1:1 and a 1:3) were studied with the main focus on the 1:1 ratio.

As in the previous section a ^{1}H MAS NMR spectrum is a useful starting point to study the P3HT-PCBM mixture (cf. Figure 5.17). In addition to the spectrum of the P3HT-PCBM, also neat P3HT (blue) is shown to highlight possible changes.

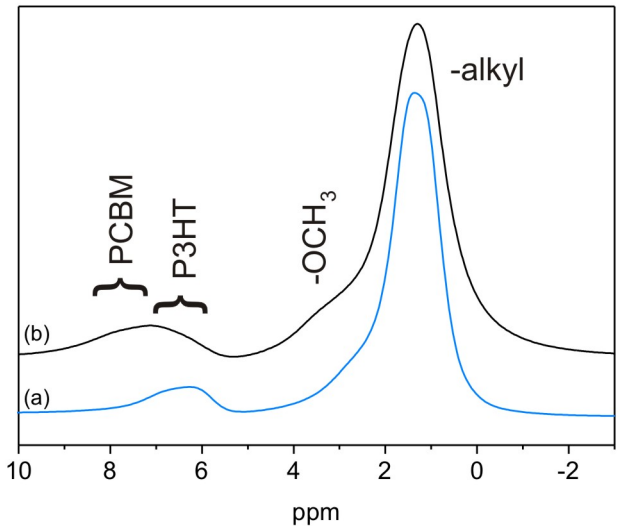

Figure 5.17.: ^{1}H MAS NMR spectra of (a) P3HT and (b) P3HT-PCBM (1:1).

The ^{1}H MAS NMR spectrum of the mixture contains two main peaks that were already observable for P3HT. However, the chemical shift value of the aromatic protons is different for the mixture, it is shifted down field to 7.1 ppm. The alkyl resonance

at 1.3 ppm remains almost unchanged, but the line width has broadened indicating a decreased local order of the mixture compared to pure P3HT. A broadening of the aromatic resonance is observable as well, but this could be due to overlapping resonances of aromatic protons from the polymer and PCBM. In addition, there is a shoulder at about 3.3 ppm, which can be assigned to the OCH_3 group of PCBM.

Additional information are available via ^{13}C $\{^1H\}$ CP/MAS NMR, which is even more sensitive to changes of the local order. The corresponding spectra of P3HT and P3HT-PCBM are shown in Figure 5.18.

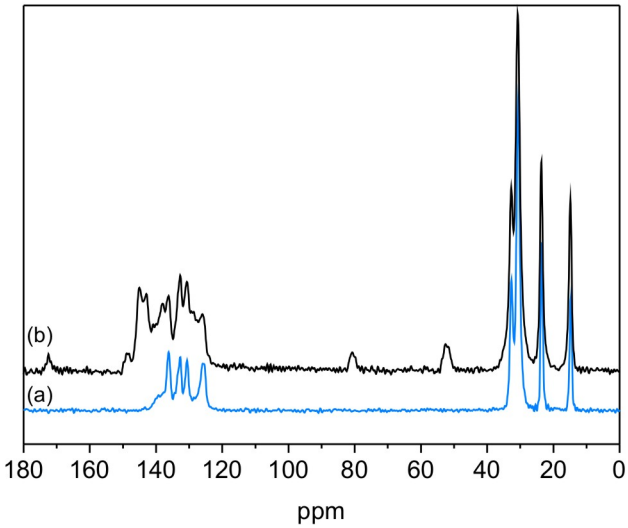

Figure 5.18.: ^{13}C $\{^1H\}$ CP/MAS NMR spectra of (a) P3HT and (b) P3HT-PCBM (1:1).

The ^{13}C $\{^1H\}$ CP/MAS spectrum of P3HT is shown in blue, the spectrum of the mixture is shown in black. Comparing both spectra, there are only minor differences of the alkyl resonances in the region from 35 to 15 ppm. The mixture shows three additional peaks at 172.4 ppm, 80.8 ppm, and 52.2 ppm which can be assigned to PCBM. Major changes are also observable in the aromatic region. Between 150 ppm and 125 ppm, hardly any peaks are resolved. The resonances of P3HT and the aromatic resonances of PCBM are not distinguishable. In agreement with the ^1H MAS NMR spectra, the local order within the mixture is lower than in the neat polymer.

From the literature it is known that the film morphology can be improved via annealing. The question arises, if both components, i.e. PCBM and P3HT, start to crystallize. There are some clear hints that P3HT crystallizes upon annealing which could be

shown via, e.g., X-ray diffraction (XRD) measurements.[96,99,100] In one particular case the crystallization of the P3HT was suppressed in a P3HT-PCBM mixture of 1:2. Upon a ratio of 1:4 no crystallization was found.[100] For PCBM the opinions about the crystallization behavior are even more diffuse. After annealing the XRD pattern shows no reflection, which can be assigned to PCBM. Hence, it was concluded that PCBM is not crystalline in the mixture.[96] In contrast via TEM and optical microscopy, PCBM crystals could be detected in a mixture of PCBM to P3HT at a critical ratio of 1:1. Below that limit, no crystallization was found.[100,101] It is hard to distinguish between the donor and acceptor domains in the TEM images and the results have to be interpreted carefully.[99] All mentioned publications agree that phase separation occurs upon annealing. In the phase separated sample cluster formation can be observed due to the diffusion of PCBM. Around each cluster depleted regions with rather low PCBM contents were found.[100,101]

The question of a possible crystallization within the film is highly important for the efficiency of the corresponding device. Therefore one focus of the solid-state NMR studies is concerned with this question. The P3HT-PCBM mixture was annealed for one hour at 150°C, which is known to be the most efficient annealing temperature.[99] Afterwards a ^{13}C $\{^{1}H\}$ CP/MAS spectrum was measured (cf. Figure 5.19).

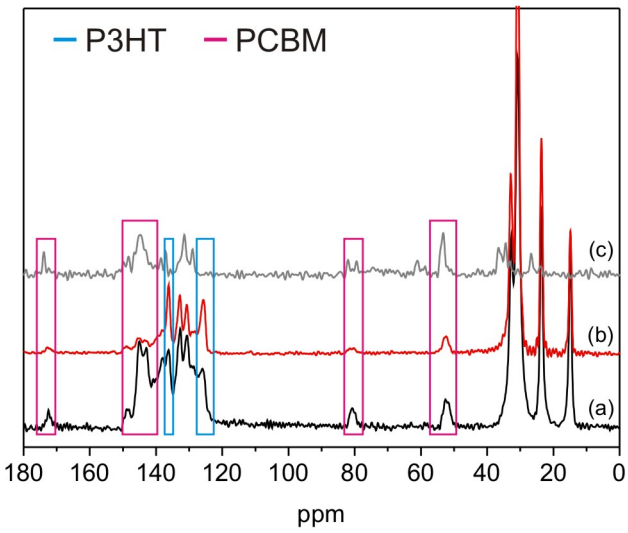

Figure 5.19.: ^{13}C $\{^{1}H\}$ CP/MAS NMR spectra of (a) P3HT-PCBM (1:1) before annealing, (b) P3HT-PCBM (1:1) after annealing, and (c) PCBM for comparison and signal assignment.

The black ^{13}C $\{^1H\}$ CP/MAS NMR spectrum at the bottom (Figure 5.19 a) corresponds to unannealed P3HT-PCBM, the red spectrum shows the sample after annealing ((b), and for comparison in (c) the neat PCBM is shown. The resonances assigned to P3HT are marked with a blue box, PCBM related resonance are highlighted with a magenta box. The spectra before and after annealing indeed confirm that annealing plays a decisive role on the morphology of the mixture. The signal intensities of the resonances within the mixture, which can be assigned to PCBM are dramatically decreased. After annealing the aromatic resonances at 136.1, 132.8, 130.7, and 125.8 ppm of P3HT are clearly observable in contrast to the unannealed sample. The chemical shift positions of the P3HT resonances within the mixture are similar compared to the chemical shift values found for neat P3HT (cf. Figure 5.6). This is a first hint for phase separated regions in the bulk heterojunction mixture. Further, the decrease of the PCBM signal intensity corroborates the interpretation of a phase separation. Before annealing, both components are molecularly dissolved and polarization can be transferred from the proton rich P3HT to the proton poor PCBM. After phase separation, the signal intensity of PCBM decreases dramatically due to the low proton density of PCBM.

Additional insights in the morphology of the bulk heterojunction can be gained from a 2D $^{13}C/^1H$ correlation spectrum, which is shown in Figure 5.20.

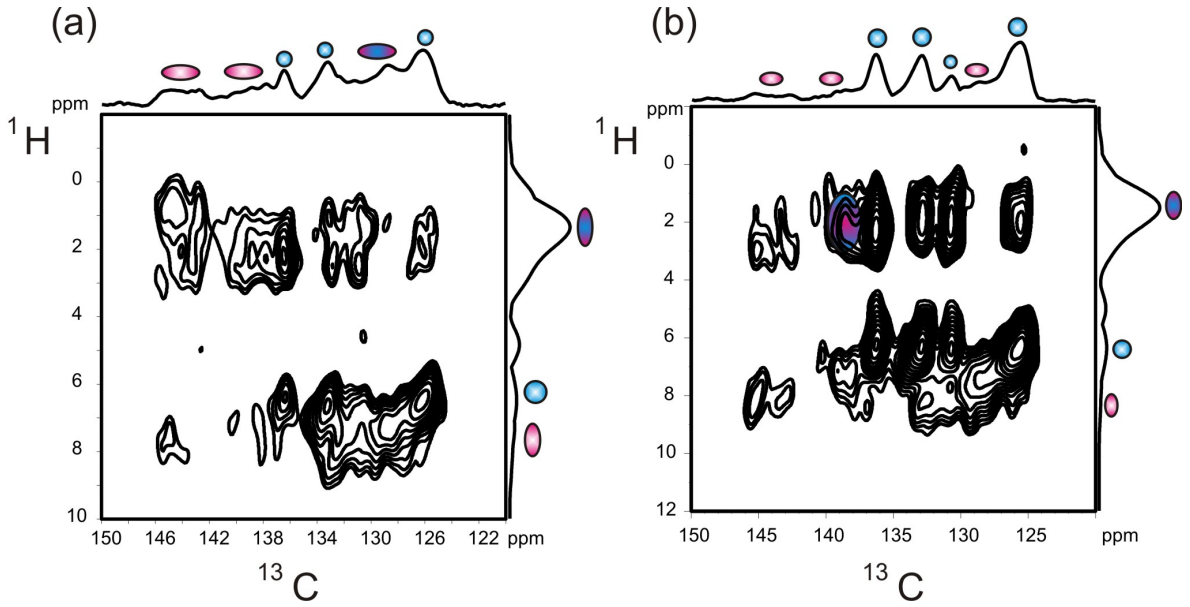

Figure 5.20.: 2D $^{13}C/^1H$ FSLG-decoupled CP HETCOR of P3HT-PCBM (a) before annealing and (b) after annealing recorded at 15 kHz MAS and a contact time of 3 ms.

The direct dimension of the $^{13}C/^{1}H$ FSLG-decoupled CP HETCOR spectra of (a) P3HT-PCBM before annealing and (b) after annealing contain the aromatic region of the ^{13}C spectrum. In the indirect dimension, the ^{1}H chemical shift is observable. Almost all resonances can be assigned to either PCBM (magenta dot) or P3HT (blue dot). Resonances with overlapping P3HT and PCBM chemical shifts are marked with a blue/magenta mixed dot. A comparison of both 2D spectra confirms that annealing causes phase separation. Before annealing all correlation peaks are rather broad and a clear assignment of the correlation peaks of either P3HT or PCBM is not possible. After annealing the intramolecular correlation peaks of P3HT can be easily extracted. They equal the correlations found for the pure polymer in Figure 5.7. In addition, it is possible to gain information about the crystallinity of both compounds. Before annealing neither the P3HT nor the PCBM domains are crystalline. After annealing, the crystalline modification I is found for P3HT (cf. section 5.3). This conclusion is drawn from the similarity of the ^{13}C chemical shift values and the 2D spectra (cf. Figure 5.6). The amorphous phase of P3HT in the bulk heterojunction can neither be retried nor quantified with the ^{1}H MAS NMR as well as in the ^{13}C $\{^{1}H\}$ CP/MAS NMR since the corresponding resonances overlap with the PCBM resonances. The solid-state NMR spectra indicate that the PCBM domains are rather amorphous. Even after annealing, all correlation peaks assigned to intramolecular contacts of PCBM are broad and ill defined. Further information can be drawn from a comparison of the ^{13}C resonances of the neat PCBM and the PCBM in the mixture in the ^{13}C $\{^{1}H\}$ CP/MAS NMR spectrum (Figure 5.19). Two resonances are rather meaningful: the resonance at 172.4 ppm is broadened in the mixture compared to the pure PCBM and the resonance at 80.8 ppm is split into two peaks for neat PCBM, while only one broad peak is observable in the mixture. Both observations indicate that PCBM in the mixture is amorphous, which is in agreement with XRD results found in the literature.[96]

The assignment of intermolecular proximities in the 2D correlation to understand the aggregation within the bulk heterojunction is rather difficult, due to poorly resolved resonances of PCBM and partially overlapping proton resonances. However, one correlation peak (see highlighted region in Figure 5.20 (b)) can be assigned to an intermolecular contact of P3HT and PCBM. The resonance at about 140 ppm, originates from the fullerene ball of PCBM correlates to the resonance of the alkyl protons of P3HT, which helps to get a rough idea of the corresponding packing. Similar 2D correlation studies are reported in the literature. In contrast to the performed solid-state NMR measurements of this work the contact was absent after annealing but present

before annealing.[88]

The observation that the crystal modification I of P3HT is maintained in the bulk heterojunction is supported by ^{1}H–^{1}H DQ–SQ MAS NMR. The corresponding spectrum is shown in Figure 5.21.

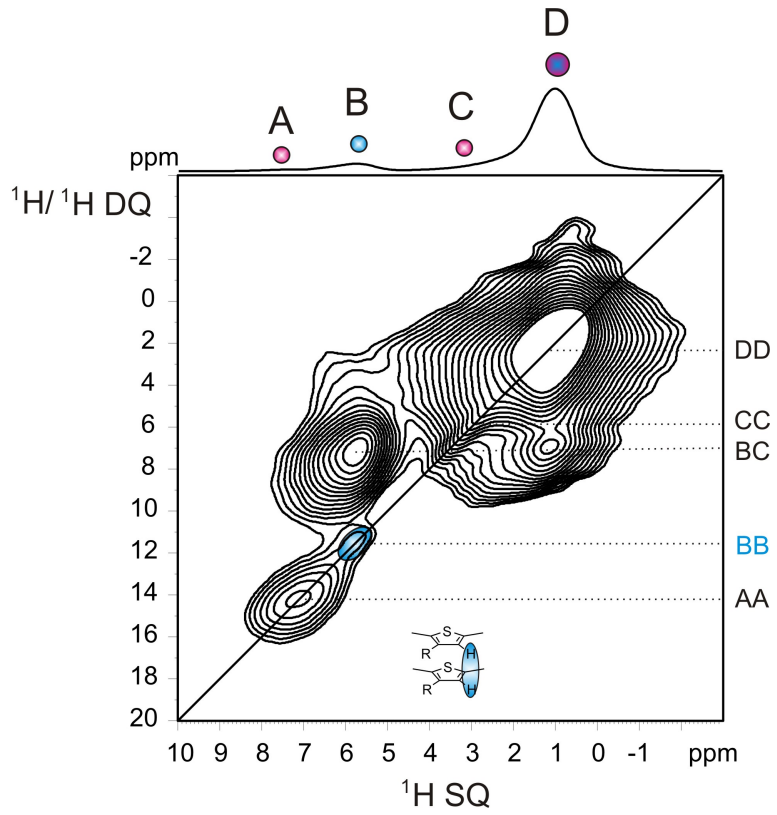

Figure 5.21.: ^{1}H–^{1}H DQ–SQ MAS NMR of P3HT-PCBM recorded at 25 kHz MAS and 1 τ_R recoupling.

The direct dimension of the 2D correlation spectrum of P3HT-PCBM contains four resonances at 7.1, 5.7, 3.1, and 0.9 ppm. The assignment is identical to that of the ^{1}H MAS NMR spectrum shown in Figure 5.17. Due to the improved resolution of the 2D spectrum, the broad aromatic peak is resolved into two peaks which can be assigned to PCBM (7.1 ppm) and P3HT (5.7 ppm). The most important correlation peak is BB, which shows that the intermolecular proximity of the P3HT thiophene protons is maintained and equal to the neat polymer (see Figure 5.10). Hence, the polymer morphology in the mixture after annealing is the same as the morphology found for the neat P3HT. All other observable correlations in the 2D spectrum are due to intramolecular contacts.

To study the effect of the PCBM/P3HT ratio a film with a 1:3 composition was analyzed. The study is focused on the question, if a higher amount of PCBM inhibits the crystallization of the P3HT as claimed in the literature.[100] A first rough idea can be gained from the ^{1}H MAS NMR spectra shown in Figure 5.22.

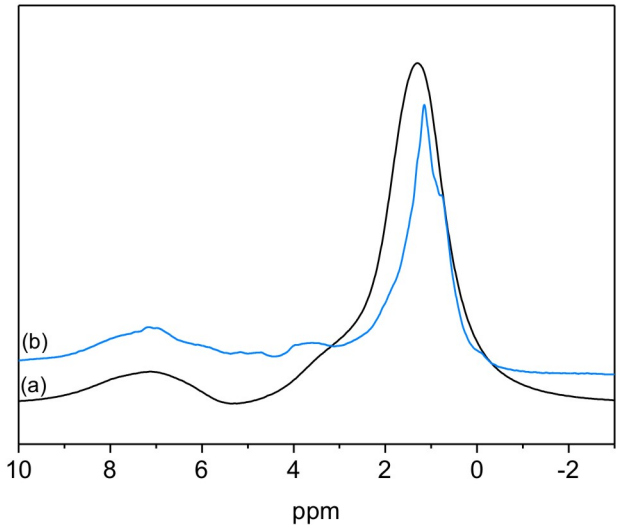

Figure 5.22.: ^{1}H MAS NMR spectra of (a) P3HT-PCBM (1:1) and (b) P3HT-PCBM (1:3). Both spectra were measured after annealing.

The spectrum of the 1:1 mixture is displayed in black. The spectrum in blue corresponds to a 1:3 mixture. For the latter three peaks at about 7 ppm (aromatic protons), 3.9 ppm (OCH_3-group) and about 1 ppm (alkyl protons) are observable similar to the black spectrum. In comparison, the spectral line width of the 1:3 mixture is decreased dramatically. This can be either due to an increase of the local mobility or an increase of the local order. To deepen the understanding of the polymer ratio and its effect on the morphology, ^{13}C $\{^{1}$H$\}$ CP/MAS NMR spectra were recorded (cf. Figure 5.23).

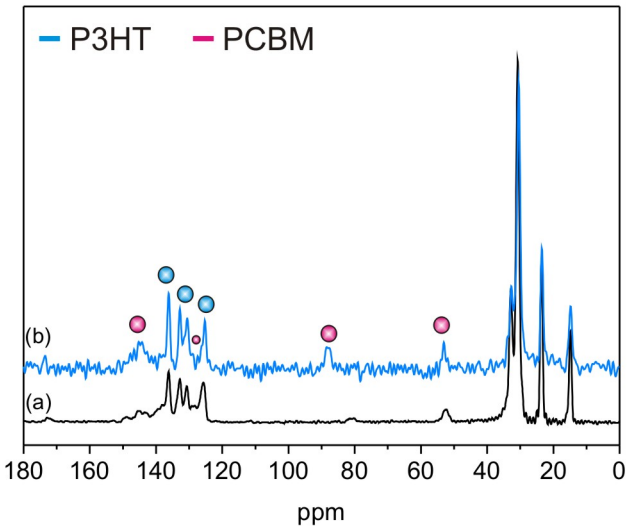

Figure 5.23.: ^{13}C $\{^{1}H\}$ CP/MAS NMR spectra of (a) P3HT-PCBM (1:1) and (b) P3HT-PCBM (1:3). Both spectra were measured after annealing.

The ^{13}C $\{^{1}H\}$ CP/MAS NMR spectra were recorded after annealing since it is only possible to extract information from the spectrum after thermal treatment. The black spectrum on the bottom again corresponds to the P3HT-PCBM mixture with a 1:1 ratio and the blue spectrum above to the mixture with a 1:3 ratio. Both spectra exhibit major similarities. After annealing, all PCBM resonances are decreased dramatically, despite the fact that the ratio of the PCBM was increased by a factor of three. This corroborates the conclusion that annealing leads to a phase separation independent of the P3HT/PCBM ratio. Similar to the spectrum of the 1:1 mixture four resonances assigned to the crystal modification I of P3HT can clearly be observed in the spectrum at 136.1, 132.7, 130.5, and 125.3 ppm. Hence, it cannot be confirmed that a higher PCBM ratio inhibits the crystallization of P3HT.

In conclusion the local order of P3HT-PCBM decreases dramatically compared to both neat components. The system is rather sensitive to thermal treatment and annealing lead to a phase separation of the blend. In the phase separated P3HT domains, crystal modification I is found like in the bulk polymer. In contrast, the PCBM domains are rather amorphous and ill defined. This behavior appears to be rather independent of the P3HT/PCBM ratio.

5.6. Aggregation of PCPDTBT

The second system studied in more detail is based on PCPDTBT (see Figure 5.3). This polymer has gained more and more attention during the past decade due to its promising properties like a suitable band gap. Previous studies of its structure and morphology are rare especially compared to the well-studied P3HT. One reason for the lack of information is due to its decreased local order (as shown by WAXS), which limits the extraction of information.[82,83] In the following section, it will be tried to gain more information via solid-state NMR investigations, starting with ^{1}H MAS NMR shown in Figure 5.24 (a) and ^{13}C $\{^{1}$H$\}$ CP/MAS NMR shown in Figure 5.24 (b).

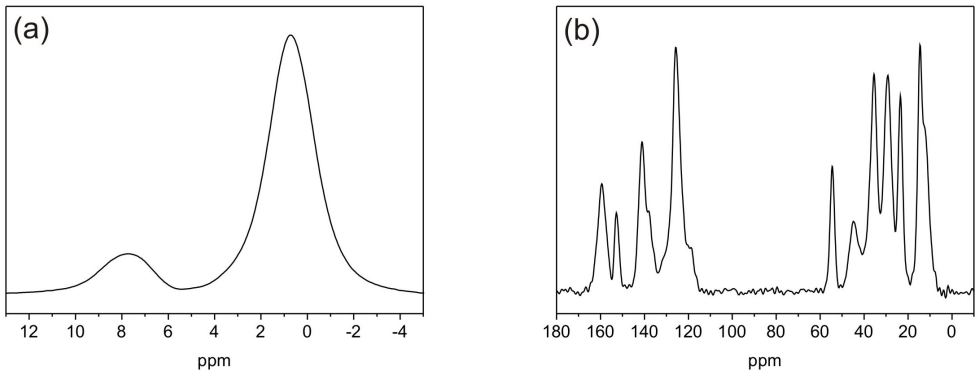

Figure 5.24.: (a) ^{1}H MAS NMR and (b) ^{13}C $\{^{1}$H$\}$ CP/MAS NMR spectrum of PCPDTBT performed at 25 kHz MAS

In the ^{1}H MAS NMR spectrum of PCPDTBT, only two broad peaks at 8 ppm and 1 ppm are resolved. Since the resolution of the resonances is rather low the aromatic resonance cannot be assigned to either the electron-rich cyclopentadithiophen unit or the electron-deficient benzodithiazol. Likewise, the lack of resolution prevented the extraction of the same information from the ^{13}C $\{^{1}$H$\}$ CP/MAS NMR (cf. Figure 5.24 (b)). An explanation for the low local order could be that the branching of the alkyl side chains is not suitable for stabilizing an ordered structure, which has already been observed for the macrocycles. Hence, these solid-state NMR spectra support the WAXS results, that the local order of the polymer is rather low. It should be noted that parameters like the molecular weight and the polydispersity can influence the local order.[102] However, these aspects are not discussed in more detail. Nevertheless, these spectra could be used to understand possible changes of the structure within the bulk heterojunction with PCBM, which is studied in the following section.

5.7. Aggregation of a Bulk-Heterojunction Based on PCPDTBT and PCBM

As for P3HT, the neat polymer is only of minor interest. Hence this study is focused on the bulk heterojunction with PCBM. The sample preparation of the PCPDTBT-PCBM (1:3) blend, which is studied in more detail in this section is described in the literature.[103] Both components were dissolved in dichlorobenzene. After evaporation of the solvent the solid material was scratched of the flask and filled into the NMR rotor. The whole procedure was done under a argon atmosphere. Similar to all studies of this chapter, a ^{1}H MAS NMR spectrum was recorded at first.

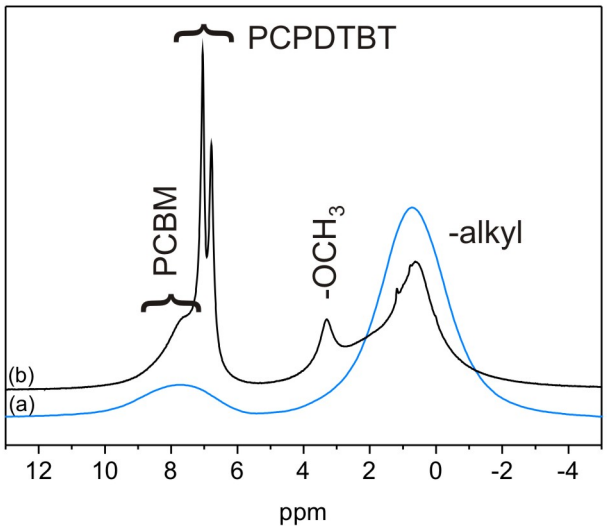

Figure 5.25.: ^{1}H MAS NMR spectra of (a) neat PCPDTBT (for comparison) and (b) of the PCPDTBT-PCBM blend.

The corresponding spectrum of PCPDTBT-PCBM (black) contains five peaks, which are partially well-resolved. Thus, already at first view a significant difference compared to the neat PCPDTBT (blue) is observable. Two resonances at 3.3 and 0.6 ppm can be assigned to the OCH_3 group of PCBM and to alkyl protons, respectively. The spectra substantially differ in the aromatic region where two sharp resonances at 6.8 ppm and 7.0 ppm can be discerned for the blend. The sharpness of these resonances indicates the presence of a highly mobile species in the sample. Due to the chemical shift values of these mobile resonances they most likely originate from the PCPDTBT polymer

within the blend. This is only a rough assumption, since the ill-resolved resonances of the neat spectrum have to be used for comparison. Moreover, one broad resonance is observable at 7.6 ppm, which is assigned to the aromatic protons of the PCBM. Without any annealing steps, the PCBM domains appear rather amorphous and the PCPDTBT domains highly mobile on the molecular level. To verify these assumptions, ^{13}C $\{^{1}H\}$ CP/MAS NMR was performed (cf. Figure 5.26).

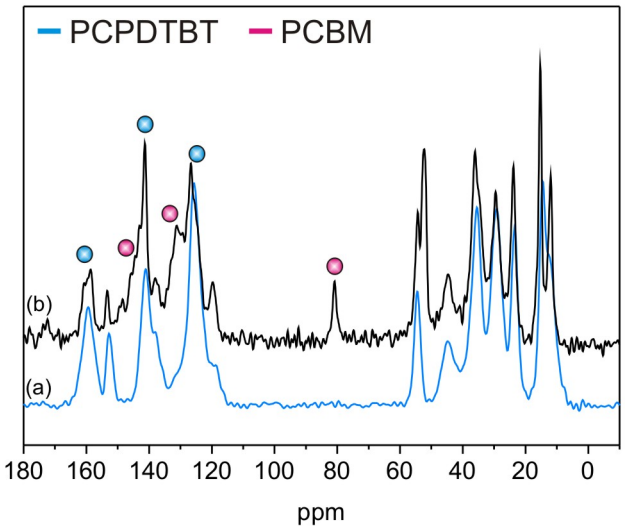

Figure 5.26.: ^{13}C $\{^{1}H\}$ CP/MAS NMR spectra of (a) neat PCPDTBT (for comparison) and (b) of the PCPDTBT-PCBM blend.

Similar to the P3HT-PCBM blend, the resolution of the PCPDTBT-PCBM spectrum is decreases in comparison to the neat polymer. This especially applies to the aromatic region of the spectrum. Some PCPDTBT resonances (e.g. at 141.2 and 126.6 ppm) can be assigned to PCPDTBT domains, which are placed on top of a broad aromatic background. This broad background is probably related to PCBM and is indicative of its amorphous structure in the blend. The resonances originating from the PCPDTBT polymer are sharper than the resonances of the neat polymer. This corroborates the assumption that the polymer is rather mobile in the blend and could relate to an incomplete aggregation of the polymer in the freshly prepared mixture without any annealing step.

All further studies of the polymers were done after annealing. However, this particular sample was stored for two months at room temperature. Without any annealing,

complex changes of the structure could be observed. It is expected that these structural changes could also be induced via annealing but on a shorter time scale (several hours). A first rough idea of these changes can be gained by the ^{1}H MAS NMR spectrum shown in Figure 5.27. The spectrum of the raw blend is shown in black and the spectrum of the aged material is shown in red.

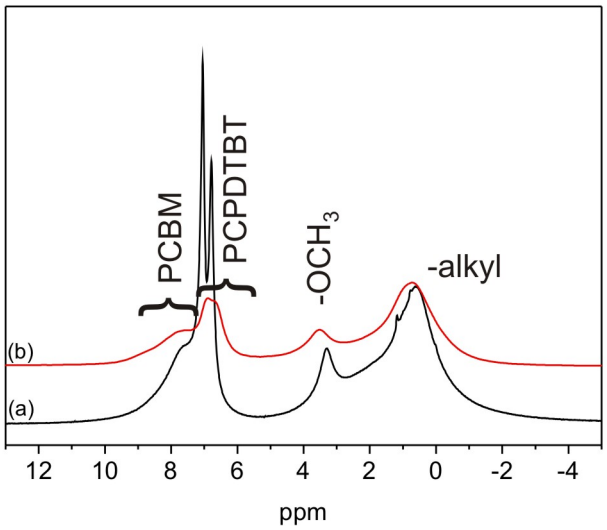

Figure 5.27.: ^{1}H MAS NMR spectrum of (a) raw PCPDTBT-PCBM right after sample preparation and (b) of the same material after two month storage.

The mobile resonances at 6.8 and 7.0 ppm of the aged material underwent considerable changes. Both resonances are much broader, which indicates a dramatic decrease of the local mobility. Additionally, the line width of all other resonances is broadened, indicating that the whole system is less mobile and probably better organized. This assumption can easily be verified via ^{13}C $\{^{1}$H$\}$ CP/MAS NMR (cf. Figure 5.28).

In this spectrum major changes are observable as well. Information about the morphology of the PCBM within the blend is available from the resonances at 174 ppm and 80 ppm (marked with a magenta box see Figure 5.28). These resonances can be clearly assigned to PCBM since they do not overlap with any resonance of PCPDTBT. While the resonance at 174 ppm is hardly observable in spectrum (a), a sharp resonance occurs in spectrum (b) which indicate crystalline domains of PCBM. Also, the resonance at about 80 ppm shows a huge change. The broad peak of the fresh prepared blend is splitted in two sharp resonances in spectra (b) and (c).

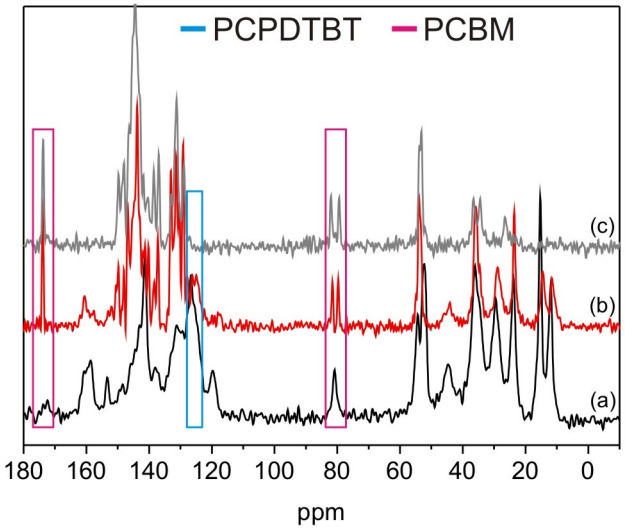

Figure 5.28.: ^{13}C $\{^{1}H\}$ CP/MAS NMR spectra of (a) raw PCPDTBT-PCBM right after sample preparation and (b) two month later. The spectrum of PCBM is displayed in (c) for comparison.

Both observations indicate a crystalline organization of PCBM within the blend as observed in neat PCBM. This is particularly remarkable since the PCBM domains in P3HT-PCBM blends remain amorphous after annealing. This could be due to the fact that PCPDTBT in the blend is not as densely packed as the crystalline P3HT and hence allows for PCBM diffusion. Larger domains of PCBM might improve the crystallization behavior and therefore in the blend with P3HT no PCBM crystallization occurs compared to the blend based on PCPDTBT. It is much harder to extract information about the PCPDTBT morphology within the blend, since the aromatic region includes almost no resonance that can be clearly assigned to PCPDTBT. One resonance, which might be considered, is located at 124.8 ppm (marked with a blue box see Figure 5.28). In spectrum (a) this resonance consists of a broad peak while in (b) it is splitted into two distinct peaks. This indicates that in the blend material the polymer morphology is improved compared to the neat polymer.

Unfortunately, no further information about the phase separation behavior of the freshly prepared and the aged sample can be obtained. For example the signal intensity of PCBM does not decrease in the PCPDTBT-PCBM blend in contrast to the P3HT blend. It is most likely that the crystallization of PCBM also leads to a phase separation.

5.8. Conclusions

In this chapter two relevant systems for photovoltaic applications were studied. Each study was started with a characterization of the neat polymer. The obtained results were then used as a starting point for the characterization of the blend with PCBM. The system based on P3HT is widely used as a model compound to study how different aspects influence the device efficiency. For P3HT, a crystalline- and an amorphous modification were observed. The crystalline modification is of high interest since it is also found in the blend with PCBM after annealing. PCBM is rather amorphous in contrast to P3HT and appears to be unaffected by annealing. Further, it could be shown that the blend phase separates upon annealing. System based on PCPDTBT behaves differently. The bulk polymer has a low local order and no crystalline modification could be detected. The corresponding blend with PCBM exhibits crystallized domains of PCBM after annealing. This also leads to an improvement of the order of the PCPDTBT polymer. Combined with already available information from other methods, the results obtained in this chapter provide for a substantial knowledge about how structure and dynamics of these photovoltaic materials are affected on the local scale. This information is crucial to improve the efficiency of photovoltaic cells further and open a widespread use of these systems in the future.

6. Aggregation of Oligo(p-benzamides) - Poly(ethylene glycol) Copolymers

Application like LEDs and photovoltaic cells impose, demanding requirements on the organic material. As already discussed in section 5.1 a high efficiency of a photovoltaic cell is only provided if the donor and acceptor material are phase separated on the length scale of 10 nm. Within the phase separated domains a high crystallinity is necessary and the donor and acceptor phases need to form a continuous pathway to the electrodes in order to allow an efficient charge transport.[61,104] These strict requirements are difficult to achieve via a phase separation of polymer blend materials. This phase separation originates from a spinodal decomposition during film formation and is rather difficult to control.[58] Also, during operation of the device, macrophase separation can occur, which leads to a dramatic decreases of the performance efficiency.[58,104] One idea to overcome these problems is the application of copolymers with a donor- and an acceptor-block. A conjugated polymer is used as a donor and serve as a rigid backbone. For improving the properties of this block flexible polymer coils are attached and a rod-coil copolymer is formed.[58,61] In advantage over traditional polymer blends, rod–coil copolymers form microphase separated structures with highly ordered and thermodynamicall stable nano-phases. Also, the phase separation can be fine-tuned via the length of the blocks.[104,105] The driving forces for such nanoscaled phase separation are interactions between various segments and geometric effects.[106–109] The phase separation of rod-coil copolymers can be rather complex since besides the minimization of interaction of unlike blocks it is governed by anisotropic interactions and liquid-crystalline behavior. Phase diagrams of model systems show different phases such as isotropic, nematic, and lamellar structures for rod-rich systems whereas strip and puck morphologies dominate for coil-rich system.[61,108–111] Still the understanding of the aggregation behavior of rod-coil copolymers is hampered, especially if additional driving forces such as hydrogen bonding occur. However, hydrogen bonding suppresses macrophase separation in favor of microphase separation, which can be combined with long-range order in the material.[112] Besides the influence of hydrogen bonding on the phase separation it allows to control the nanoscaled ar-

chitectures of such materials. Further, it is possible to switch between nano-phase and macro-phase separation by disturbing hydrogen bonding with the temperature.[113,114] The aim of this chapter is to get a deeper understanding of the aggregation behavior and nano-scaled architecture of rod–coil copolymers based on oligo(p-benzamides) (OPBA) and poly(ethylene glycol) (PEG), including effects of non-covalent interactions with respect to the structure formation. In this chapter, π–π-stacking interactions and hydrogen bonding are in the focus. Secondly, it is assessed how th lengths of rod and coil length influence the structure formation. Due to the hydrogen bonding network, a secondary structure is formed, which reduces the ability of the chains to rearrange. This reduced conformational freedom allows to predict the geometry and hence, simplifies the correlation between molecular shape and superstructure.[115,116]

6.1. Rod–Coil Copolymers Based on OPBA-PEG

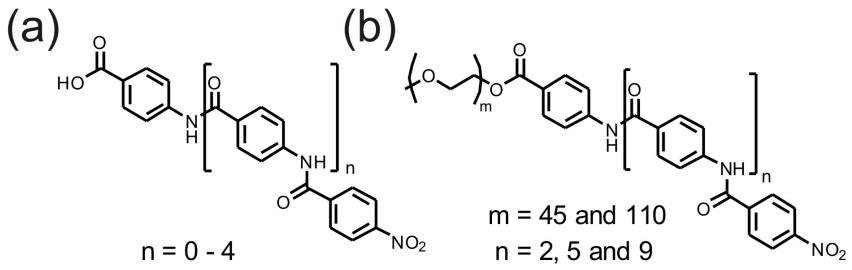

Figure 6.1.: Overview of the investigated (a) unsubstituted OPBAs and (b) OPBA-PEG rod–coil copolymers.

The rod–coil copolymers in this study are based on oligomeric rod blocks of oligo(p-benzamides) (OPBA) and a poly(ethylene glycol) (PEG) coil. Figure 6.1 (a) gives an overview of the investigated unsubstituted, OPBAs with n = 0–4 repeat units, named OPBA-2 to OPBA-6. Figure 6.1 (b) shows the investigated rod–coil copolymers with a varying rod and coil lengths (OPBA-7-PEG110, OPBA-11-PEG110, and OPBA-4-PEG45). Section 6.3 focused on the characterization of unsubstituted OPBAs to get a deeper insight in those materials. This knowledge is then used to understand the structure of the OPBAs incorporated in the rod–coil copolymers. One interesting feature of OPBAs is the aggregation behavior due to their rigidity, resulting mainly from the strong hydrogen-bonding network. This is already known from the related

polymer Kevlar. The latter polymer is, due to the hydrogen bonding network, hardly destructible and hence used in bulletproof vests and protective helmets. However the strong hydrogen bonding network in OPBAs require a rather complex synthesis and advanced analytical characterization due to poor solubility and crystallization behavior. The synthetic route of unsubstituted OPBAs is shown in Figure 6.2.

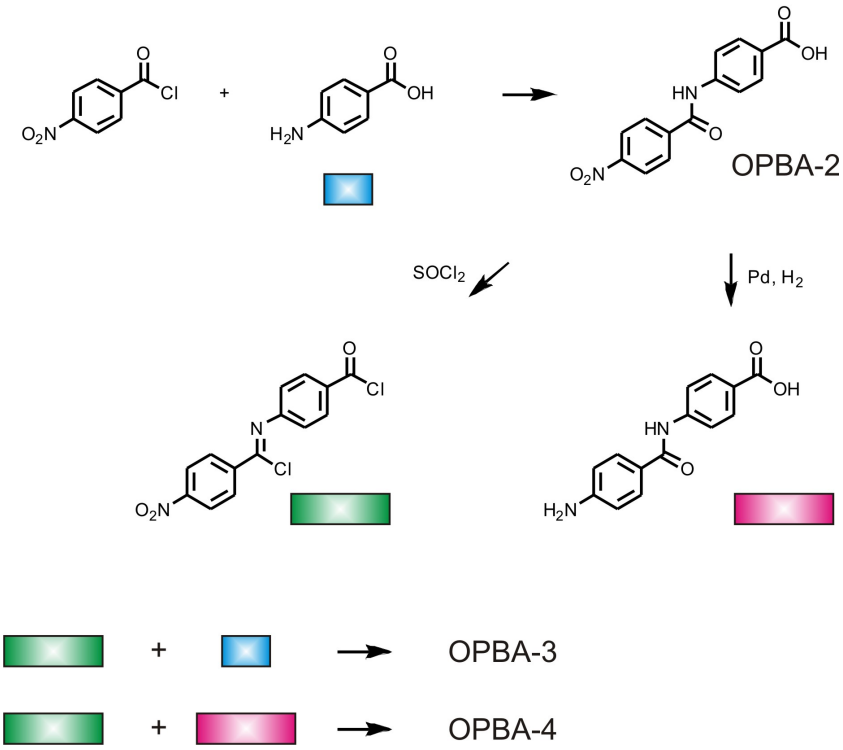

Figure 6.2.: Scheme of the synthetisis for OPBAs.[117]

In the first step of the synthesis, p-nitrobenzoyl chloride and p-aminobenzoic acid are reacted to OPBA-2. The synthesis of longer OPBAs proceed via precursors, which are not able to form hydrogen bonds and, hence, have a better solubility. This is done by the reaction of OPBA-2 with thionyl chlorid forming an imidoyl chloride (compound marked with a green box in Figure 6.2). This imidoyl chloride can then be reacted with another amine to yield a longer OPBA after hydrolysis. Since longer OPBAs can also be converted to imidoyl chlorides unsubstituted OPBAs with up to six repeat units can be synthesized.[117]

The synthesis of the corresponding rod–coil copolymers is similar and shown in Figure 6.3. In the first step p-nitrobenzoyl chloride is connected to the PEG polymer. Afterwards, a similar OPBA build-up procedure is performed as already described

above.[118,119] The PEG coil also increases the solubility so that OPBA rods with up to eleven repeat units within the copolymer are feasible.

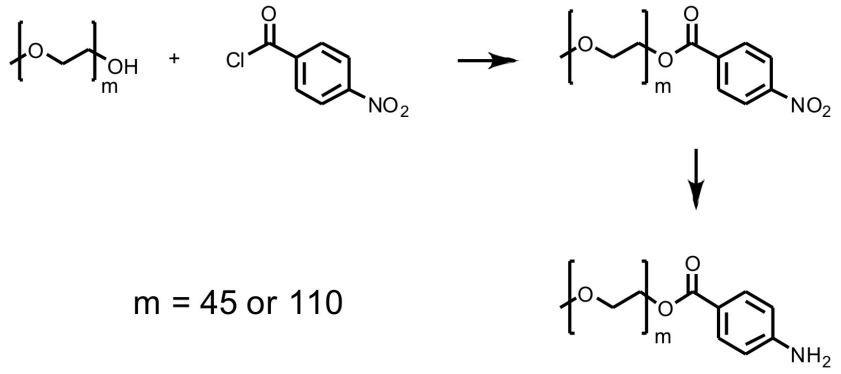

Figure 6.3.: Scheme of the synthetic route for OPBA-PEG.[119]

6.2. Aggregation of OPBA–PEG Copolymers in Solution

The aggregation behavior of OPBA–PEG copolymers in solution was assessed by previous studies.[115,119] Via gel permeation chromatography (GPC) it was found that the aggregation behavior strongly depends on the solvent. In a hydrogen bond breaking solvent, like dimethylformamide (DMF), no aggregation is observed and the copolymer is molecularly dissolved. If the solvent is changed, e.g. to chloroform, aggregation occurs above a critical OPBA rod length. While OPBA-1-PEG110 to OPBA-4-PEG110 are still molecularly dissolved, a rod length of five repeat units leads to aggregation.[119] The aggregation cannot only be controlled by the size of the rod, but also by the size of the coil. For a coil length of 45 repeat units, aggregation is already induced even if the rod consists of only four repeat units.[115] The size of the aggregates is well defined and no intermediate sized aggregates were found via GPC. Further studies of OPBA-7-PEG110 and OPBA-7-PEG45 were conducted with light scattering and scanning force microscopy (SFM). Combining static and dynamic light scattering OPBA-7-PEG110 was found to posse a spherical shape with an ellipsoid character. This result could be confirmed via SFM measurements, which also allowed to measure the dimensions of the aggregates. The size of the aggregates within a layer is 20–35 nm (50–90 units) and the height is about 2 nm (6 units). For OPBA-7-PEG45, a broader distribution of the particle size was found. Also, the ratio between the radius of gyration and the

hydrodynamic radius of about 1.6 indicates an anisotropic shape. The SFM images showed aggregates which are elongated rod-like.[115]

6.3. Aggregation of Unsubstituted OPBAs in the Solid State

So far solely the aggregation behavior of OPBA-PEG copolymers in the solid state was studied via differential scanning calorimetry (DSC). With increasing length of the OPBA rod in the copolymer, the melt enthalpy of the PEG coil decreases. This indicates that the OPBA rod inhibits the crystallization of PEG segments in the vicinity of the OPBA domains.[119] In this chapter the study of the aggregation in the solid state is expanded with solid-state NMR studies starting with the aggregation behavior of unsubstituted OPBA rods. Since the size dependency of this rod block for the structure of the copolymer is of special interest the NMR study was initiated with the size dependency of aggregation on the length of the oligomer. For this kind of investigation, the ^{13}C $\{^1H\}$ CP/MAS experiment is particularly suited since it is sensitive to structural changes and local degrees of organization.

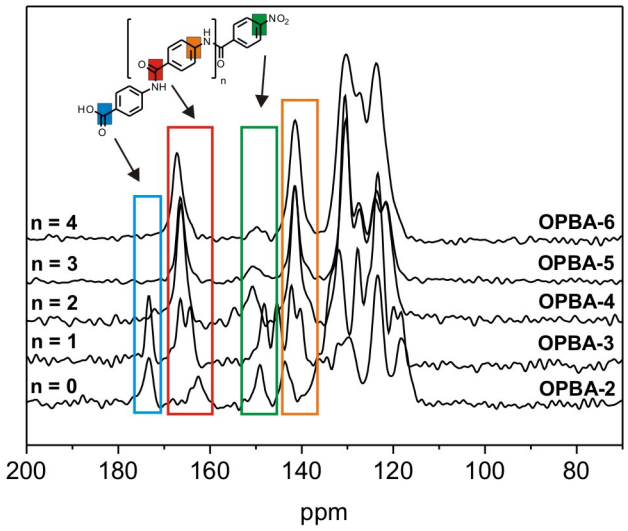

Figure 6.4.: ^{13}C $\{^1H\}$ CP/MAS spectra of OPBAs with different numbers of repeat units, performed at 25 kHz MAS and a CP contact time of 3 ms. The resonance assignment is illustrated by the color code.

The measured spectra of OPBA-2 to -6 are shown in Figure 6.4 and the corresponding

assignment is outlined with a color code. The resonance at 172 ppm is assigned to the COOH group. The CONH carbon has a chemical shift of about 164 ppm and the signals at about 150 ppm and 142 ppm can be assigned to the quaternary carbon atoms bearing nitro and amide groups. The resonances in the region of 120 to 140 ppm can be assigned to aromatic carbon atoms.[120]

In comparison, the spectra of OPBA-2 and -3 differ from those of OPBA-4 to -6. This indicates that the structure for the short OPBAs with n = 0 and 1 is different from that of the longer oligomers. In particular, the well-resolved peak at 172 ppm of the COOH group is only present in OPBA-2 and -3. Remarkably, longer OPBAs with four and more repeat units (n $\geq$ 2) give rise to similar ^{13}C spectra, suggesting an equilibrium structure (see Figure 6.4). The only observable difference for the longer OPBAs is a deteriorating spectral resolution, most likely caused by a decreasing crystallinity of the samples.

The ^{1}H MAS NMR spectra shown in Figure 6.5 reflect a similar behavior. For OPBA-2 and -3, a strong peak at about 14 ppm is observed, which is absent for the longer OPBAs with n $\geq$ 2. The broad peak at about 7 ppm, present for all OPBAs, can be assigned to aromatic protons. The additional resonance at 2 ppm for OPBA-6 is caused by impurities due to the poor solubility, which makes a purification difficult.[117]

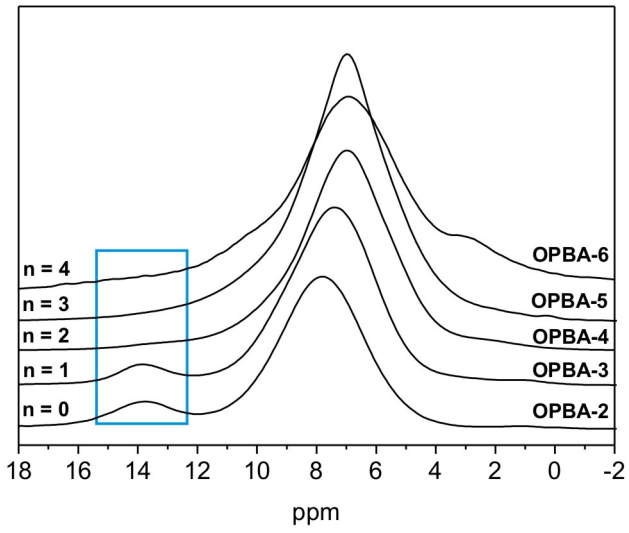

Figure 6.5.: ^{1}H-MAS NMR spectra of OPBA-2 to OPBA-6. The resonance at 14 ppm is only present in OPBA-2 and -3.

In conclusion both ^{1}H MAS NMR and ^{13}C $\{^{1}$H$\}$ CP/MAS spectra indicate a change of

the OPBA structure with respect to the number of repeat units. Above four repeat units, an equilibrium structure is observed. The structure of OPBA-2 and OPBA-3 is discussed in more detail in the following section. Subsequently, the equilibrium structure of the longer OPBAs with (n $\geq$ 2) is assessed which is more important for the aggregation behavior of the copolymers and therefore constitutes the center of this section.

6.3.1. OPBA-2 and OPBA-3

To understand the structural differences between OPBA-2 and -3 and the longer OPBAs the additional peak in the proton spectrum at 14 ppm needs to be assigned. Due to its chemical shift value this resonance is likely to originate from hydrogen bonded protons.[28] There are two possible groups which are able to form hydrogen bonds in the molecule: the CONH groups and the COOH group. A proper assignment can be done via a ^{1}H–^{1}H DQ–SQ MAS NMR spectrum, which is shown for OPBA-2 in Figure 6.6. The correlation spectrum of OPBA-3 is similar and not shown here.

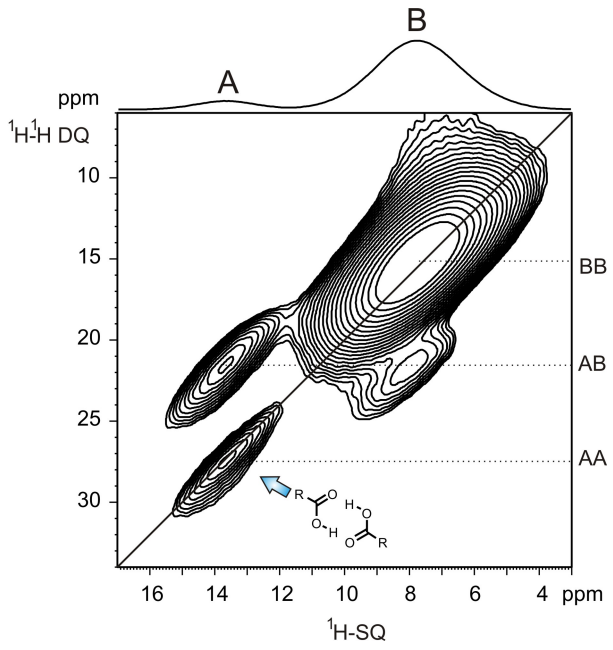

Figure 6.6.: ^{1}H–^{1}H DQ–SQ MAS NMR spectrum recorded at 30 kHz MAS and 1 τ_R recoupling. The auto peak indicates a close proximity between the hydrogen bonded protons which can only be explained by a dimer formation of the COOH groups.

The ^{1}H spectrum in direct dimension contains two peaks. The peak at about 14 ppm is assigned to hydrogen bonded protons (A) and, the peak at 7 ppm is assigned to aromatic protons (B). For each resonance an auto-correlation peak is observable (AA and BB). Further, the spectrum contains cross correlation peaks among the two resonances (AB). The auto peak BB, assigned to proximities among aromatic protons, and the cross peak AB, assigned to proximities of hydrogen bonded protons and aromatic protons can be understood in terms of intramolecular proximities. An interesting correlation is the auto peak AA, which indicates proximities of hydrogen bonded protons. This can only be explained by a dimer formation of two COOH groups (see inset of Figure 6.6). While OPBA-2 and OPBA-3 are able to form hydrogen bonded dimers via two carboxylic acid groups, the longer OPBAs are not. To gain a deeper understanding of the hydrogen bonded network of OPBA-2 and OPBA-3, also the NH groups are of interest. Since their proton resonances are probably hidden under the broad aromatic signal, additional techniques like ^{2}H MAS NMR are necessary.

To measure a ^{2}H MAS NMR spectrum the amount of deuterium has to be increased in the sample. This could be easily achieved by stirring OPBA-2 and -3 for two days in D_2O. Thus, all NH and COOH protons could be exchanged by deuterium. The aromatic protons are not exchangeable and hence, not observable in the ^{2}H MAS NMR spectrum. The measured ^{2}H MAS NMR spectra of OPBA-2 and OPBA-3 are shown in Figure 6.7 (blue). The corresponding proton spectra are shown in black for comparison. Both spectra can be directly compared since the chemical shifts of deuterium and protons are rather similar (within $\pm$0.2 ppm) which is known as the isotope effect.[121]

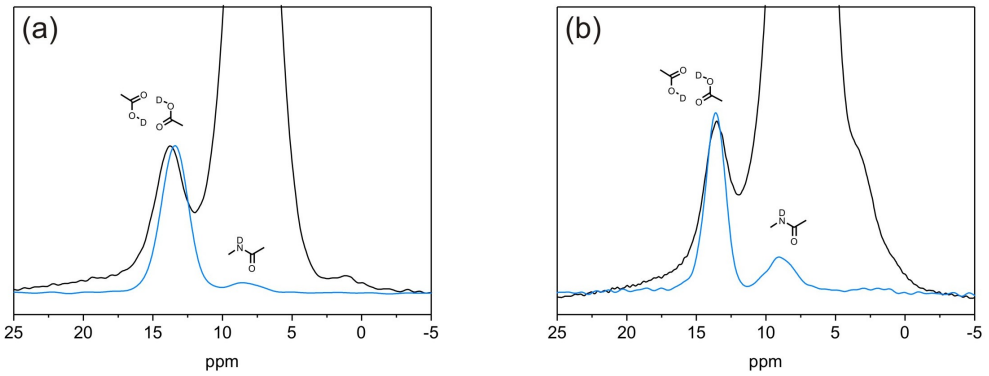

Figure 6.7.: ^{1}H MAS NMR (black)- and ^{2}H MAS NMR (blue) spectra of **(a)** OPBA-2 and **(b)** OPBA-3. In both spectra contain two peaks at about 14 ppm (COOH) and 9 ppm (NH).

In the ^{2}H MAS NMR spectra two resonances are observable for both OPBA-2 and OPBA-3. The resonance at about 14 ppm can be assigned to the COOH protons since the chemical shift agrees with that of the proton spectra. In addition, NH protons can be observed in the ^{2}H MAS NMR spectrum in contrast to the normal ^{1}H MAS NMR spectrum where these are hidden under the broad aromatic signals. The weaker intensity of the NH resonances compared to the COOH resonances might be due to a less quantitative deuterium exchange. The NH resonance of OPBA-2 occurs at 8.4 ppm, the NH resonance for OPBA-3 occurs at 9.0 ppm. This indicates that the NH hydrogen bonds are weaker than the COOH hydrogen bonds and that the NH hydrogen bonds present in OPBA-3 are stronger than those in OPBA-2.[22]

The NH hydrogen bonding network can be further studied via ^{15}N $\{^{1}H\}$ CP/MAS NMR (cf. Figure 6.8).

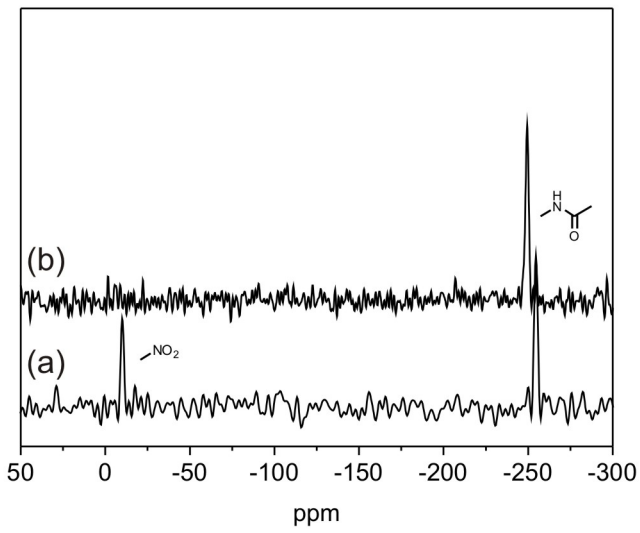

Figure 6.8.: ^{15}N $\{^{1}H\}$ CP/MAS NMR of (a) OPBA-2 and (b) OPBA-3, performed at 5 kHz MAS and a CP contact time of 7 ms.

For OPBA-2, two signals are observable in the ^{15}N spectrum: one signal at –10.1 ppm, which can be assigned to the nitro group and one signal at –254.7 ppm which can be assigned to the NH group. The ^{15}N $\{^{1}H\}$ CP/MAS NMR spectrum of OPBA-3 only contains one signal at –249.5 ppm, which can be assigned to the NH nitrogen. Here no signal stems for the nitro group. This indicates that the nitro-group of OPBA-2 is in closer proximity to protons. Hence, the polarization from the protons towards the

nitrogen is more efficient and a signal can be detected. Also, the difference of ∼5 ppm of the NH chemical shift indicates that the hydrogen bond environment is most likely different in OPBA-2 and -3. The nitrogen chemical shift is very sensitive to such changes due to its broad chemical shift range.[122]

The differences between the ^{15}N $\{^1H\}$ CP/MAS NMR (Figure 6.8) spectra and the ^{13}C $\{^1H\}$ CP/MAS NMR spectra (Figure 6.4) of OPBA-2 and OPBA-3 emphasize the basic structural differences in the hydrogen bonding network and the structure in general. The only similarity of both structures seems to be the dimer formation due to carboxylic acid hydrogen bonds.

A single-crystal X-ray structure would aid the interpretation of the structural features observed by NMR. However, both systems do not crystallize. This problem can be overcome with a special technique based on a combination of electron and X-ray diffraction. This technique allows the extraction of information similar to a single-crystal X-ray study and the results are shown in Figures 6.9 and 6.10.[123]

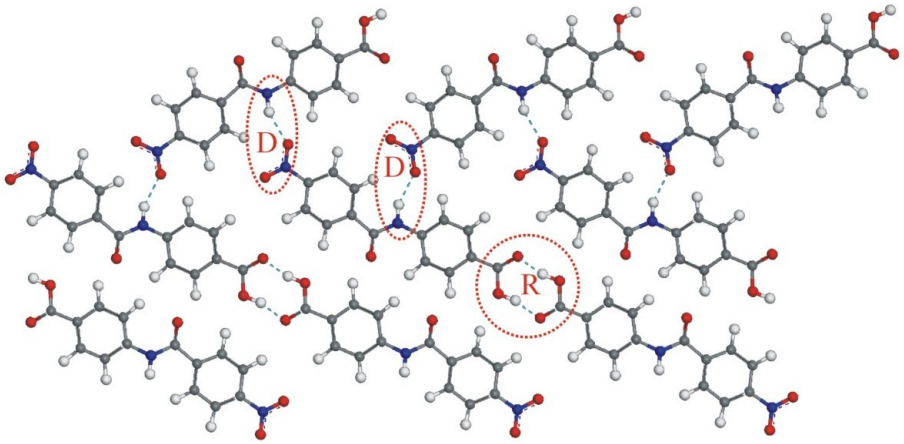

Figure 6.9.: Crystal structure of OPBA-2 obtained by a combination of electron and X-ray diffraction on small crystallites in the sample.[123]

The crystal structure of OPBA-2 confirms the hydrogen bonding and dimer formation if two carboxylic acid groups (marked with R in Figure 6.9). Further, the peak of the nitro group at -10 ppm in the nitrogen spectrum can be explained by hydrogen bonding of the NH group with the oxygen of the nitro group (marked with D in Figure 6.9). In fact, due to that particular hydrogen bonding, polarization can be transferred from the NH proton towards the nitro group and a signal can be observed. All NH-hydrogen bonds are within a layer.

The crystal structure of OPBA-3 is shown in Figure 6.10. OPBA-3, like OPBA-2, shows a dimer formation of two carboxylic acid groups (marked with R in Figure 6.10) in agreement with the ^{1}H MAS NMR results (cf. Figure 6.5). However, the hydrogen bonds of the NH group are peptide-like hydrogen bonds with a CO group of a different OPBA-3 molecule (marked with C in Figure 6.10). Thereby one hydrogen bond is formed within the layer and the other hydrogen bond is formed between the layers.

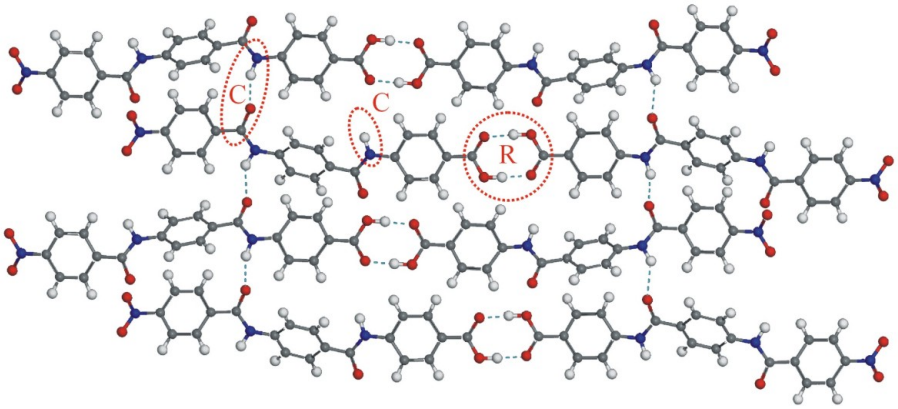

Figure 6.10.: Crystal structure of OPBA-3 obtained by a combination of electron and X-ray diffraction on small crystallites in the sample.[123]

These, variations in the hydrogen bonding network account for the chemical shift difference of the NH nitrogen in the ^{15}N spectrum and for the absence of the NO_2 peak. This completely different hydrogen bonding network leads to substantially different structures as observed by ^{13}C $\{^{1}$H$\}$ CP/MAS NMR (cf. Figure 6.4). Hence the combined information of crystal structure and solid-state NMR leads to a proper understanding of both structure and aggregation of OPBA-2 and OPBA-3.

6.3.2. OPBAs with (n $\geq$ 2)

Since the rod-blocks of the copolymers contain OPBAs with at least five repeat units, the longer OPBAs are the focus of all further studies. The carbon spectra shown in Figure 6.4 indicate an equilibrium structure for OPBAs with n $\geq$ 2. Thus it is sufficient to understand the aggregation of one representative. As an example, OPBA-5 was chosen. One remarkable difference compared to OPBA-2 and OPBA-3 is the absence

of the proton resonance at 14 ppm, which indicates that these longer OPBAs are not able to form hydrogen bonds between carboxylic acid groups. This could also explain the absence of the peak at 172 ppm in the ^{13}C $\{^1H\}$ CP/MAS spectra (see Figure 6.4). Due to the lack of hydrogen bonding the chemical shift of the carboxylic acid carbon atom is shifted towards higher field and thus overlaps with the chemical shift of the CONH peak at 164 ppm.

Obviously, the rod length affects what kind of hydrogen bonding determines the structure. On the one hand, the hydrogen bonding of two carboxylic acid groups is known to be by far stronger than amide hydrogen bonds.[124] On the other hand, the number of amide hydrogen bonds is increasing with increasing rod size, while the formation of the carboxylic dimers is limited to the end groups. For OPBA-2 and -3, the ratio of the two types of hydrogen bonds is 1:1 and 1:2, respectively, and hence, the carboxylic acid dimer formation is facilitated. With an increasing number of repeat units, the number of carboxylic acid hydrogen bonds decreases compared to the number of amide hydrogen bonds. Hence, amide hydrogen bonding dominates the structure formation for longer oligomers ($n \geq 2$), as shown by the absence of the peaks at 14 ppm in the ^1H MAS NMR spectrum (Figure 6.5) and 172 ppm in the ^{13}C $\{^1H\}$ CP/MAS NMR spectrum (Figure 6.4).

Again, to understand the hydrogen bonding network completely a single-crystal X-ray structure would be helpful. However, for OPBAs with $n \geq 2$ neither a single-crystal X-ray structure is available nor the alternative technique by combining electron and X-ray diffraction is feasible. To further reveal the impact of hydrogen bonding on the structure, the influence of a hydrogen bond breaking solvent was probed upon crystallization of OPBA-3 with dimethylformamide (yielding OPBA-3-DMF). DMF blocks the carboxylic acid end groups as revealed by the single-crystal X-ray structure of the co-crystal. Thus, almost no dimer formation is observed as for OPBAs with $n \geq 2$.[115] To understand the impact of this disruption towards the structure, a ^{13}C $\{^1H\}$ CP/MAS NMR spectrum of OPBA-3-DMF was measured and compared to the ^{13}C spectrum of OPBA-5 (cf. Figure 6.11).

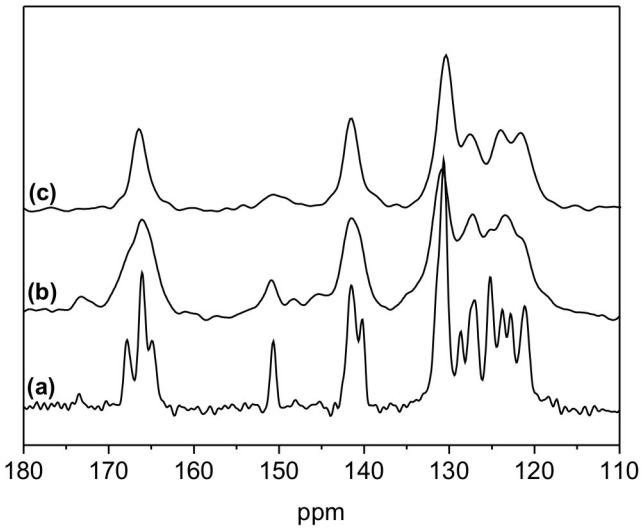

Figure 6.11.: ^{13}C $\{^1$H$\}$ CP/MAS NMR spectrum of (a) OPBA-3-DMF, (b) OPBA-3-DMF processed with an additional line broadening of 150 Hz and (c) OPBA-5. Note that, spectra (b) and (c) match almost perfectly.

The corresponding ^{13}C $\{^1$H$\}$ CP/MAS NMR spectra of OPBA-3-DMF and OPBA-5 match rather well (cf. Figure 6.11, spectrum (a) and (c)) except for the tiny ^{13}C-signal at 172 ppm and the better resolution for OPBA-3-DMF. The additional resonance at 172 ppm indicates the presence of a minority component of carboxylic dimers. Over time and upon heating DMF is removed from the sample and pure OPBA-3 is gained, which explains that peak at 172 ppm. With the exception of this difference, all other resonances in the ^{13}C $\{^1$H$\}$ CP/MAS NMR spectrum have rather similar chemical shifts. The difference in the spectral resolution is due to the fact that OPBA-3-DMF forms a regular crystal lattice whereas OPBA-5 does not. To account this difference, the ^{13}C $\{^1$H$\}$ CP/MAS NMR spectrum of OPBA-3-DMF was processed with an additional line broadening of 150 Hz (see Figure 6.11 b), which obscures the fine splitting. Spectra (b) and (c) match almost perfectly, underlining the similarity of both spectra and, hence, indicating a comparable solid-state packing of OPBA-3-DMF and OPBA-5. To verify the structural consistencies of OPBA-3-DMF and OPBAs with n $\geq$ 2 with an independent probe, WAXS was performed (shown in Figure 6.12). The wide angle range ($2\theta > 15^\circ$) reflects the local structure comparable to solid-state NMR. OPBA-3-DMF give rise to about eleven reflexes in the WAXS spectrum, while OPBA-5 gives rise to only three reflexes. This difference can be explained again by the fact that OPBA-3-

DMF is more crystalline than OPBA-5. However, the three reflexes at 2θ = 20.3, 23.7, and 27.8 for OPBA-5 are in agreement with reflexes observed for OPBA-3-DMF.

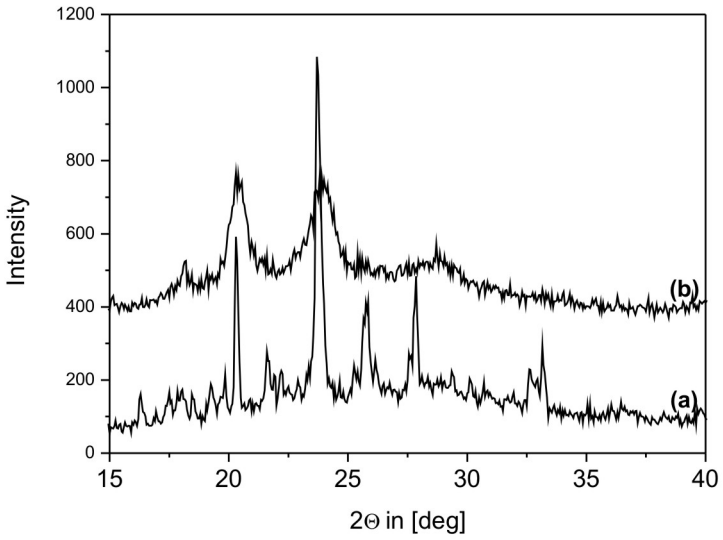

Figure 6.12.: WAXS pattern of (a) OPBA-3-DMF and (b) OPBA-5 underlining the structural similarity of the materials.

In agreement with the NMR data, the match of the main reflexes in the WAXS patterns mirrors the structural consistency of OPBA-3-DMF and OPBA-5. Hence, the structure of OPBA-3-DMF contains information about the packing and the hydrogen bonding network of OPBAs with n $\geq$ 2. Since OPBA-3 forms a co-crystal with DMF, a single-crystal X-ray structure can be obtained.[115] This single-crystal X-ray structure shown in Figure 6.13 exhibits, like the structure of pure OPBA-3 (shown in Figure 6.10), peptide like hydrogen bonding between NH groups and carbonyl groups of different molecules. Deviation from pure OPBA-3, all NH hydrogen bonds are within the plane and a regular β-sheet like layered structure results with all head groups pointing in the same direction. The layers are stacked in an alternate fashion and are shifted by one benzene ring every third layer. Due to the suppression of the carboxylic acid hydrogen bonds, the hydrogen bonding of the NH-groups is formed in a highly ordered fashion.

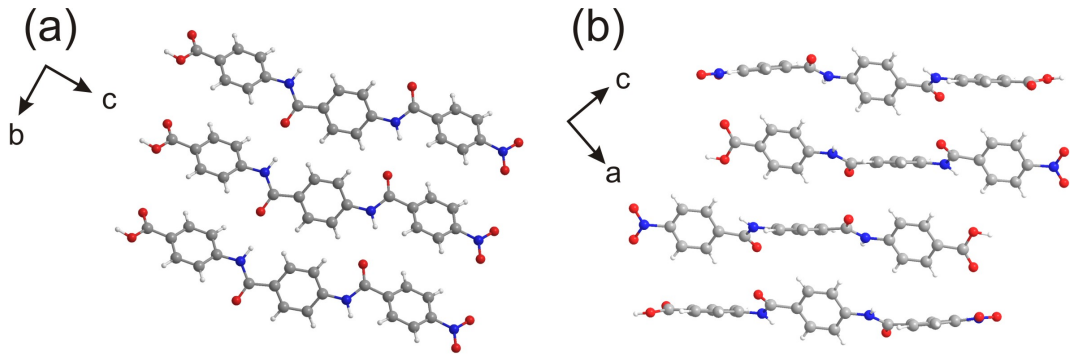

Figure 6.13.: Projections of the OPBA-3-DMF single-crystal X-ray structure.[115] (a) Amide hydrogen bonding within a layer and the formation of a β-sheet like structure, (b) stacking between the layers.

These structural features are likely present in OPBAs with n $\geq$ 2. It is expected that longer OPBAs form a regularly layered β-sheet like hydrogen-bonded structure with no linkage of the head groups within one layer (see Figure 6.13a). Moreover π–π-stacking interactions are present between the layers (see Figure 6.13b).

In summary, it could be shown how the number of repeat units influences the hydrogen bonding network in unsubstituted OPBAs. For OPBA-2 and OPBA-3, the dominating effect for the structure is the dimer formation of two COOH groups. In contrast, for OPBAs with n $\geq$ 2, NH hydrogen bonding is dominant and a regular β-sheet-like hydrogen bonded network is formed. In the latter case no indication for a hydrogen bond formation of the COOH groups could be found.

6.4. Aggregation of OPBA-PEG Copolymers in the Solid State

The gained knowledge about unsubstituted OPBAs in the previous section can now be used to understand the structure and aggregation behavior of OPBAs incorporated in the rod–coil copolymer. This copolymer is obtained by chemically linking the rod to PEG-polymers according to the synthetic scheme described in section 6.1. Potential structural changes of the OPBA rod within the copolymer compared to unsubstituted OPBAs can be monitored via ^{13}C $\{^1H\}$ CP/MAS NMR. The corresponding spectra of OPBA-5 and OPBA-7-PEG110 are shown in Figure 6.14 (a).

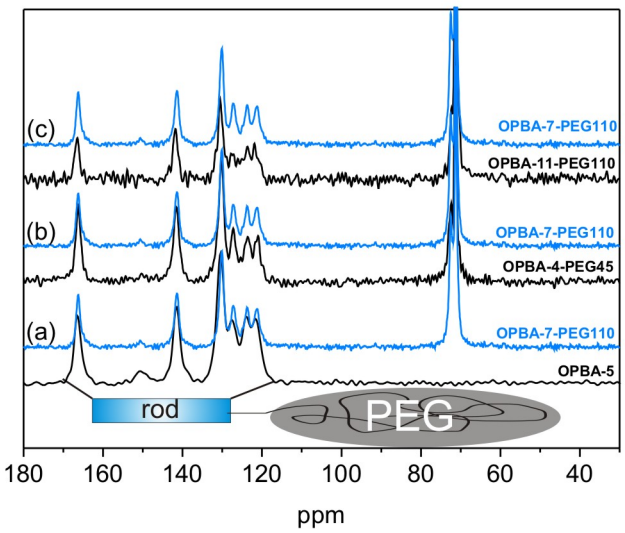

Figure 6.14.: ^{13}C $\{^{1}H\}$ CP/MAS NMR spectra of (a) OPBA-5 (black) and OPBA-7-PEG110 (blue) (b) OPBA-4-PEG45 (black) and OPBA-7-PEG110 (blue) and (c) OPBA-11-PEG110 (black) and OPBA-7-PEG110 (blue).

The resonances attributed to the OPBA rod within the copolymer appear in the same region of 110 ppm to 165 ppm as in unsubstituted OPBAs. Comparison of the ^{13}C signals show a good match of the unsubstituted OPBAs and the OPBA rods incorporated in the polymer (shown in Figure 6.14 (a)). The additional signal at 70 ppm reflects resonances from the PEG coil. Since the coil length may influence the structure, a comparison of the ^{13}C $\{^{1}H\}$ CP/MAS NMR spectra of OPBA-7-PEG110 and OPBA-4-PEG45 is shown in Figure 6.14 (b). Although the length of the PEG coil is more than doubled, the ^{13}C $\{^{1}H\}$ CP/MAS NMR spectrum was not changed. The same consistency of the ^{13}C signals is observed when changing the rod length (cf. Figure 6.14 (c)). From the consistency of the ^{13}C signals, it can be concluded that the structure of OPBA remains unaffected upon attachment of a PEG coil and upon variation of both coil and rod length.

Based on the observations that a) the structure of OPBAs with $n \geq 2$ is very similar to the structure of OPBA-3-DMF and that b) the structure of OPBA rods within the copolymer reflects that of the unsubstituted OPBAs, a tentative packing of the rod–coil copolymer can be proposed. (cf. Figure 6.15)

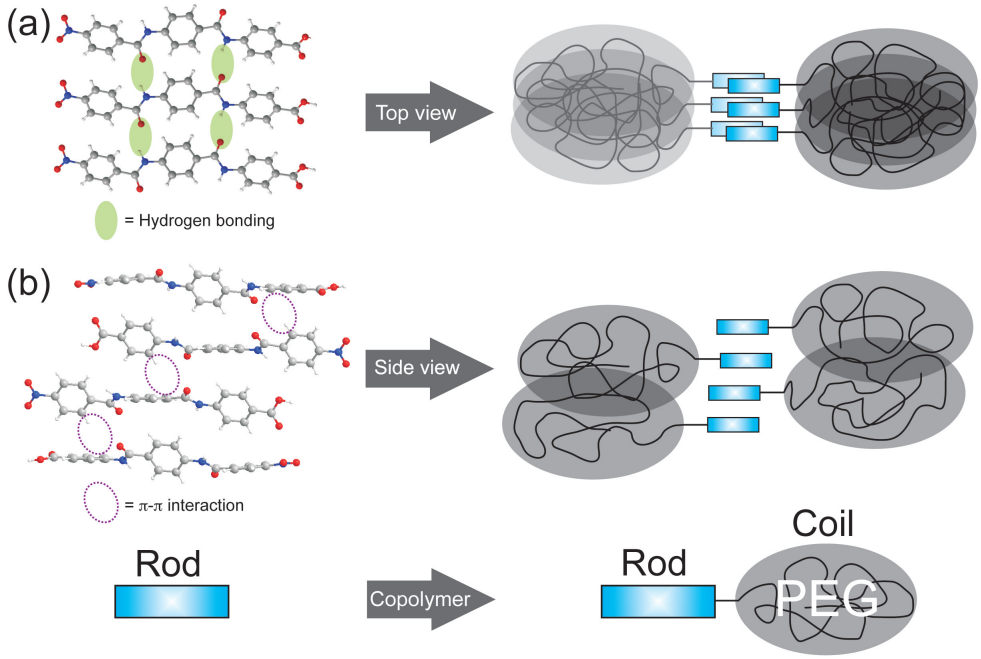

Figure 6.15.: Schematic structure of the rod–coil copolymer. (a) Aggregation within a layer with hydrogen bonding as driving force. (b) Aggregation between the layers π–π-interactions as driving force.

The rod block is depicted as a blue box, and the volume filling PEG coil is described by an elongated sphere.[125] Within a layer, a β-sheet-like hydrogen bonding network is built with all PEG chains oriented in the same direction. Between the layers π–π-stacking interactions are present and the polymer chains are oriented in an alternate way. The fact that the oligomers are oriented in the same direction within one layer might raise the question, how such a packing could lead to a proper space filling structure. In similar rigid rod systems with alkyl side chains of different lengths, it was observed that the flexibility of these chains allows for a dense packing imposed by the rods.[126] In the present case of OPBA with attached PEG chains this will be even easier, since such chains are known to be more flexible.[125] The corresponding supramolecular structure is referred to as a hockey-puck micelle where the driving forces for packing within the layer are higher than the driving forces for the packing of the layers. This corresponds well to the results for micelles in solution (cf. section 6.2), which exhibits an aggregate size of about 20–35 nm within a layer and a height of about 2 nm.[115] The strong hydrogen bonds within a layer and the weak π–π-stacking interactions between the layers give rise to the observable difference in the aggregate dimension by a factor of 10. However, the published aggregation in solution and the

suggested packing in the solid is slightly different. SFM topography images suggested a bilayer arrangement of the inner rod core for micelles in solution. While SFM can give very accurate height dimensions, the finite size of the scanning tip limits the lateral accuracy of the images. Considering, the tip geometry and analyzing the SFM phase contrast images, the existence of bilayer hockey-puck micelle is very unlikely.

To support the suggested packing model, a 2D ^{1}H–^{1}H DQ–SQ MAS NMR and a ^{13}C/^{1}H REPT-HSQC NMR spectrum of OPBA-7-PEG110 were recorded (cf. Figure 6.16).

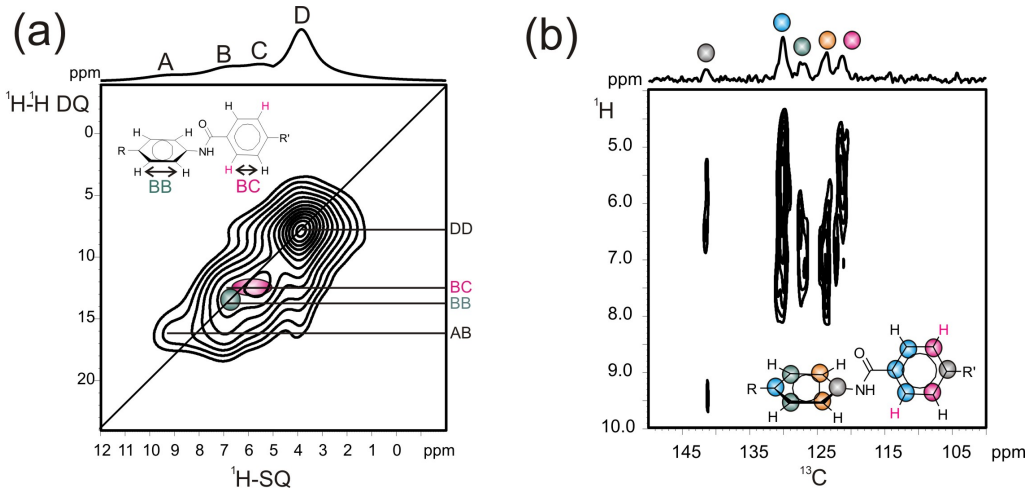

Figure 6.16.: (a) 2D ^{1}H–^{1}H DQ–SQ MAS NMR spectrum recorded at 250 K and 30 kHz MAS with $1\tau_R$ recoupling. (b) REPT-HSQC spectrum of OPBA-7-PEG110 measured at 25 kHz MAS and $2\tau_R$ recoupling.

The 2D ^{1}H–^{1}H DQ–SQ MAS NMR spectrum of OPBA-7-PEG110 was recorded at a low temperature (250 K) to suppress the intense PEG signal. In the projection, besides the signal at 3.8 ppm (resonance D) assigned to PEG, three additional resonances at 9.1 ppm (resonance A), 7 ppm (resonance B), and 5.5 ppm (resonance C) are observed. The signal at 9.1 ppm can be assigned to the amide protons, which are directly observable at that temperature due to a better resolution. The remaining two peaks at 7 ppm and 5.5 ppm originate from aromatic protons. The chemical shift of 5.5 ppm indicates π–π-stacking interactions present in the system. This is in agreement with the suggested structure and the corresponding protons are marked in red (cf. chemical structure Figure 6.16 (a)).[26] Two correlation peaks are rather important to confirm the suggested stacking. The cross peak BC which indicates contacts among aromatic protons with and without π–π-stacking and the auto peak BB which indicates contacts among aromatic protons without π–π-stacking interactions. Both correlation

are also illustrated in the inset Figure 6.16 and have been expected from the suggested structure as displayed in Figure 6.15 (b).

Additional insights into the local packing can be derived from the $^{13}C/^{1}H$ REPT-HSQC NMR spectrum shown in Figure 6.16 (b). The peak assignment is outlined by the color code. Not only the proton chemical shift is affected by π–π-stacking interactions, but also the ^{13}C chemical shift.[28] Two carbon atoms (green and orange)are only in proximity to protons without π–π-stacking interaction while the other two carbon atoms (blue and red) shows contacts to protons with and without π–π-stacking interactions. This corroborates the assignment by ^{1}H–^{1}H DQ–SQ MAS NMR and the suggested structure shown in Figure 6.15.

In this section, structural knowledge about unsubstituted OPBAs was utilized to understand the structure and aggregation of rod–coil copolymers based on OPBAs and to propose a complex aggregation model. It could be shown that the rod and coil lengths hardly affect the final equilibrium structure.

6.5. Phase Behavior of OPBA-PEG Copolymers

From the literature it is known that rod–coil copolymers exhibit an interesting phase behavior.[61,108–111] For OPBA-7-PEG110 this is studied in the following section. Beside all structural similarities discussed in the previous section, the resolution in the ^{13}C $\{^{1}H\}$ CP/MAS spectrum of the copolymer is significantly increased compared to the corresponding unsubstituted OPBAs. This is underlined by comparing the ^{13}C $\{^{1}H\}$ CP/MAS spectra of OPBA-6 and OPBA-7-PEG110 (Figure 6.17).

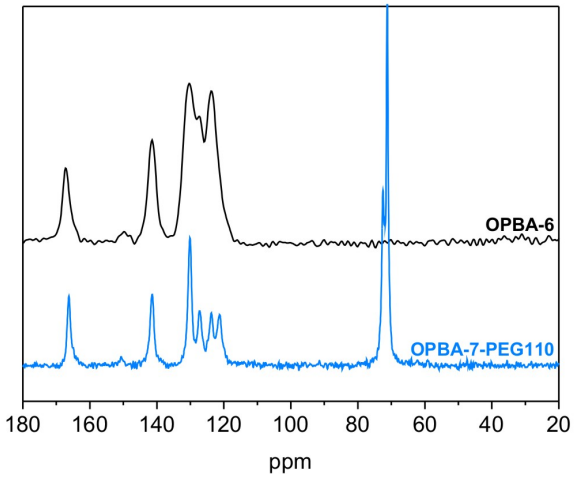

Figure 6.17.: ^{13}C $\{^{1}H\}$ CP/MAS NMR spectrum of OPBA-6 (black) and OPBA-7-PEG110 (blue).

The resonances assigned to the OPBA rod appear in the region of 110 ppm to 165 ppm. In case of the copolymer the aromatic signals are much better resolved, although the rod part includes more repeat units. This is surprising since an increasing number of repeat units of unsubstituted OPBAs leads to a dramatic decrease in resolution (cf. Figure 6.4). The increased resolution of a ^{13}C $\{^{1}H\}$ CP/MAS solid-state NMR spectrum can originate from two effects: either the mobility or the local order of the OPBA rod incorporated in the copolymer has increased. To clarify this question, the mobility of the rod segment was analyzed via the $^{13}C/^{1}H$ REPT-HDOR method (cf. Figure 6.18). The red spectra corresponds to the measured $^{13}C/^{1}H$ dipolar sideband pattern and the black spectra are the fitting curves. Since multispin interactions affect the innermost dipolar sidebands the third and forth sidebands were chosen to evaluate the goodness of the fit. For OPBA-5 and OPBA-7-PEG110 the dipolar sideband pattern relates to the aromatic ^{13}C resonance at 123 ppm. The fitted sideband pattern are shown in Figure 6.18. For both OPBA-7-PEG110 and OPBA-5, the measured $^{13}C/^{1}H$ dipolar coupling constant of 18 kHz ($\pm$ 0.5 kHz), indicates that the aromatic rings are rather rigid (for a completely rigid system 21 kHz is expected).

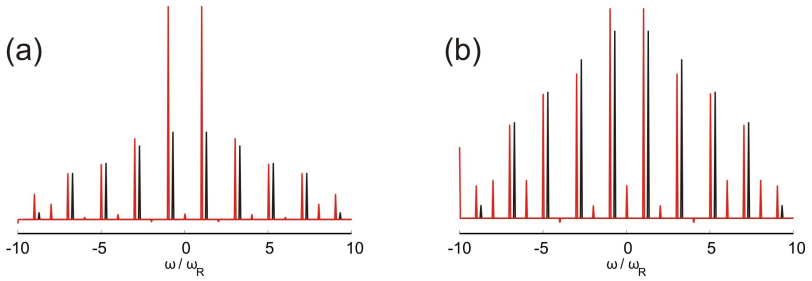

Figure 6.18.: $^{13}C/^{1}H$ REPT-HDOR side band pattern of **(a)** OPBA-5 and **(b)** OPBA-7-PEG110. The measurement was performed at 25 kHz MAS and 4 rotor periods recoupling.

The almost identical $^{13}C/^{1}H$ dipolar coupling constants indicate that the mobility of the OPBA rod is unaffected by attachment of PEG chains. Thus, the increased spectral resolution in the ^{13}C $\{^{1}H\}$ CP/MAS spectrum stems from a higher local order of the rod structure. Apart from phase separation and aggregation, another important characteristic of rod–coil copolymers is their ability to form liquid-crystalline phases.[107,109,111] Indeed the DSC trace shows an exothermic peak at 332 K for OPBA-7-PEG110. To study the effect of this transition on the structure, VT-^{13}C $\{^{1}H\}$ CP/MAS measurements in the temperature range up to 340 K were performed to monitor possible changes of the structure (cf. Figure 6.19).

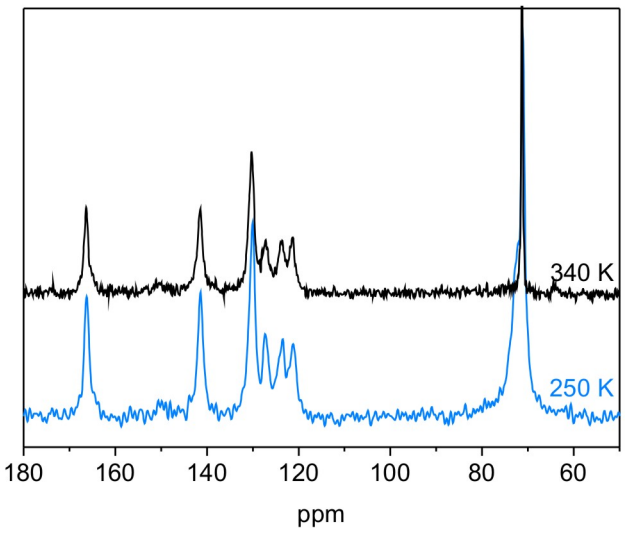

Figure 6.19.: ^{13}C $\{^{1}H\}$ CP/MAS NMR spectra of OPBA-7-PEG110 recorded at 250 K (black) and 340 K (blue).

The ^{13}C $\{^{1}H\}$ CP/MAS NMR spectra recorded at temperatures of 250 K and 340 K, i.e. well below and slightly above the phase transition are shown. While the OPBA signals in the range of 120 to 160 ppm exhibit hardly any changes, the PEG signal at 71 ppm narrows substantially from 130 Hz at 250 K to 50 Hz at 340 K. Hence, the phase transition detected by DSC reflects a melting of the PEG block. This is in agreement with a statement in the literature that the rod-like character is retained under virtually all circumstances.[107]

The formation of a liquid-crystalline phase was probed with a polarization optical microscope (POM). The corresponding images are shown in Figure 6.20. These indeed show that a liquid-crystalline phase is formed above the melting temperature for all the examined rod–coil copolymers. The sample exhibit alternately birefringent and dark textures every 45° (cf. Figure 6.20 A and B). Non specific textures can be sheared but could not be assigned to a certain kind of mesophase. It is known that the presence of a liquid-crystalline phase favors supramolecular organization when cooling down to a solid phase.[44,50] Thus, the better local order of the aggregation in the rod–coil copolymer noted above is likely to be due to a preorganization in the liquid-crystalline phase.

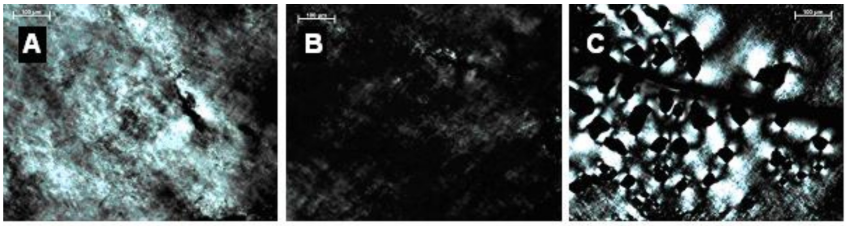

Figure 6.20.: Polarization optical microscope images of OPBA-4-PEG45 at 105°C. (A) and (B) show the same position of the sample rotated by 45°. (C) Birefringent nonspecific texture.

6.6. Conclusion

The structures of unsubstituted OPBAs and OPBA-PEG rod–coil copolymers were studied by solid-state NMR, XRD, DSC, and POM. A dependency between the number of repeat units, the hydrogen bonding network, and hence, the structural features was found. The structures of OPBAs with two and three repeat units are driven by the dimer formation of their carboxylic acid groups. For longer OPBAs with at least four

repeat units, an equilibrium structure was found. In this equilibrium structure, no dimer formation could be detected. Remarkably stable layered β-sheet-like aggregates are formed. The structural difference is due to the fact that the number of amide hydrogen bonds increases with an increasing size of the rod, whereas the formation of the carboxylic dimers is limited to the end groups. Blocking the end groups of OBPA-3 by DMF, a single crystal could be obtained, which reflects the structural features of longer OPBAs as checked by ^{13}C $\{^{1}$H$\}$ CP/MAS NMR and XRD. The equilibrium structure of the long OPBAs is retained after PEG attachment, leading to a rod–coil copolymer. Transferring the structural ideas from OPBA-3-DMF to longer OPBAs to the copolymer, a complex aggregation model could be proposed. Further, the transition to a liquid-crystalline phase at elevated temperatures could be ascribed to a melting of the PEG coil while the aggregates of the OPBA rods are retained. The preorganization in the liquid-crystalline phase lead to an improvement of the local order for the OPBA rod in the copolymer. This has been also observed for the macrocycle in Chapter 4, were the liquid-crystalline phase is also able to improve the local order of the SPM-1 macrocycle.

7. Conclusion

In this work supramolecular organic systems based on rigid π-conjugated building blocks and flexible side chains were studied via solid-state NMR spectroscopy. Specifically, these studies focussed on phenylene ethynylene based macrocycles, polymer systems including polythiophenes, and rod–coil copolymers of oligo(p-benzamide) and poly(ethylene glycol). All systems were studied in terms of the local order and mobility. The central topic of this dissertation was to elucidate the role of the flexible side chains in interplay of different non-covalent interactions, like π–π-stacking and hydrogen bonding.

Shape Persistent Macrocycles

The macrocycles which were studied feature a balance between the size of the alkyl side chains and the rigid ring. Hence, the kind of alkyl chains crucially affects the structure, the liquid crystallinity, and the local order. However, it is not easy to predict, which kind of alkyl chains influences the system in which direction. Unbranched longer alkyl chains are able to stabilize the corresponding macrocycle in highly ordered hexagonal columns in the liquid-crystalline phase. In these columns all inner rings of the system are stacked on top of each other with a pitch angle of 60°. π–π-stacking interactions are present between the rings and the whole system is rather rigid. In contrast, macrocycles with shorter and branched alkyl chains, though exhibiting the same liquid-crystalline phase transition, are not able to form well ordered columnar stacks in this phase. Instead the whole system shows an increased local mobility. This difference is attributed to the different space filling properties of the attached alkyl side chains. Longer and unbranched alkyl chains are better able to fill the intercolumnar space, compared to shorter and branched alkyl chains. Thus, the local order is improved and the mobility is reduced.

Thiophene-based Conducting Polymers

In the second part of this thesis poly(3-alkylthiophenes) P3ATs were in the focus. Compared to the macrocycles less flexible alkyl side chains are attached to the rigid polymer backbone. Hence, a variation of the alkyl chain length only imposes minor effects on the structure of the rigid backbone. However, longer alkyl side chains do lead to an

improvement of the local order and to a decrease of the local mobility, in accordance with the results found for the macrocycles. In the bulk polymer, two different modifications were found for all P3ATs: a crystalline fraction denoted modifications A and an amorphous fraction denote as modification B. It could be shown that the packing of both modifications are different. In modification A the layers are stacked on top of each other such that π–π-stacking interactions are observable. In contrast, modification B does not show π–π-stacking interactions, since the π-stacking distance between adjacent layers is to large, as confirmed by a 2D ^{1}H/^{1}H correlation experiment. Combined with theoretical calculations, two possible packing models for modification A are suggested. In the bulk, the crystalline modification is incorporated in an amorphous matrix. By comparing WAXS and solid-state NMR data the crystalline modification A can be related to modification I assigned by WAXS. The second crystalline modification described in the literature could not be observed in any of the studied polymers.

For possible applications the solid-state packing and properties of the polymers blended with the fullerene derivative PCBM are of considerable interest. Two different bulk heterojunction systems were studied in more detail, a mixture of P3HT and PCBM and a mixture of the more complex polymer PCPDTBT and PCBM. The local order of P3HT-PCBM decreases dramatically with respect to both components. The system is rather sensitive to thermal treatment and phase separates after annealing. In the phase separated domain of P3HT, crystal modification I is found again like in the bulk polymer. In contrast, the PCBM domain is rather amorphous and ill defined. This behavior seems to be rather independent of the ratio between the two polymeric components. The system based on PCPDTBT behaves differently. The bulk polymer has a low local order and no crystalline modification could be detected. In contrast in an aged blend with PCBM both components starts to crystallize. Crystallization can also be achieved by annealing.

Rod–Coil Copolymers

In the last part of this thesis, a rod–coil copolymer based on oligo(p-benzamide) (OPBA-rod) and poly(ethylene glycol) (PEG-coil) was studied. In this system, the rigid conjugated π-system constitutes the minor component. The study was started with unsubstituted OPBA rods. These are able to form strong hydrogen bonds, which is the main reason for their rigidity. Neat OPBAs have two sources of hydrogen bonding: carboxylic acid end groups and amide groups interconnecting phenylene units. There is a dependency between the number of repeat units, the hydrogen bonding network, and hence, the structural features. The self-assembly of OPBAs with two

and three repeat units is driven by dimer formation of the carboxylic acid groups. For longer OPBAs with at least four repeat units an equilibrium structure was found. This consisted of layered β-sheet like aggregates, due to the hydrogen bonding of the amid groups. In contrast, the hydrogen bonding of the carboxylic acid end groups is absent, due to the fact that the number of amide hydrogen bonds is increasing with increasing rod size, whereas the formation of the carboxylic dimers is limited to the end groups. A detailed structural idea of the equilibrium structure could be obtained from the single crystal X-ray structure of OPBA-3-DMF, which shows similar structural features, confirmed by XRD investigations. Within the rod–coil copolymers this equilibrium structure is retained. Hence, it was further possible to transfer the structural ideas from OPBA-3-DMF to longer OPBAs towards the copolymer and a complex aggregation model was achieved. In addition, the phase behavior was studied and it was found that at elevated temperatures a transition to a liquid-crystalline phase of the rod–coil copolymer is observed by DSC. This has been ascribed to melting of the PEG coil, where the aggregates of the OPBA rods are retained. Due to the preorganization in the liquid-crystalline phase an improvement of the local order is observed for the OPBA rod in the copolymer.

Combining the results of this work, it can be concluded that the ratio of the rigid block and the attached alkyl side chains can be crucial for the design of an ordered π-conjugated supramolecular system. Through alkyl side chains, it is also possible to introduce liquid-crystalline phases in the system, which can foster the local order of the system. Moreover in the studied system longer, unbranched alkyl side chains are better suited to stabilize the corresponding aggregation than shorter, branched ones.

The combination of non-covalent interactions such as π–π-stacking and hydrogen bonding play an important role for structure formation. However, the effect of π–π-stacking interaction is much weaker than the effect of hydrogen bonding and is only observed in systems with a suitable local order. Hence, they are often not strong enough to control the local order. In contrast, hydrogen bonds predominantly influence the structural organization and packing. In comparison the size of the alkyl side chains is only of minor importance. The suppression of certain hydrogen bonds can lead to completely different structures and can induce a specific aggregation behavior. Thus, for the design of a supramolecular ordered system the presence of hydrogen bonding efficiently stabilizes the corresponding structure, but the ratio of hydrogen bond forming groups should be kept low to be able to influence the structure selectively.

A. Sample Preparation

A.1. Macrocycles

SPM-1 and SPM-2 have been prepared at the Kekulé-Instituts for organic chemistry and biochemistry University of Bonn in the group of Prof. Sigurd Höger who also provided the corresponding DSC and WAXS data.

A.2. Thiophene based polymers

All investigated P3ATs and P3OctiT have been prepared at the Bergische University of Wuppertal in the group of Prof. Ullrich Scherf. PCPDTBT and P3HT-PCBM have been provided by the Konarka. All additional films have been prepared via drop coating with PCPDTBT from Konarka and PCBM from Alldrich.

A.3. Rod–coil copolymers

The OPBAs and corresponding copolymers have been prepared at the Johannes Gutenberg University Mainz in the group of Dr. Andreas F. M. Killbinger.

B. Methods

B.1. Solid-State NMR

^{1}**H MAS NMR** measurements have been performed at a Bruker Avance 700 MHz or a Bruker Avance-III 850 MHz spectrometer using 30 kHz MAS and a $\pi/2$-pulse of 2.5 μs. The recycle delay strongly depends on the samples. For the macrocycles, the polythiophene and the rod–coil copolymer systems a recycling delay of 5 s have been use and for unsubstituted OPBAs 60 s.

^{2}**H MAS NMR** measurements have been performed at a Bruker Avance 700 MHz spectrometer using 25 kHz MAS, a recycle delay of 20 s and a $\pi/2$ pulse of 2.5 μs.

^{1}**H–**^{1}**H DQ–SQ MAS NMR** have been performed at a Bruker Avance 700 MHz for the polythiophene and the rod–coil copolymers and at a Bruker Avance-III 850 MHz for the macrocycles using 30 kHz MAS and a $\pi/2$ pulse of 2.5 μs. The back to back (BABA) recoupling sequence was used applying States-TPPI for phase sensitive detection.[21] The recycle delay have been varied between 2 and 60 s. The number of t_1-slices have been between 72 and 256 and for each slice 16 or 32 transients were recorded.

^{13}**C CP/MAS NMR** measurements were carried out at 125.77 MHz (Bruker Avance 500 machine) using 25 kHz MAS and a $\pi/2$-pulse of 2.5 μs. Spectra were measured normally with a CP contact time of 3 ms, 4096 scans, a recycle delay of 2 s and TPPM decoupling.[14]

^{15}**N CP/MAS NMR** measurements were carried out at 30.42 MHz (Bruker Avance 300 machine) using 5 kHz MAS and a $\pi/2$-pulse of 5 μs. Spectra were measured with a CP contact time of 9 ms, between 8192 and 32768 scans, a recycle delay of 10 s and TPPM decoupling.[14]

REPT-HSQC experiments[127] were carried out using a Bruker Avance-III 850 spectrometer with a ^{13}C resonance of 213 MHz and a $\pi/2$-pulse of 2.5 μs. The measurement was acquired with 2 or 4 rotor periods recoupling, 72 increments in the indirect dimension, 1024 transients per increment and a recycle delay of 2 s.

FSLG-decoupled CP HETCOR measurements were carried out using a Bruker Avance-III 850 spectrometer with a ^{13}C resonance of 213 MHz, 15 kHz MAS and a $\pi/2$-pulse

of 2.5 μs. The measurement was acquired with a CP contact time of 3 ms. The experiment used a recycle delay of 2 s, 72 t_1 increments where each t_1 increment had a span of five basic FSLG blocks (81.6 μs), high power TPPM decoupling and States-TPPI for phase sensitive detection.[14,21]

REPT-HDOR measurements[41] were performed using a Bruker Avance 500 or a Avance-III 850 MHz spectrometer at 25 kHz MAS and a $\pi/2$-pulse of 2.5 μs. The experiment was measured employing 4 rotor periods recoupling, 20 increments in the indirect dimension, about 1024 transients per increment, and a recycle delay of 2 s. For analysing the data a home written Matlab routine have been used which is based on the dipolar coupling of a two spin system.[42]

Variable temperature measurements have been performed with a heating rate of 2 K/min. Before the measurement was started a tempering time of 20 minutes was used. All given temperature values in this thesis are the relative values at the corresponding spectrometer and not the absolut values from the sample.

All ^{1}H- and ^{13}C- MAS NMR spectra were referenced with respect to tetramethyl silane (TMS) using solid tetrakis(trimethylsilyl)silane (TTSS, 0.27 ppm) and solid adamantane (29.456 ppm) as a secondary standard.[128,129] For ^{15}N CP/MAS NMR nitromethane is used as a standard using solid $^{15}NH_4NO_3$ (-358.4 ppm) as a secondary standard.[38]

B.2. WAXS

Wide angle X-ray scattering measurements of the rod–coil copolymers were carried out with a D8 Advanced Bruker on powder samples on a glass substrate.

B.3. POM

POM observations were made with a Zeiss Axioscop 40 equipped with a Linkam THMS600 hot stage.

B.4. DSC

DSC was performed on a DSC 822 (METTLER TOLEDO) under N_2 atmoshere with a heating rate of 10 K/min.

B.5. Theoretical calculations

All model structures were optimized with Gaussian03 package[130] in the framework of DFT using the B3LYP exchange-correlation functional[131,132] and 6-31+G(d,p) basis set. The nuclear independent chemical shift (NICS) maps were computed with the CPMD package[133] in the framework of DFT using the gradient-corrected exchange[134] and correlation functionals,[135] Goedecker-type pseudo-potentials[136,137] together with a plane wave cutoff of 70Ry. The NICS maps are providing the information about the influence of the polymer layers and their fragments on the neighbor moieties (on their NMR chemical shifts, particularly) and hence explaining the packing effect observed in the solid-state NMR spectra.

References

[1] Meyer, C. *Spiegel* **2010,** *10,* 50–54.

[2] Levitt, M. H. *spin dynamics - Basic of Nuclear Magnetic Resonance;* Wiley, Chichester: 2006.

[3] Spiess, H. W.; Diehl, P.; Fluck, E.; Günther, H.; Kostfeld, R.; Seelig, J. *NMR Basic Principles and Progress;* Springer Verlag, Berlin: 1978.

[4] Ooms, K. J.; Terskikh, V. V.; Wasylishen, R. E. *J. Am. Chem. Soc.* **2007,** *129,* 6704–6705.

[5] Keeler, J. *Understanding NMR Spectroscopy;* Wiley, Chichester: 2006.

[6] Duer, M. J. *Introduction to Solid State NMR Spectroscopy;* Blackwell Publishing, Oxford: 2004.

[7] Hore, P. J.; Jones, J. A.; Wimperis, S. *NMR: The Toolkit;* Oxford Science Publications: 2009.

[8] Anet, F. A. L.; O'Leary, D. J. *Concepts Magn. Reson.* **1991,** *3,* 193–214.

[9] Laws, D. D.; Bitter, H.-M. L.; Jerschow, A. *Angew. Chem.* **2002,** *114,* 3224–3259.

[10] P. P. Man, Quadrupolar interactions. In *Encyclopedia of Nuclear Magnetic Resonance*, Vol. 9: Advances in NMR; Grant, D.; Harris, R., Eds.; John Wiley & Sons, Ltd: Chichester, England, 2002.

[11] Brown, S. P. *Prog. Nucl. Magn. Reson. Spectrosc.* **2007,** *50,* 199–251.

[12] Schnell, I. *Prog. Nucl. Magn. Reson. Spectrosc.* **2004,** *45,* 145–207.

[13] Fung, B. F.; Khitrin, A. K.; Ermolaev, K. *J. Magn. Reson.* **2000,** *142,* 97–101.

[14] Bennett, A. E.; Rienstra, C. M.; Auger, M.; Lakshmi, K. V.; Griffin, R. G. *J. Chem. Phys.* **1995,** *103,* 6951–6958.

[15] and. A. C. Kolbert, A. B.; Levitt, M. H. *Chem. Phys. Lett.* **1989,** *155,* 341–346.

[16] Brown, S. P.; Spiess, H. W. *Chem. Rev.* **2001,** *101,* 4125–4155.

[17] Gullion, T. *Concepts Magn. Reson.* **1998,** *10,* 277–289.

[18] Gullion, T.; Schaefer, J. *J. Magn. Reson.* **1989,** *81,* 196–200.

[19] Fischbach, I.; Ebert, F.; Spiess, H. W.; Schnell, I. *ChemPhysChem* **2004,** *5,* 895–908.

[20] Rance, M.; Wright, P. E. *J. Magn. Reson.* **1986,** *66,* 372–378.

[21] Feike, M.; Demco, D. E.; Graf, R.; Gottwald, J.; Hafner, S.; Spiess, H. W. *J. Magn. Reson. Ser. A* **1996,** *122,* 214–221.

[22] Chierotti, M. R.; Gobetto, R. *Chem. Commun.* **2008,** *14,* 1621–1634.

[23] Brunner, E.; Sternberg, U. *Prog. Nucl. Magn. Reson. Spectrosc.* **1998,** *32,* 21–57.

[24] Emmler, T.; Gieschler, S.; Limbach, H. H.; Buntkowsky, G. *J. Mol. Struct.* **2004,** *700,* 29–38.

[25] Yamauchi, K.; Kuroki, S.; Fujii, K.; Ando, I. *Chem. Phys. Lett.* **2000,** *324,* 435–439.

[26] Schmidt, J.; Hoffmann, A.; Spiess, H. W.; Sebastiani, D. *J. Phys. Chem. B* **2006,** *110,* 23204–23210.

[27] Gu, Z. T.; Redenour, C. F.; Bronnimann, C. E.; Iwashita, T.; McDermott, A. *J. Am. Chem. Soc.* **1996,** *118,* 822–829.

[28] Lazzeretti, P. *Prog. Nucl. Magn. Reson. Spectrosc.* **2000,** *36,* 1–88.

[29] Pines, A.; Rhim, W.-K.; Waugh, J. S. *J. Magn. Reson.* **1972,** *6,* 457–465.

[30] Pines, A.; Gibby, M. G.; Waugh, J. S. *J. Chem. Phys.* **1973,** *59,* 569–590.

[31] Hartmann, S. R.; Hahn, E. L. *Phys. Rev.* **1962,** *128,* 2042–2053.

[32] Bugay, D. E. *Pharm. Res.* **1993,** *10,* 317–327.

[33] Hesse, M.; Meier, H.; Zeeh, B. *Spektroskopische Methoden in der organischen Chemie;* Thieme, Stuttgart, New York: 2005.

[34] Harris, R. K. *Analyst* **2006,** *131,* 351–373.

[35] Harris, R. K. *Solid State Sci.* **2004,** *6,* 1025–1037.

[36] Mason, J. *Multinuclear NMR;* Plenum Press: 1987.

[37] Schnell, I.; Spiess, H. W. *J. Magn. Reson.* **2001,** *151,* 153–277.

[38] Goward, G. R.; Schnell, I.; Brown, S. P.; Spiess, H. W.; Kim, H.-D.; Ishida, H. *Magn. Reson. Chem.* **2001,** *39,* S5–S17.

[39] Saalwächter, K.; Graf, R.; Spiess, H. W. *J. Magn. Reson.* **2001,** *148,* 398–418.

[40] van Rossum, B.-J.; Förster, H.; de Groot, H. J. M. *J. Magn. Reson.* **1997,** *124,* 516–519.

[41] Paul, S. M. D.; Saalwächter, K.; Graf, R.; Spiess, H. W. *J. Magn. Reson.* **2000,** *146,* 140–156.

[42] Saalwächter, K.; Schnell, I. *Solid State Nucl. Magn. Reson.* **2002,** *22,* 154–187.

[43] Hentschel, R.; Sillescu, H.; Spiess, H. W. *Polymer* **1981,** *22,* 1516–1521.

[44] Hansen, M. R.; Schnitzler, T.; Pisula, W.; Graf, R.; Müllen, K.; Spiess, H. W. *Angew. Chem. Int. Ed.* **2009,** *48,* 4621–4624.

[45] Lei, S.; Heyen, A. V.; Feyter, S. D.; Surin, M.; Lazzaroni, R.; Rosenfeldt, S.; Ballauf, M.; Lindner, P.; Mössinger, D.; Höger, S. *Chem. Eur. J.* **2009,** *15,*.

[46] Zhao, D.; Moore, J. S. *Chem. Commun.* **2003,** 807–818.

[47] Becker, K.; Fritzsche, M.; Höger, S.; Lupton, J. M. *J. Phys. Chem. B* **2008,** *112,* 4849–4853.

[48] Höger, S.; Weber, J.; Leppert, A.; Enkelmann, V. *Beilstein J. Org. Chem.* **2008,** *4,* 1–8.

[49] Höger, S. *J. Polym. Sci. Part A: Polym. Chem.* **1999,** *37,* 2685–2698.

[50] Percec, V.; Glodde, M.; Bera, T. K.; Miura, Y.; Shiyanovskaya, I.; Singer, K. D.; Balagurusamy, V. S. K.; Heiney, P. A.; Schnell, I.; Rapp, A.; Spiess, H. W.; Hudson, S. D.; Duan, H. *Nature* **2002,** *417,* 384–387.

[51] Wegner, M. *Dissertation;* Johannes-Gutenberg Universität Mainz: 2010.

[52] Bohle, A.; Brunklaus, G.; Hansen, M. R.; Schleuss, T.; Kilbinger, A. F. M.; Seltmann, J.; Spiess, H. W. *Macromolecules* **2010,** *43,* 4978–4985.

[53] Fritsche, M. *Dissertation;* Universität Bonn: 2010.

[54] Fischer, M.; Lieser, G.; Rapp, A.; Schnell, I.; Mamdouh, W.; Feyter, S. D.; Schryver, F. C. D.; Höger, S. *J. Am. Chem. Soc.* **2004,** *126,* 214–222.

[55] Tasios, N.; Grigoriadis, C.; Hansen, M. R.; Wonneberger, H.; Li, C.; Spiess, H. W.; Müllen, K.; Floudas, G. *J. Am. Chem. Soc.* **2010,** *132,* 7478–7487.

[56] Koppe, M.; Egelhaaf, H.-J.; Dennler, G.; Scharber, M. C.; Brabec, C. J.; Schilinsky, P.; Hoth, C. N. *Adv. Funct. Mater.* **2010,** *20,* 338–346.

[57] Roncali, J. *Acc. Chem. Res.* **2009,** *42,* 1719–1730.

[58] Venkataraman, D.; Yurt, S.; Venkatraman, B. H.; Gavvalapalli, N. *Phys. Chem. Lett.* **2010,** *1,* 947–958.

[59] Günes, S.; Neugebauer, H.; Sariciftci, N. S. *Chem. Rev.* **2007,** *107,* 1324–1338.

[60] Chen, J.; Cao, Y. *Acc. Chem. Res.* **2009,** *42,* 1709–1718.

[61] Segalman, R. A.; McCulloch, B.; Kirmayer, S.; Urban, J. J. *Macromolecules* **2009,** *42,* 9205–9216.

[62] Peet, J.; Heeger, A. J.; Bazan, G. C. *Acc. Chem. Res.* **2009,** *42,* 1700–1708.

[63] Bredas, J.-L.; Norton, J. E.; Cornil, J.; Coropceanu, V. *Acc. Chem. Res.* **2009,** *42,* 1691–1699.

[64] Fruth, A.; Klapper, M.; Müllen, K. *Macromolecules* **2010,** *43,* 467–472.

[65] Boudouris, B. W.; Molins, F.; Blank, D. A.; Frisbie, C. D.; Hillmyer, M. A. *Macromolecules* **2009,** *42,* 4118–4126.

[66] Liang, F.; Lu, J.; Ding, J.; Movileanu, R.; Tao, Y. *Macromolecules* **2009,** *42,* 6107–6114.

[67] Egbe, D. A. M.; Türk, S.; Rathgeber, S.; Kühnlenz, F.; Jadhav, R.; Wild, A.; Birckner, E.; Adam, G.; Pivrikas, A.; Cimrova, V.; Knör, G.; Sariciftci, N. S.; Hoppe, H. *Macromolecules* **2010,** *43,* 1261–1269.

[68] He, X.; Gao, F.; Tu, G.; Hasko, D.; Hüttner, S.; Steiner, U.; Greenham, N. C.; Friend, R. H.; Huck, W. T. S. *Nano Letters* **2010,** *10,* 1302–1307.

[69] Brunetti, F. S.; Gong, X.; Tong, M.; Heeger, A. J.; Wudl, F. *Angew. Chem. Int. Ed.* **2010,** *49,* 532–536.

[70] McCullough, R. D. *Adv. Mater.* **1998,** *10,* 93–114.

[71] Chen, T.-A.; Wu, X.; Rieke, R. D. *J. Am. Chem. Soc.* **1995,** *117,* 233–244.

[72] Hiorns, R. C.; Khoukh, A.; Gourdet, B.; Dagron-Lartigau, C. *Polym. Int.* **2006,** *55,* 608–620.

[73] Soci, C.; Hwang, I.-W.; Moses, D.; Zhu, Z.; Waller, D.; Gaudiana, R.; Brabec, C. J.; Heeger, A. J. *Adv. Funct. Mater.* **2007,** *17,* 632–636.

[74] Norrman, K.; Alstrup, J.; Jorgensen, M.; Krebs, F. C. *Surf. Interface Anal.* **2006,** *38,* 1302–1310.

[75] Seemann, A.; Egelhaaf, H.-J.; Brabec, C. J. *Org. Electr.* **2009,** *10,* 1424–1428.

[76] Prosa, T. J.; Winokur, M. J.; McCullough, R. D. *Macromolecules* **1996,** *29,* 3654–3656.

[77] Prosa, T. J.; Winokur, M. J.; Moulton, J.; Smith, P.; Heeger, A. J. *Macromolecules* **1992,** *25,* 4364–4372.

[78] Ooserbaan, W. D.; Vrindts, V.; Berson, S.; Guillerez, S.; Douheret, O.; Ruttens, B.; D'Haen, J.; Adriaensens, P.; Manca, J.; Lutsen, L.; Vanderzande, D. *J. Mater. Chem.* **2009,** *19,* 5424–5435.

[79] Joshi, S.; Grigorian, S.; Pietsch, U.; Pingel, P.; Zen, A.; Neher, D.; Scherf, U. *Macromolecules* **2008,** *41,* 6800–6808.

[80] Joshi, S.; Grigorian, S.; Pietsch, U. *Phys. Status Solidi* **2008,** *205,* 488–496.

[81] Joshi, S.; Pingel, P.; Grigorian, S.; Panzner, T.; Pietsch, U.; Neher, D.; Forster, M.; Scherf, U. *Macromolecules* **2009,** *42,* 4651–4660.

[82] Morana, M.; Wegschneider, M.; Bonanni, A.; Kopidakis, N.; Shaheen, S.; Scharber, M.; Zhu, Z.; Waller, D.; Gaudiana, R.; Brabec, C. *Adv. Funct. Mater.* **2008,** *18,* 1757–1766.

[83] Morana, M.; Azimi, H.; Dennler, G.; Egelhaaf, H.-J.; Scharber, M.; Forberich, K.; Hauch, J.; Gaudiana, R.; Waller, D.; Zhu, Z.; Hingerl, K.; van Bavel, S. S. *Adv. Funct. Mater.* **2010,** *20,* 1180–1188.

[84] Yazawa, K.; Inoue, Y.; Yamamoto, T.; Asakawa, N. *Phys. Rev. B* **2006,** *74,* 094204.

[85] Yazawa, K.; Inoue, Y.; Shimizu, T.; Tansho, M.; Asakawa, N. *J. Phys. Chem. B* **2010,** *114,* 1241–1248.

[86] Bolognesi, A.; Porzio, W.; Provasoli, A.; Botta, C.; Comotti, A.; Sozzani, P.; Simonutti, R. *Macromol. Chem. Phys.* **2001,** *202,* 2586–2591.

[87] Kolbert, A. C.; Sariciftci, N. S.; Gaudl, K.-U.; Bäuerle, P.; Mehring, M. *J. Am. Chem. Soc.* **1991,** *113,* 8243–8246.

[88] Yang, C.; Hu, J. G.; Heeger, A. J. *J. Am. Chem. Soc.* **2006,** *128,* 12007–12013.

[89] Yamamoto, T.; Komarudin, D.; Arai, M.; Lee, B.-L.; Suganuma, H.; Asakawa, N.; Inoue, Y.; Kubota, K.; Sasaki, S.; Fukuda, T.; Matsuda, H. *J. Am. Chem. Soc.* **1998,** *120,* 2047–2058.

[90] Wu, Z.; Petzold, A.; Henze, T.; Thurn-Albrecht, T.; Lohwasser, R. H.; Sommer, M.; Thelakkat, M. *Macromolecules* **2010,** *43,* 4646–4653.

[91] Dag, S.; Wang, L.-W. *J. Phys. Chem. B* **2010,** *114,* 5997–6000.

[92] Maillard, A.; Rochefort, A. *Phys. Rev. B* **2009,** *79,* 115207-1–115207-6.

[93] Zen, A.; Saphiannikova, M.; Neher, D.; Grenzer, J.; Grigorian, S.; Pietsch, U.; Asawapirom, U.; Janietz, S.; Scherf, U.; Lieberwirth, I.; Wegner, G. *Macromolecules* **2006,** *39,* 2162–2171.

[94] Arosio, P.; Moreno, M.; Famulari, A.; Raos, G.; Catellani, M.; Meille, S. V. *Chem. Mater.* **2009,** *21,* 78–87.

[95] Moreno, M.; Casalegno, M.; Raos, G.; Meille, S. V.; Po, R. *J. Phys. Chem. B* **2010,** *114,* 1591–1602.

[96] Erb, T.; Zhokhavets, U.; Gobsch, G.; Raleva, S.; Stühn, B.; Schilinsky, P.; Waldauf, C.; Brabec, C. J. *Adv. Funct. Mater.* **2005,** *15,* 1193–1196.

[97] Sato, T.; Cai, Z.; Shiono, T.; Yamamoto, T. *Polymer* **2006,** *47,* 37–41.

[98] Sato, T.; Yagi, T.; Tajima, H.; Fukuda, T.; Yamamoto, T. *Reactive and Functional Polymers* **2008,** *68,* 369–375.

[99] Ma, W.; Yang, C.; Gong, X.; Lee, K.; Heeger, A. J. *Adv. Funct. Mater.* **2005,** *15,* 1617–1622.

[100] Swinnen, A.; Haeldermans, I.; Vanlaeke, P.; D´Haen, J.; Poortmans, J.; D´Olieslaeger, M. *Eur. Phys. J. Appl. Phys.* **2007,** *36,* 251–256.

[101] Watts, B.; Belcher, W. J.; Thomsen, L.; Ade, H.; Dastoor, P. C. *Macromolecules* **2009,** *42,* 8392–8397.

[102] Tsao, H. N.; Cho, D.; Andrease, J. W.; Rouhanipour, A.; Breiby, D. W.; Pisula, W.; Müllen, K. *Adv. Mater.* **2009,** *21,* 209–212.

[103] Dante, M.; Garcia, A.; Nguyen, T.-Q. *J. Phys. Chem. C* **2009,** *113,* 1596–1600.

[104] Sary, N.; Richard, F.; Brochon, C.; Leclerc, N.; Leveque, P.; Audinot, J.-N.; Berson, S.; Heiser, T.; Hadziioannou, G.; Mezzenga, R. *Adv. Mater.* **2010,** *22,* 763–768.

[105] de Boer, B.; Stalmach, U.; van Hutten, P. F.; Melzer, C.; Krasnikov, V. V.; Hadziioannou, G. *Polymer* **2001,** *42,* 9097–9109.

[106] Lee, M.; Cho, B.-K.; Zin, W.-C. *Chem. Rev.* **2001,** *101,* 3869–3892.

[107] Klok, H.-A.; Langenwalter, J. F.; Lecommandoux, S. *Macromolecules* **2000,** *33,* 7819–7826.

[108] Olsen, B. D.; Segalman, R. A. *Macromolecules* **2005,** *38,* 10127–10137.

[109] Olsen, B. D.; Segalman, R. A. *Macromolecules* **2006,** *39,* 7078–7083.

[110] Olsen, B. D.; Segalman, R. A. *Macromolecules* **2007,** *40,* 6922–6929.

[111] Olsen, B. D.; Shah, M.; Ganesan, V.; Segalman, R. A. *Macromolecules* **2008,** *41,* 6809–6817.

[112] Tang, C.; Lennon, E. M.; Fredrickson, G. H.; Kramer, E. J.; Hawker, C. J. *Science* **2008,** *322,* 429–432.

[113] Chen, S.-C.; Kuo, S.-W.; Jeng, U.-S.; Su, C.-J.; Chang, F.-C. *Macromolecules* **2010,** *43,* 1083–1092.

[114] Dobrosielska, K.; Takano, A.; Matsushita, Y. *Macromolecules* **2010,** *43,* 1101–1107.

[115] Schleuss, T. W.; Abbel, R.; Gross, M.; Schollmeyer, D.; Frey, H.; Maskos, M.; Berger, R.; Kilbinger, A. F. M. *Angew. Chem. Int. Ed.* **2006,** *45,* 2969–2975.

[116] König, H. M.; Kilbinger, A. F. M. *Angew. Chem. Int. Ed.* **2007,** *46,* 8334–8340.

[117] Abbel, R.; Frey, H.; Schollmeyer, D.; Kilbinger, A. F. M. *Chem. Eur. J.* **2005,** *11,* 2170–2176.

[118] Gabellini, A.; Novi, M.; Ciferri, A.; Dell'Erba, C. *Acta Polym.* **1999,** *50,* 127–134.

[119] Abbel, R.; Schleuss, T. W.; Frey, H.; Kilbinger, A. F. M. *Macromol. Chem. Phys.* **2005,** *206,* 2067–2074.

[120] Cavallaro, S.; Cum, G.; Gallo, R.; Spadaro, A.; Visalli, G. *Magn. Reson. Chem.* **2002,** *40,* 219–224.

[121] Schulz-Dobrick, M.; Schnell, I. *Cent. Eur. J. Chem.* **2005,** *3,* 245–251.

[122] von Philipsborn, W.; Müller, R. *Angew. Chem.* **1986,** *98,* 381–412.

[123] Gorelik, T.; Kolb, U.; Matveeva, G.; Schleuss, T.; Kilbinger, A. F. M.; van de Streek, J.; Bohle, A.; Brunklaus, G. *CrystEngComm.* **2010,** *12,* 1824–1832.

[124] Steiner, T. *Angew. Chem. Int. Ed.* **2002,** *41,* 48–76.

[125] Lee, H.; de Vries, A. H.; Marrink, S.-J.; Pastor, R. W. *J. Phys. Chem. B* **2009,** *113,* 13186–13194.

[126] Adam, A.; Spiess, H. W. *Macromol. Rapid Commun.* **1990,** *11,* 249–259.

[127] Saalwächter, K.; Graf, R.; Spiess, H. W. *J. Magn. Reson.* **1999,** *140,* 471–476.

[128] Muntean, J. V.; Stock, L. M.; Botto, R. E. *J. Magn. Reson.* **1988,** *76,* 540–542.

[129] Morkombe, C. R.; Zilm, K. *J. Magn. Reson.* **2003,** *162,* 479–486.

[130] Frisch, M. J.; et all, *Gaussian 03;* Gaussian, Inc., Wallingford: 2003.

[131] Becke, A. *J. Chem. Phys* **1993,** *98,* 5648–5652.

[132] Stephens, P.; Devlin, F.; Chabalowski, C.; Frisch, M. *J. Phys. Chem.* **1994,** *98,* 11623–11627.

[133] J. Hutter, e. a. *Computer code CPMD, version 3.9;* Copyright IBM Corp. and MPI-FKF Stuttgart, http://www.cpmd.org: 1990–2004.

[134] Becke, A. D. *Phys. Rev. A* **1988,** *38,* 3098–3100.

[135] Lee, C.; Yang, W.; Parr, R. G. *Phys. Rev. B* **1988,** *37,* 785–89.

[136] Goedecker, S.; Teter, M.; Hutter, J. *Phys. Rev. B* **1996,** *54,* 1703.

[137] Hartwigsen, C.; Goedecker, S.; Hutter, J. *Phys. Rev. B* **1998,** *58,* 3641.

Danksagung

Hiermit möchte ich mich bei allen bedanken, die zum entstehen dieser Arbeit beigetragen haben.